The Pennsylvania State University

The Graduate School

Department of Materials Science and Engineering

NUMERICAL MODELING OF SPACE CHARGE DYNAMICS AND ELECTRICAL BREAKDOWN IN SOLID DIELECTRICS

A Dissertation in

Materials Science and Engineering

by

Doo Hyun Choi

Submitted in Partial Fulfillment

of the Requirements

for the Degree of

Doctor of Philosophy

December 2013

The dissertation of Doo Hyun Choi was reviewed and approved* by the following

Michael T. Lanagan
Professor of Engineering Science and Mechanics
Dissertation Co-Advisor
Co-Chair of Committee

Clive A. Randall
Professor of Materials Science and Engineering
Dissertation Co-Advisor
Co-Chair of Committee

Shujun Zhang
Senior Research Associate and Associate Professor of Materials Science and Engineering

Jeffrey Mayer
Associate Professor of Electrical Engineering

Seong H. Kim
Professor of Chemical Engineering

Suzanne Mohney
Professor of Materials Science and Engineering
Chair, Intercollege Graduate Degree Program in Materials Science and Engineering

*Signatures are on file in the Graduate School.

Abstract

A general numerical model has been developed to predict the dielectric breakdown strength of insulating materials. Low-alkali boroaluminosilicate glasses are of interest for electrostatic energy storage since they have exceptionally high dielectric breakdown strength. Polymer dielectric such as polyethylene is the state-of-the art material for power transmission cables. Therefore, understanding their breakdown mechanisms and predicting their strengths are important theoretically as well as practically. This research focuses on understanding electrical conduction and space charge dynamics and their effects on electrical breakdown strengths. Conduction mechanisms for AF45 glass (one kind of low-alkali BAS) below 473 K were studied using Schottky, Poole-Frenkel, space-charge-limited current, and ionic hopping conduction mechanism. This study showed that the electrical conduction in low-alkali BAS glass is governed by a combination of two or more conduction mechanisms. Cation depletion phenomena during thermal poling of low-alkali BAS is an important precursor to dielectric breakdown. Numerical models including multiple charge carriers such as Na^+, nonbridging oxygen ion, H_3O^+/H^+, Ba^{2+} were developed to predict depletion widths under anode and electric field distribution within the glass. These numerical models accurately predicted widths of 2.1 μm, which were very close to the experimentally determined values. Moreover, the calculated electric field from a numerical model assuming Na^+, H_3O^+/H^+, Ba^{2+} migration could reproduce the experimentally determined electric field distribution. Numerical breakdown models were developed assuming electronic conduction or ionic redistribution and electronic breakdown for low-alkali BAS glass. The numerical model assuming electronic conduction predicted weakly thickness dependent breakdown strengths below 20 μm although it cannot predict strongly thickness dependent breakdown strengths above 20 μm. Another combined breakdown model assuming ionic redistribution and electronic breakdown predicted two distinct regions in AF45 glass for thickness dependence of breakdown strengths. Temperature dependence of breakdown strengths for AF45

glass predicted by the model assuming ionic redistribution and electronic breakdown agreed well with experimental results. This model showed that the change in breakdown strengths with temperature depended on the initial mobile sodium ion concentration. Thermal and electronic breakdown combined model was also applied to low-density polyethylene where electrical conduction is dominated by electrons and holes. Upon high electric fields these carriers move and produce space charges which enhance local electric field near the anode. This breakdown model predicts weakly thickness dependent breakdown strengths at room temperature which is also proved by other researchers. Furthermore, the relationship between the breakdown strength and voltage ramp rate can be reproduced in this model.

TABLE OF CONTENTS

LIST OF FIGURES

LIST OF TABLES

ACKNOWLEDGEMENTS

First of all, I would like to express my sincere gratitude to my advisors, Dr. Michael Lanagan and Dr. Clive Randall, who are always providing great suggestions, valuable guidance, and encouragement throughout the study. Without their guidance and support, this dissertation would never become a reality.

My sincere gratitude is also extended to my committee members: Dr. Shujun Zhang, Dr. Jeffrey Mayer, and Dr. Seong Kim for serving on my Ph.D. committee and providing insightful comments. I am also grateful to my friends in our group, Dr. Eugene Furman, Dr. Priyanka Dash, Takashi, Dr. Mohan Manoharan, Seth, Betul, Dennis, Russell, Dr. Seok-Hyun Yoon, Dr. Jeongryul Kim, Dr. Chungeun Lee. Huge thanks to the tremendous support from the entire MRI staff and researchers. Special thanks to Jeff, Steve, Amanda and Paul for their continuous research support. Many thanks to so many other friends in and outside of Penn State. Special thanks to June Hyuk, Hyeong Jae, Sangkwon for spending time together and keeping me not alone.

I also express my sincere gratitude to my group members in Agency for Defense Development in South Korea. Dr. Yong Kee Baek gives me great opportunity for studying in Penn State and also become a great mentor for my life and research. For Dr. Eul Son Kang, Dr. Seung Su Baek, Dr. Hyung Kang thanks for allowing me to study abroad after knowing all the difficulties you'll have for several years. I cannot thank you enough.

I really owe this thesis to my family. Thanks to my mom, Mrs. Gwangsuk Lee for praying every day to achieve all these things. I thank my parents-in-law (Mr. Gwangeon Choi, Mrs. Chunja Kim) for raising my son such an adorable kid. Thanks also to my brothers and sister (Mr. Doosik Choi, Mr. Doohan Choi, Mrs. Eunhui Choi) for encouraging me all the time and supporting me. I would like to express special thanks to my lovely wife Heeyoung and adorable

son Boogyum for their endless love, support, understanding, and encouragement. Without them, I could not complete my dissertation.

Finally, I would like to acknowledge the financial supports from the Center for Dielectric Studies and Agency for Defense Development for my research.

Chapter 1: Introduction

Energy density and power density are two important figures-of-merit for applications of capacitors and dielectrics. These parameters fundamentally depend on material properties such as dielectric breakdown strength and permittivity. Energy density (E_{vol}) can be defined by

$$E_{vol} = \frac{1}{2}\varepsilon_r\varepsilon_0 E_b^2 \quad (1\text{-}1)$$

where ε_r is the relative permittivity, ε_0 the permittivity of free space, E_b the breakdown strength. The energy density is proportional to the permittivity and the square of breakdown strength. On the other hand, power density (P_{vol}) can be expressed by

$$P_{vol} = \frac{V^2}{4\times E.S.R.\times vol} = \frac{\pi f \varepsilon_r \varepsilon_0 E_b^2}{2\tan\delta} \quad (1\text{-}2)$$

where E.S.R. is the equivalent series resistance, vol is the volume of material, f is the operating frequency, and tanδ is the dielectric loss tangent. The power density also depends on the permittivity and the square of breakdown strength. Therefore, both energy density and power density are can be optimized through controlling these material properties. In this section, ceramic and polymer dielectric materials will be discussed for capacitor applications.

1.1. Dielectric materials for capacitor applications

1.1.1. Polymer materials for capacitor applications

Polymer materials are widely used for pulsed power and power electronic capacitors since large-area polymer films with good insulating properties can be fabricated by scalable manufacturing processes. Table 1-1 shows commonly used polymers for capacitor applications.

Flexible polymers are able to be wrapped in high speed roll-to-roll machines, which is an attractive process for low cost applications. For example rolled, metallized polypropylene films are placed in cylindrical containers with insulating oils in order to limit electrical discharge and enhance power dissipation.

Most available polymers for capacitor applications have low permittivities, ranging from 2.2 to 3.5, which are small in comparison to ceramic materials[1, 2]. Polymer permittivities are limited by electronic and dipolar mechanisms, unlike inorganic oxides with higher permittivities that are typically used in electrolytic and ceramic capacitors. One of the advantages of polymer materials is they can sustain low dielectric losses up to gigahertz range, except for the ferroelectric polymers such as P(VDF-TrFE) based copolymers[3]. The temperature dependence of permittivity and dielectric loss is also stable until the appearance of thermal transitions (i.e. T_g or melting point). The disadvantage of polymers is the low operating temperature range compared to ceramics and glasses[4]. For several polymers in Table 1-1, the maximum operating temperature is near 100 ^oC, although polymers such as polyimide and polyphenylene-sulfide can operate up to 200 ^oC. The maximum operating temperature is limited by the melting point or the dielectric loss at high temperature.

Table 1-1 Permittivity, loss tangent, and maximum operating temperature for polymers used for capacitor applications. Permittivity and loss tangent are measured at room temperature[1, 2].

Polymer	ε_r'	tan δ	T_{max} (^oC)	T_g(^oC)
Polystyrene	2.8	0.00026	85	100
Polyimide	3.6	0.00200	200	360~410
Polypropylene	2.3	0.00042	105	0
Polyester	3.5	0.00170	125	67~81
Polycarbonate	2.9	0.00097	125	145
Polyphenylene-sulfide	3.0	0.00030	200	85

1.1.2. Ceramic materials for capacitor applications

Depending on the magnitude of permittivity ceramic materials can be categorized into three groups which include low permittivity ($\varepsilon_r \leq 10$), medium permittivity ($10 < \varepsilon_r < 100$), and high permittivity ($\varepsilon_r > 100$). On the other hand ceramic materials can be divided into two categories of linear dielectrics and nonlinear dielectrics, and the energy densities of both types have been explored.

Linear dielectric mainly covers low to medium permittivity oxides such as SiO_2, Al_2O_3, ZrO_2, TiO_2 and $CaTiO_3$-based materials. McPherson et al. have established an inverse relationship between relative permittivity and breakdown strength for linear dielectrics according to the thermochemical model[5]. Theoretical maximum breakdown strengths for these materials are predicted to range from10 to 15 MV/cm. Thus this model has suggested energy density greater than 20 J/cm^3 for these materials. Nano-crystalline TiO_2 has been reported to have energy density of 17 J/cm^3[6]. $0.8CaTiO_3$-$0.2CaHfO_3$ with 0.5 mol% Mn has been reported to show energy density as high as 9.5 J/cm^3 which is sustained up to 200 ^{o}C[7].

Ferroelectrics, antiferroelectrics, and relaxors constitute nonlinear dielectrics. Ferroelectric ceramics such as $BaTiO_3$ and $Pb(Zr,Ti)O_3$ show permittivity greater than 1000, which diminish at high electric fields due to the saturation of polarization. Love has reported energy density of 4.8 J/cm^3 for commercial X7R MLCCs[8]. Antiferroelectrics such as $(Pb,La)(Zr,Ti)O_3$ (PLZT) show enhanced permittivity at high fields due to the phase transition from antiferroelectric to ferroelectric phases. Ma et al. have reported energy density as high as 60 J/cm^3 for PLZT film-on-foil capacitors[9]. Relaxors with composition of $BaTiO_3$-$BiScO_3$ have been reported to have energy density from 6.1 to 16 J/cm^3[10, 11]. These parameters including permittivity, breakdown strength and energy density are summarized in Table 1-2.

Table 1-2 Permittivity, breakdown strength and energy density for key ceramic dielectrics;*: permittivity at low electric field.

Material	Type	Permittivity*	Breakdown strength (MV/m)	Energy density (J/cm^3)	Ref.
$BaTiO_3$-based commercial X7R	Ferroelectric	1800	90	4.8	[8]
PLZT	Antiferroelectric	1300	435	29-60	[9, 12]
$BaTiO_3$-$BiScO_3$	Weakly-coupled relaxor	650	73	6.1-16	[10, 11]

1.1.3. Glass materials for capacitor applications

Glass and glass ceramics can also be categorized into low, medium, and high permittivity materials. Glass ceramics are composed of embedded nanocrystallites in a glass matrix. These materials can be fabricated by melt processing and thus acquire very low porosity and high breakdown strength[13]. Alkali-free glasses have a low permittivity of about 6. Recently the breakdown strength as high as 1200 MV/m has been reported for these alkali-free glasses with thicknesses from 10 to 50 μm which predict electrostatic energy density as high as 35 J/cm^3[14-16]. These glasses also maintain low dielectric loss up to 200 ^oC, which provides an advantage for automotive and aerospace applications with high temperature environment[14]. Multilayered capacitors with these thin glasses have been considerable interests for potential applications in electric vehicles[17]. For thicknesses of 5 μm, these alkali-free glass shows ample flexibility which will allow them to be incorporated into a roll-to-roll rolled process that is similar to polymer film capacitors[17].

Ferroelectric glass ceramics have both high permittivity and low permittivity which are critical for high energy density values. Glass ceramics such as PbO-BaO-SrO-Nb_2O_0-B_2O_3-SiO_2

($Sr_{0.33}Ba_{0.67}Nb_2O_6$ phase), Na_2O-PbO-Nb_2O_5-SiO_2 ($Pb_2Nb_2O_7$, $NaNbO_3$, and $PbNb_2O_6$ phases), and BaO-TiO_2-Al_2O_3-SiO_2 systems have been studied using melt-casting and subsequent heat treatment[18]. These glass ceramics have showed permittivities of 250 – 350 and breakdown strengths of 40 – 80 MV/m, which result in energy density as high as 8 J/cm^3[18].

1.1.4. Other materials for capacitor applications

There are also several other types of capacitors including electrolytic capacitors and electrochemical capacitors. Aluminum and tantalum capacitors are most widely used electrolytic capacitors where aluminum oxide and tantalum oxide layers are used as dielectric layers. These layers have thickness as thin as 100 nanometers and can be fabricated using electrochemical oxidation process at anode. This thin layer of dielectric materials has a rough surface and will store charges. In electrolytic capacitors one of both of electrodes can be solid electrolyte. The combination of thin dielectric layers and high surface area can achieve very high capacitance which ranges from 1 to 10^5 μF. Its high volumetric capacitance is one of the essential advantages for electrolytic capacitors[19]. The energy density for electrolytic capacitors has been reported about 0.2 J/g[20].

Electrochemical capacitors can be divided into double layer capacitor and supercapacitor/ ultracapacitor. These capacitors generally have very high capacitance in the Farads range. A porous carbon electrode with high surface area, electrolyte and separator constitute the double layer capacitor. The interfacial charge at double layers between carbon electrode and electrolyte results in high capacitance in double layer capacitors. Therefore the capacitance of double layer capacitor can be improved through maximizing the surface area of carbon electrode. Supercapacitors or ultracapacitors are based on the principle of space charge electrode polarization and pseudo-capacitance contribution[21]. Examples being specially processed

carbons, metal oxide such as RuO_2, and conducting polymers can be used for electrodes in supercapacitors. Supercapacitors can be charged by a faradic reaction which include absorption of ion from the electrolyte or by redox reaction between electrode and electrolyte or by doping and undoping of conductive polymer electrode. The energy density in the range of 10 – 20 J/kg has been reported for electrochemical capacitors[22].

1.1.5 Dielectric materials and Capacitor Energy Densities

Energy density is an important parameter for predicting material and capacitor performance. Figure 1-1 shows energy density for a wide range of dielectric materials and capacitor technologies. Capacitor technologies can be divided into pulsed power capacitor, power electronic capacitor and high temperature capacitor. As moving from the intrinsic dielectric material to the high temperature capacitor the energy densities decrease. The intrinsic energy densities for dielectric materials can be remarkably high at the breakdown electric fields. It should be noted that the operating electric fields are generally less than half the breakdown electric fields due to reliability issues. Fluoropolymers having high permittivities larger than 20 and high breakdown fields result in one of highest energy densities close to 25 J/cm^3[23].

The operating electric field for each capacitor technology depends on the application. Pulsed power capacitors require a finite number of charge/discharge cycles and operating electric fields close to the breakdown fields. Figure 1-1 shows that pulsed power capacitors have the highest energy densities among capacitor technologies. Polymer capacitors have a significant advantage over ceramics because of self-healing modes. Metallized polymer films have the ability of self-healing and undergo the phenomenon of ‘graceful failure’ contrary to the catastrophic failure mode in ceramics[24, 25]. During the self-healing process local defects such as pinholes, microflaws or impurities result in local heating and localized breakdown. The energy

discharge during breakdown evaporates metallized electrodes and then isolates the damaged area, thus creating a decreased capacitance rather than short circuit. Therefore the capacitor system is still operative after local breakdown. Contrary to polymer materials, ceramic materials generally do not exhibit self-healing properties. Ceramic materials for capacitors applications can be operative over wide temperature range due to its high melting temperature and low dielectric loss at high temperature. Superior power densities of ceramic materials are another advantage for capacitor applications.

Pulsed power application needs a limited lifetime due to a small number of charge/discharge cycles. The operating electric fields for power electronic capacitors must be lower since they require more extreme voltage cycles than pulsed power capacitors. Power electronic capacitors confront very challenging reliability requirements since they operate under high electric fields and ripple currents for long periods of time. Therefore power electronic capacitors need significant voltage de-rating factors. The energy density for power electronic capacitors is in the range of 0.1 J/cm^3. For high temperature capacitors, the energy densities are less than 0.01 J/cm^3 due to the further reduced operating electric field.

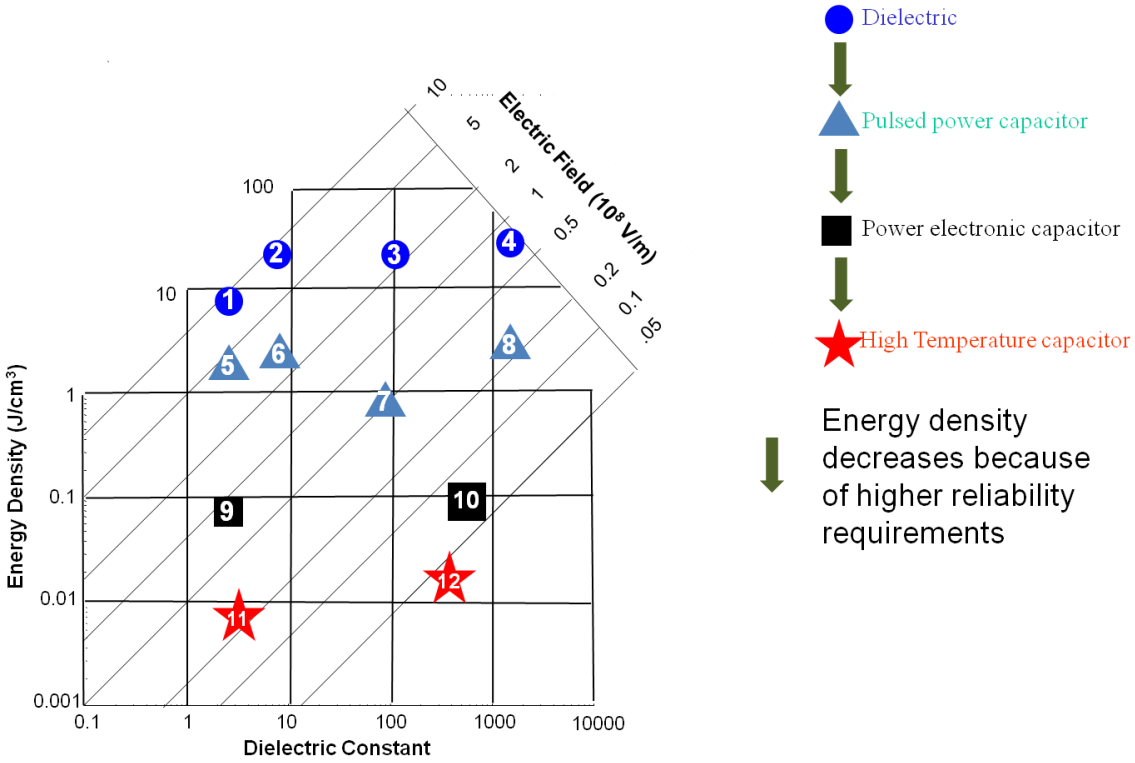

Figure 1-1 Energy density comparison for dielectric materials and capacitors. 1) biaxially oriented polypropylene, 2) modified poly(vinylidene fluoride) polymer, 3) titanium oxide dielectric, 4) antiferroelectric/ferroelectric phase switch ceramic, 5) polypropylene film capacitor for pulsed power, 6) PVDF film capacitor for pulsed power, 7 and 8) ceramic capacitors for pulsed power, 9) commercial polymer film power capacitor, 10) commercial multilayer ceramic capacitor, 11) commercial high temperature film capacitor(125 ^{o}C operation), 12)commercial high temperature ceramic capacitor(200 ^{o}C operation)[26].

1.2. Comparison of capacitor materials using Ragone plots

1.2.1. General theory for Ragone plots

Energy storage devices (ESDs) including a capacitor, battery, flywheel or magnetic energy storage devices have a wide range of energy density and power density. In a practical point of view, it is very important to determine which ESDs are most appropriate for a given application.

ESDs connected to a load (i.e. motor, actuator) are characterized by their maximum energy and power output. Ragone plots are charts used for performance comparison of various energy storing devices. Ragone plots, which compare power density and energy density in a log-log scale are widely used in the battery community and useful for two reasons. First, the maximum available power of ESDs can be determined from the internal device loss and stored energy density. Secondly, the optimum operating range of a power system can be defined by finding the portion of the plot where both energy and power are optimized. A fundamental understanding of the intrinsic power and energy density of a dielectric provides a path for materials development. For example, increasing high-temperature dielectric breakdown yields higher operating fields and higher energy density. Ripple current is related to power density and also increases with high temperature dielectric reliability.

Christen et al.[27] proposed a mathematical definition of the Ragone plots for different energy storage devices. In the general circuit of Figure 1-2, the ESD can be any kind of electrical power source. In most cases this ESD may be considered as a voltage source (V) with an internal series resistance (R) and an internal inductance (L). This voltage of the source depends upon the stored charge (Q). In this simplified model, the load connected to the ESD consumes constant power (P). Firstly assume there is no reactive power at the load. Then the current (I) and voltage (U) at the load can be described by a nonlinear equation of U=P/I. With the help of initial conditions, $Q(0)=Q_0$ and $\dot{Q}(0)=\dot{Q}_0$, the following ordinary differential equation for Q(t) which governs the electrical dynamics,

$$L\ddot{Q} + R\dot{Q} + V(Q) = -\frac{P}{\dot{Q}} \qquad (1\text{-}3)$$

where the dot means the derivative with respect to time. The Ragone plots can be expressed as follows. Initially (t=0) a certain amount of energy, $E_0=L\dot{Q}_0^2/2+W(Q_0)$, is stored in the device. With increasing time, a constant power (P) is consumed at the load so that Q(t) can be described

by Eqn. (1-3). Due to the finite amount of stored energy (E_0), the ESD can provide this power for a limited amount of time ($t_\infty(P)$). The available energy can be given by $E(P)=Pt_\infty(P)$ where the power (P) is time independent. Finally the Ragone plot can be suggested by the curve E(P) versus P. This method is useful since it holds regardless of the specific ESD.

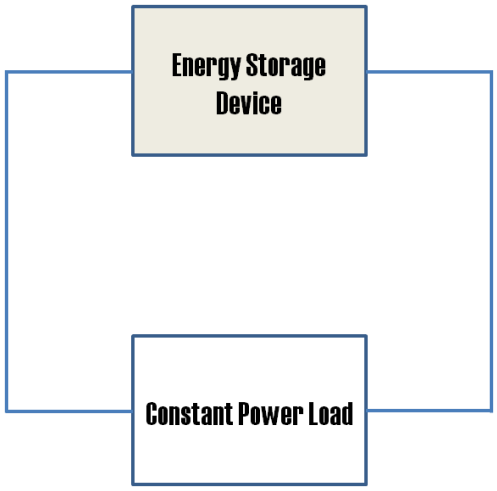

Figure 1-2 General circuit related with Ragone plots; a load consumes constant power P drawn from the ESDs.

1.2.2. Ragone plots for capacitors and capacitor materials

Now, we focus on the particular case of an ideal capacitor without inductance (L=0), so the operating frequency is well below the capacitor self-resonance. We assume that an ideal capacitor resistance and polarization values have neither frequency dependence nor an intrinsic nonlinearity with electric field. The electrical potential (V(Q)) of a capacitor obeys a linear dependence on the charge (Q) via a relationship of V(Q)=Q/C. The voltage drop at the load can be derived from Eqn. (1-3) and will be given by U=P/I=Q/C-RI with I=-$\dot{Q}$. After differentiating each expression for U with respect to time, the $\dot{I}$ in the first expression can be replaced by the second expression. Then multiplying each side by U and rearranging using $dU^2=2UdU$ gives the following ordinary differential equation for U^2

$$\left(1-\frac{RP}{U^2}\right)\frac{dU^2}{dt}=-\frac{2P}{C} \qquad (1\text{-}4).$$

The Eqn. (1-4) can be integrated after separation of variables and leads to the solution

$$t(U)=\frac{C}{2P}\left[RP\ln\left(\frac{U^2}{U_0^2}\right)+U_0^2-U^2\right] \qquad (1\text{-}5).$$

The criterion where the capacitor cannot supply the required power (P) can be determined by dt/dU=0. The corresponding voltage will be $U_\infty=\sqrt{RP}$ assuming positive U. There is a finite amount of energy t_∞ where the residual energy is $E_\infty=2RCP$. At times greater than t_∞ the capacitor cannot provide the required power (P). From the relationship between time and maximum energy, the maximum power of the capacitor can be suggested by $P_{max}=E_0/2RC$. The Ragone plot can be determined by the relation of $E_c=Pt_\infty$. However, it should be noted that U_0 in Eqn. (1-5) depends on power (P) since the voltage drop at the capacitor will be $U_C=U+RI=U+RP/U$. One finds for the corresponding value of the voltage $U_\infty=\sqrt{RP}$ (assuming positive U). In order to calculate the Ragone plot, $E_c=Pt_\infty$, one has to be careful. Indeed, U_0 in Eqn. (1-5) depends on P, because

U_C=U+RI=U+RP/U is the voltage drop at the capacitance. Therefore, the Ragone curve will be given by

$$E_c(P) = \frac{C}{2}\left[RP\ln\left(\frac{RP}{U_0^2}\right) + U_0^2 - RP\right] \quad (1\text{-}6)$$

$$U_0 = \frac{U_{C,0}}{2} + \sqrt{\frac{U_{C,0}^2}{4} - RP} \quad (1\text{-}7)$$

where $U_{C,0}$ is the initial capacitor voltage. For the capacitor, the total energy (E_0) is $CU_{C,0}^2/2$. As previously mentioned there is a maximum power ($P_{max}=E_0/2RC=U_{C,0}^2/4R$) which can be attained for $E_c \rightarrow 0$.

There are several kinds of capacitor components made of different dielectric materials and electrode configurations which include multilayer ceramic capacitors (MLCCs), aluminum electrolytic capacitors (Al electrode or polymer electrode), tantalum electrolytic capacitors (MnO_2 electrode or polymer electrode) and film (polymer) capacitors. Applying the Ragone theory to these kinds of capacitors is interesting and useful to determine what is an adequate capacitor for a specific application. In addition, the strengths and weaknesses of each capacitor technology can be evaluated from the Ragone plot. Table 1-3 summarizes commercial capacitors and their properties for each category.

Eqns. (1-6) and (1-7) present Ragone plots using volume for given capacitor components and shown in Figure 1-3. It is noteworthy that MLCCs have two orders of magnitude higher power density than film capacitors and four orders of magnitude higher power density than Al and Ta electrolytic capacitors. For energy density, MLCCs have one order of magnitude higher energy density than film capacitors and about two times higher than Al and Ta electrolytic capacitors. It is interesting that for Ta electrolytic capacitors with polymer electrodes power density increased more than one order of magnitude with the expense of energy density. A same trend holds for the Al electrolytic capacitor with polymer electrode. Figure 1-4 shows Ragone plots using mass for same capacitor components. It is noteworthy that due to the low density of

polypropylene the energy density of film capacitor is comparable to that of MLCCs and the difference of power density between them also decreases.

Table 1-3 Five different capacitor types and their electrical properties used for Ragone plots[28-32].

Capacitor type	C(μF)	ESR(Ω)	Voltage rating(V)	Ref.
MLCC	25	0.001	630	[28]
Al electrolytic	180	0.67	500	[29]
Al electrolytic +polymer electrode	22	0.03	16	[30]
Film	80	0.01	600	[29]
Ta electrolytic	400	0.4	100	[31]
Ta + polymer electrode	6.8	0.12	75	[32]

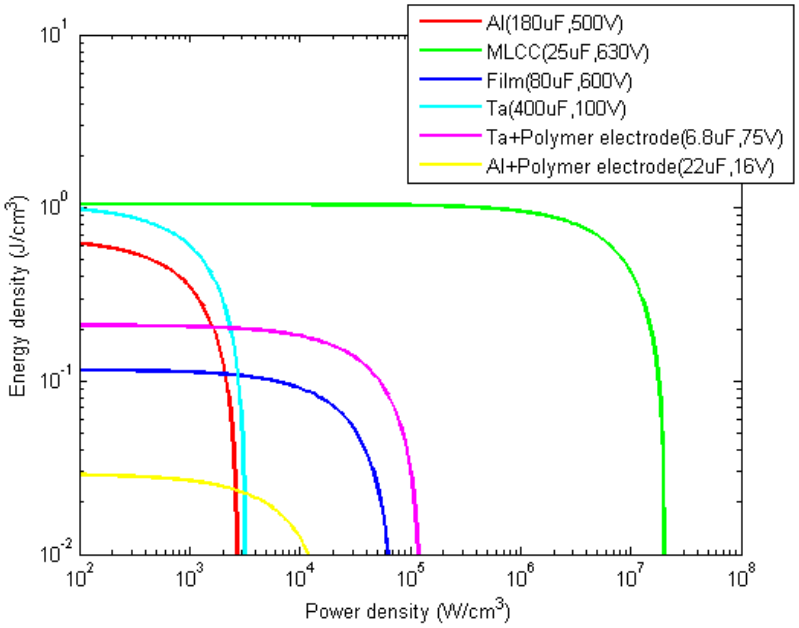

Figure 1-3 Ragone plots using volume for 5 different capacitor components: Al electrolytic, MLCC, Film, Ta electrolytic, and Ta electrolytic with polymer electrode; 1 kWh/cm^3= 3600 kJ/cm^3.

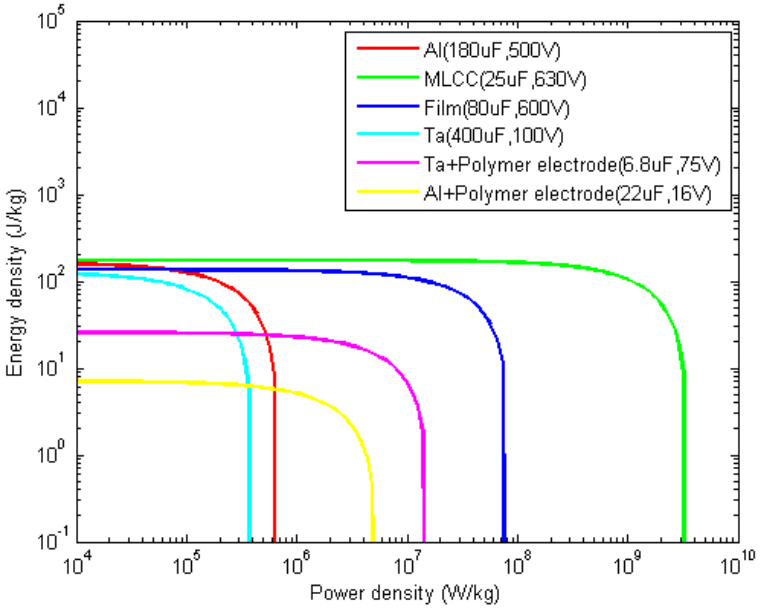

Figure 1-4 Ragone plots using mass for 5 different capacitor components: Al electrolytic, MLCC, Film, Ta electrolytic, and Ta electrolytic with polymer electrode.

Ragone plots at material levels are interesting since it can show materials ultimate energy density and power density. For this purpose permittivity, dielectric loss, and breakdown strength substitute capacitance, equivalent series resistance (ESR), and voltage rating respectively. Then using those values in Table 1-4 Ragone plots are drawn for glass (OA-10G), biaxially-oriented polypropylene, and $BaTiO_3$ as shown in Figure 1-5. For biaxilly-oriented polypropylene Ragone plot is also suggested for 95 ^oC to show the temperature effect on Ragone plot. At room temperature the energy density of glass and $BaTiO_3$ is about one order of magnitude higher than that of BOPP, whereas the power densities for three materials have a similar order of magnitude. It is also noteworthy that when temperature increases to 95 ^oC the power density decreases about one order of magnitude and the energy density becomes half the energy density at room temperature.

Power and energy densities are important parameters for materials scientists and engineers; however at the systems level, the available total power and energy values for dielectrics and capacitors depend upon processing and manufacturing capabilities. Table 1-5 and Figure 1-6 summarize the available energy and power ranges for current capacitor technologies. The applications spaces have been also delineated.

Commercial multilayer ceramic and polymer film capacitors represent the highest total power values among all of the available capacitor technologies. Polymer film capacitors have the added manufacturing benefit of a roll-to-roll processing for winding hundreds of square meters of dielectric film into a component. Large energy MLCC's are fundamentally limited by binder removal and stacking processes. Large energy values are available in electrochemical and electrolytic capacitors and the fundamental power limitations are a result of the high equivalent series resistances. It is interesting that the Ta polymer capacitor technology is an ideal fit for higher frequency microelectronic applications. The power-to-energy ratio is about 6,000 for the

Ta polymer which is substantially higher than the ratio of about 600 for conventional Ta-capacitor with Mn electrodes.

Table 1-4 Material parameters used for evaluating Ragone plots at material level;*:permittivity is calculated from energy density. $BaTiO_3$ is nonlinear dielectric and average permittivity of 351 is used to cover the low to high field nonlinear response.; breakdown field and dielectric loss are obtained from other literatures[8, 10, 16, 33, 34].

Dielectrics	ε_r	Tan δ	E_{bd} (MV/m)	Area/Thickness
Glass(OA10G)	6	0.004	840	1 $cm^2/10^{-3}$ cm
Biaxially-oriented polypropylene(25°C)	2.2	0.0004	700	1 $cm^2/10^{-3}$ cm
Biaxially-oriented polypropylene(95°C)	2.2	0.002	640	1 $cm^2/10^{-3}$ cm
$BaTiO_3$*	351*	0.0013	100	1 $cm^2/10^{-3}$ cm

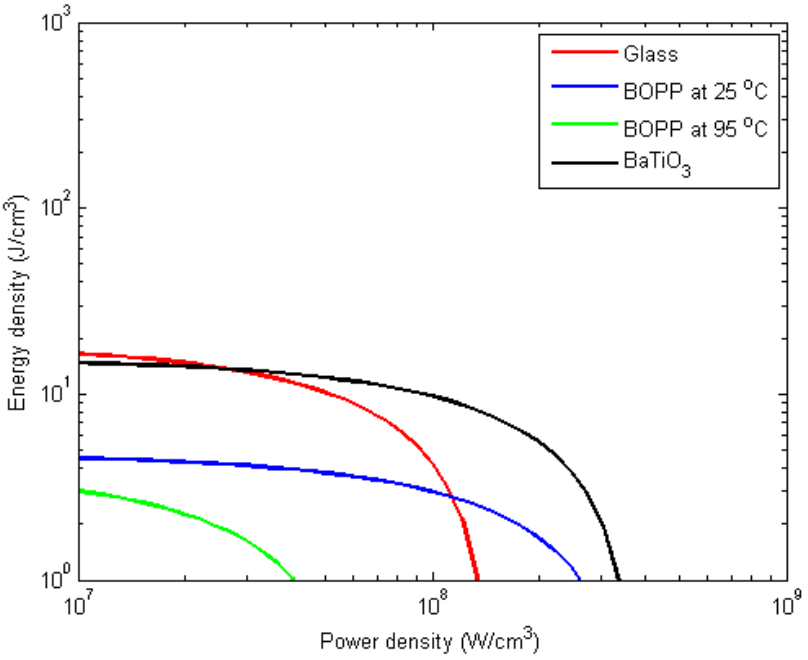

Figure 1-5 Ragone plots for glass, BOPP, and $BaTiO_3$ at the material level.

Table 1-5 Energy and power values for commercial capacitors;*:power was calculated from peak current instead of ESR[28, 31, 35-40].

Capacitor type	Capacitance	Voltage	ESR	Energy	Power	Ref.
	F	V	Ω	J	W	
Film (power)	1.0E-03	600	1.3E-04	1.8E+02	7.2E+08	[35]
Film (pulsed power)*	6.4E-02	2825		2.6E+05	7.9E+08	[36]
MLCC	2.5E-05	630	1.0E-03	5.0E+00	9.9E+07	[28]
Al	2.2E+00	10	1.4E-03	1.1E+02	1.7E+04	[37]
Ta	2.4E-02	50	3.5E-02	3.0E+01	1.8E+04	[31]
Ta polymer	1.5E-03	6.3	5.5E-02	3.0E-02	1.8E+02	[38]
EDL	6.0E+03	2.5	2.2E-03	1.9E+04	7.1E+02	[37]
Supercapacitor	9.4E+01	75	1.3E-02	2.6E+05	1.1E+05	[39]
MLCC	1.0E-12	16	2.2E-01	1.3E-10	2.9E+02	[40]

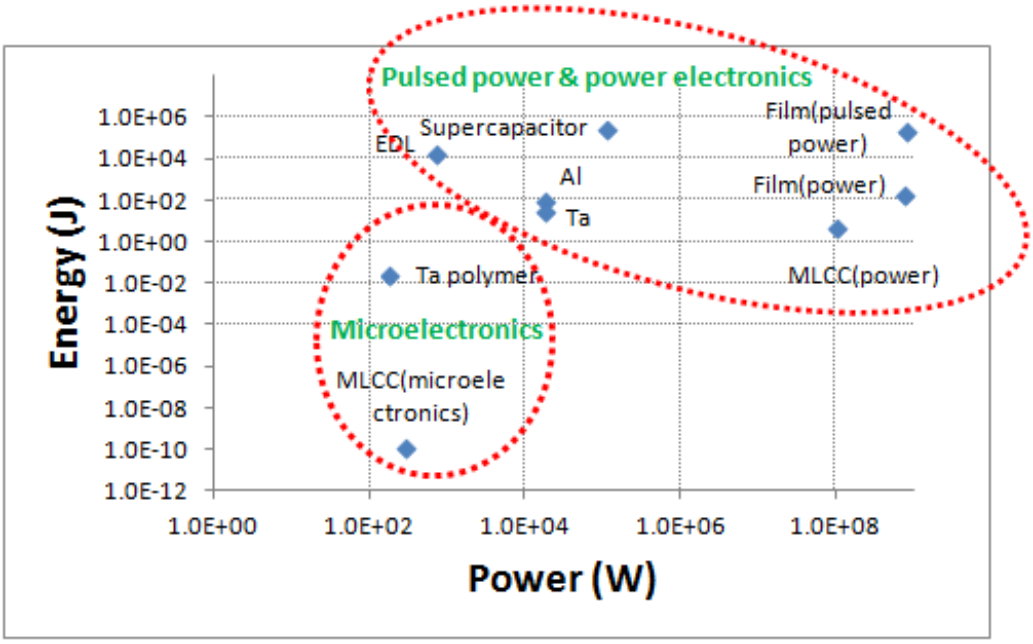

Figure 1-6 Energy and power values for commercial capacitor according to the application.

1.3. Research goals

Dielectric breakdown is one of the most critical materials properties in determining both the power and energy density of a capacitor. This research aims to develop numerical models for predicting the electrical breakdown strength and the cation depletion region depending on the temperature and electric field. These models are based on the charge transport and charge injection at high electric fields. Models for electrical breakdown mainly based on electronic breakdown and thermal breakdown apply these electric conduction phenomena to evaluate local electric field development and temperature evolution until breakdown. Taking into account space charges within dielectric is important since these affect local electric fields through Poisson's equation ($\nabla^2 V=\rho/\varepsilon_r\varepsilon_0$) where ρ is the charge density. These models will be used to predict the breakdown strengths of low-density polyethylene, and low-alkali boroaluminosilicate glass. Models for cation depletion region under high electric fields and high temperature will also be developed for low-alkali boroaluminosilicate glass. These models are also based on the charge transport of mobile ions for given time of electrical poling.

1.4. References

1. Munshi, M.Z.A., *Handbook of solid state batteries & capacitors*. 1995: World Scientific.
2. Jow, T. and P. Cygan, *Dielectric breakdown of polyvinylidene fluoride and its comparisons with other polymers.* Journal of Applied Physics, 1993. **73**(10): p. 5147-5151.
3. Claude, J.W., *Ferroelectric polymers for electrical energy storage*. 2008, The Pennsylvania State University.
4. Yen, S., et al. *Development of high temperature polyimide dielectric film for leaded and surface mount capacitor application*. in *Power Sources Symposium, 1992., IEEE 35th International*. 1992: IEEE.
5. McPherson, J., et al., *Thermochemical description of dielectric breakdown in high dielectric constant materials.* Applied Physics Letters, 2003. **82**(13): p. 2121-2123.

6. Ye, Y., *Influence of nanocrystalline grain size on the breakdown strength of ceramic dielectrics.* 2003.
7. Shay, D.P., et al., *High Energy Density, High Temperature Capacitors Utilizing Mn-Doped 0.8 $CaTiO_3$–0.2 $CaHfO_3$ Ceramics.* Journal of the American Ceramic Society, 2011.
8. Love, G.R., *Energy storage in ceramic dielectrics.* Journal of the American Ceramic Society, 1990. **73**(2): p. 323-328.
9. Ma, B., et al., *Fabrication and characterization of ferroelectric PLZT film capacitors on metallic substrates.* Journal of Materials Science, 2010. **45**(1): p. 151-157.
10. Ogihara, H., C.A. Randall, and S. Trolier McKinstry, *High Energy Density Capacitors Utilizing 0.7 $BaTiO_3$–0.3 $BiScO_3$ Ceramics.* Journal of the American Ceramic Society, 2009. **92**(8): p. 1719-1724.
11. Tinberg, D.S. and S. Trolier-McKinstry, *Structural and electrical characterization of x$BiScO_3$-(1-x) $BaTiO_3$ thin films.* Journal of Applied Physics, 2007. **101**(2): p. 4112.
12. Turtle, B.A., et al., *High energy density PLZT thin film capacitors.* Advanced Dielectric, Piezoelectric and Ferroelectric Thin Films, Volume 162, 2005: p. 17-25.
13. Cheng, C.T., et al., *Crystallization Kinetics and Phase Development of PbO–BaO–SrO–Nb_2O_5–B_2O_3–SiO_2-Based Glass–Ceramics.* Journal of the American Ceramic Society, 2005. **88**(11): p. 3037-3042.
14. Smith, N.J., et al., *Alkali-free glass as a high energy density dielectric material.* Materials Letters, 2009. **63**(15): p. 1245-1248.
15. Lee, H., et al., *Dielectric Breakdown of Thinned BaO–Al_2O_3–B_2O_3–SiO_2 Glass.* Journal of the American Ceramic Society, 2010. **93**(8): p. 2346-2351.
16. Murata, T., et al., *Electrode-Limited Dielectric Breakdown of Alkali Free Glass.* Journal of the American Ceramic Society, 2012.
17. Furman, E., et al., *High-Temperature, High-Power Capacitors: the Assessment of Capabilities.* SAE International Journal of Aerospace, 2009. **1**(1): p. 822-831.
18. Gorzkowski, E.P., et al., *Effect of additives on the crystallization kinetics of barium strontium titanate glass-ceramics.* Journal of the American Ceramic Society, 2008. **91**(4): p. 1065-1069.
19. Sakabe, Y., *Multilayer ceramic capacitors.* Current Opinion in Solid State and Materials Science, 1997. **2**(5): p. 584-587.
20. Sarjeant, W.J., I.W. Clelland, and R.A. Price, *Capacitive components for power electronics.* Proceedings of the Ieee, 2001. **89**(6): p. 846-855.
21. Conway, B.E., *Transition from "supercapacitor" to "battery" behavior in electrochemical energy storage.* Journal of the Electrochemical Society, 1991. **138**(6): p. 1539-1548.
22. Burke, A., *Ultracapacitors: why, how, and where is the technology.* Journal of Power Sources, 2000. **91**(1): p. 37-50.
23. Chu, B., et al., *A dielectric polymer with high electric energy density and fast discharge speed.* Science, 2006. **313**(5785): p. 334-336.
24. Reed, C. and S. Cichanowskil, *The fundamentals of aging in HV polymer-film capacitors.* Dielectrics and Electrical Insulation, IEEE Transactions on, 1994. **1**(5): p. 904-922.
25. Ieda, M., M. Nagao, and M. Hikita, *High-field conduction and breakdown in insulating polymers. Present situation and future prospects.* Dielectrics and Electrical Insulation, IEEE Transactions on, 1994. **1**(5): p. 934-945.
26. Lanagan, M. *Glass-based dielectrics for high temperature capacitors*. in *International conference and exhibition on high temperature electronics*. 2008. Albuquerque, New Mexico, USA.

27. Christen, T. and M.W. Carlen, *Theory of Ragone plots.* Journal of Power Sources, 2000. **91**(2): p. 210-216.
28. Kageyama, T. 2007 [cited 2013 02/07]; Available from: http://www.murata.com/articles/ta06d2.pdf.
29. Dubilier, C. 2013 [cited 2013 7/2]; Available from: http://www.cde.com/catalogs/UNL.pdf.
30. KEMET. 2013 [cited 2013 7/2]; Available from: http://capacitoredge.kemet.com/capedge2/intellispec.jsp?pn=A700D226M016ATE030&displayPN=A700D226M016ATE030.
31. Sprague, V. 2013 [cited 2013 7/2]; Available from: http://www.vishay.com/docs/43009/ste.pdf.
32. AVX. 2013 [cited 2013 7/2]; Available from: http://www.avx.com/docs/Catalogs/tcj.pdf.
33. Ho, J., *Characterization of High Temperature Polymer Thin Films for Power Conditioning Capacitors.* 2009.
34. Milliken, A.D., A.J. Bell, and J.F. Scott, *Dependence of breakdown field on dielectric (interelectrode) thickness in base-metal electroded multilayer capacitors.* Applied Physics Letters, 2007. **90**(11): p. 112910-112910-3.
35. SBE. 2011 [cited 2013 7/2]; Available from: http://www.sbelectronics.com/wp-content/uploads/2011/01/power_ring_700D348_jan-20-web.pdf.
36. Atomics, G. 2013 [cited 2013 7/2]; Available from: http://www.ga-esi.com/EP/capacitors/series-CMX-high-energy.php.
37. Nichicon. 2013 [cited 2013 7/2]; Available from: http://products.nichicon.co.jp/en/product_detail.cfm.
38. KEMET. 2012 [cited 2013 7/2]; Available from: http://capacitoredge.kemet.com/capedge2/intellispec.jsp?pn=T520H158M006ATE055&displayPN=T520H158M006ATE055.
39. Maxwell. 2013 [cited 2013 7/2]; Available from: http://www.maxwell.com/products/ultracapacitors/docs/datasheet_bmod0094_1012179.pdf.
40. TDK. 2011 [cited 2013 7/2]; Available from: http://www.tdk.co.jp/tefe02/e741_tfcap_tfsq0402.pdf.

Chapter 2: Theoretical Background for Electrical Breakdown and Conduction under High Electric Field

Electrical breakdown is a catastrophic and irreversible phenomenon which in the final stage destroys the dielectric material by creating a narrow breakdown channel between the electrodes. An excessive amount of electrical power passes through a small cross sectional area of the conductive channel, resulting in broken chemical bonds and thermally degraded regions. The origins of dielectric breakdown can be understood in terms of the pre-breakdown conduction processes[1]. Therefore in this chapter electrical breakdown and conduction mechanisms under high electric field will be discussed.

2.1. Electrical breakdown mechanism

There are many similarities between electrical and mechanical breakdown strength properties in materials. Both are fundamentally based on statistics and are strongly affected by processing defects. Temperature and stress conditions also play strong roles in influencing breakdown. Mechanical breakdown involves local stress enhancement at flaw tips and electrical breakdown typically involves local electric field enhancement due to space charge. The ultimate mechanical strength of a material is related to bond strength, crystal structure and microstructure. Dielectric strength is dependent upon fundamental materials properties such as thermal conductivity, heat capacity, band gap, work function, electrical conductivity, Young's modulus.

2.1.1. Electrical breakdown categories

Electrical breakdown is a complex process that occurs in dielectrics and is an important research area for optimizing the performance of capacitor materials. Electrical breakdown in a capacitor makes the device inoperable since it no longer stores charge and it behaves more like a resistor. The energy density of a capacitor quadratically depends on the electrical breakdown strength which makes the research of its origin important. Electrical breakdown mechanisms can be divided into four categories of electronic, thermal, electromechanical and partial discharges breakdown according to the process leading to the final stage. Figure 2-1 shows a schematic diagram for these breakdown mechanisms as a function of electric field and time-to-breakdown. This figure also shows an electrical degradation mechanism which occurs under low electric field

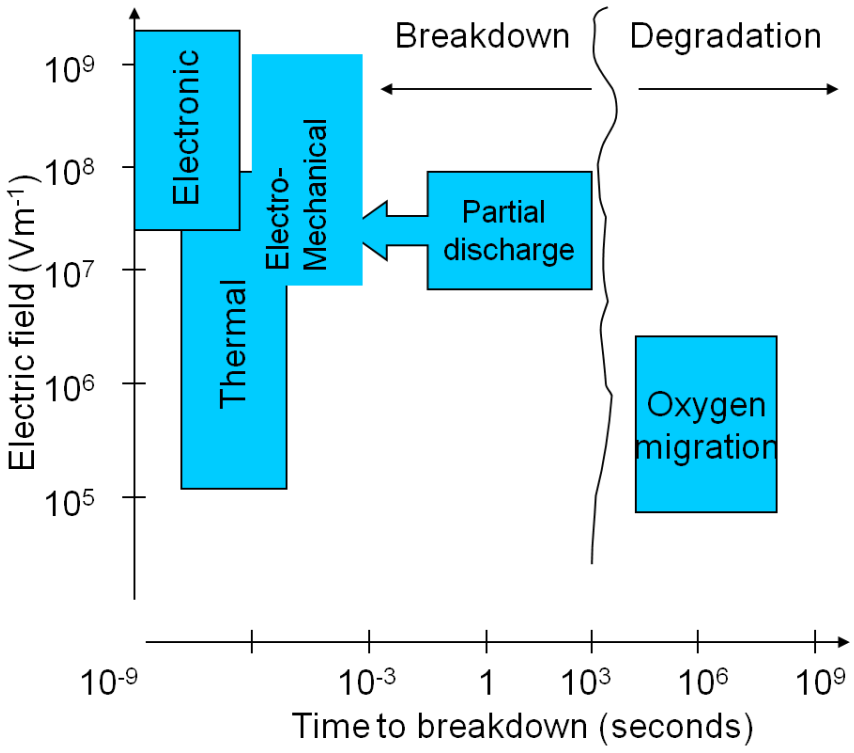

Figure 2-1 Times and electric fields at which most common electrical breakdown mechanisms and degradation mechanisms are operative under DC bias with dielectrics[2].

and on time scales greater than one thousand seconds, although the difference between breakdown and degradation is somewhat indistinct. It should be noted that the breakdown strength is often influenced by local effects such as field distortion due to space charge formation, temperature increase due to local heating and thickness deformation due to Maxwell stress.

2.1.2. Thermal breakdown mechanism

It has been frequently stated that all electrical breakdown is ultimately in some manner thermal[1]. The thermal breakdown mechanism is generally described as the breakdown induced by continuous joule heating within the dielectric from electrical conduction and polarization processes coupled with insufficient heat loss by thermal conduction or convection. The power balance equation composed of the heat generation rate and the heat loss rate is governed by

$$C_v\left(\frac{\partial T}{\partial t}\right) - \mathrm{div}(\kappa \nabla T) = \sigma E^2 \qquad (2\text{-}1)$$

where C_v is the specific heat per unit volume, T and t are temperature and time, E is the electric field, and σ and κ are the electrical and thermal conductivities respectively. For the DC fields, σ is the dc electrical conductivity. For the AC field, the conductivity from dielectric polarization loss should be added to the DC electrical conductivity. The first term represents the power or heat absorbed by the dielectric and the temperature rise associated with it. The second term represents the heat dissipated with by thermal conduction or convection to the surroundings of the dielectric. Figure 2-2 shows a schematic diagram for heat generation rate and heat loss rate, assuming the heat loss depends linearly on the temperature rise above the ambient temperature (T_0) and the heat generation increases exponentially with temperature. For applied electric field E_2, if the temperature of the dielectric does not increase above T_B, thermal equilibrium will be established. However, for applied electric field E_1, thermal instability will take place at any temperature since the heat generation rate is always larger than the heat loss rate. Analytic solutions for the Eqn. (2-

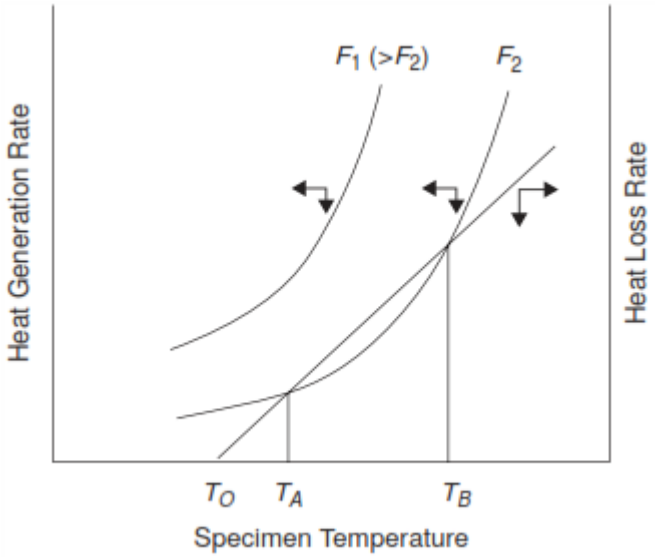

Figure 2-2 Thermal instability in a dielectric specimen for $T>T_B$; T_0 is the ambient temperature[3]. Historically electric field has been given "F" as a variable designation. The variable "E" will be used in this thesis to describe electric field.

1) cannot be obtained for the general case since C_v, κ, and σ may depend on the temperature. At very high electric field, σ can also depend on the electric field (AC or DC). Only for two extreme cases (impulse and steady-state thermal breakdown) the equation can be solved analytically.

In the impulse thermal breakdown situation it is assumed that the heat loss to the surrounding environment plays a negligible role due to a short time scale until the breakdown. Then the Eqn. (2-1) can be simplified to

$$C_v \frac{\partial T}{\partial t} = \sigma E^2 \qquad (2\text{-}2).$$

Assuming a linear increase of electric field with ramp rate of a, E can be given by E= at. If σ can be expressed by the Arrhenius equation of

$$\sigma = \sigma_0 \exp\left(-\frac{E_a}{k_B T}\right) \qquad (2\text{-}3)$$

where σ_0 is the pre-exponential factor, E_a the activation energy, and k_B the Boltzmann constant.

After substituting Eqn. (2-3) into (2-2), separation of variables, and integration of T from T_0 to T and of E from 0 to E yields

$$\frac{k_B T_0^2}{E_a}\left[\exp\left(\frac{E_a}{k_B T_0}\right) - \exp\left(\frac{E_a}{k_B T}\right)\right] \approx \frac{\sigma_0 a^2 t^3}{3C_v} \quad (2\text{-}4)$$

where C_v is assumed to be independent of temperature and $E_a \gg k_B T$ [1]. In this equation the temperature increases very rapidly in a short time. The dielectric undergoes thermal breakdown at the time $t = E/a$ as soon as the temperature of the material overshoots T_B. This type of thermal breakdown has been reported for NaCl and KCl under impulse condition[4, 5]. Hanscomb reported that breakdown strength of NaCl with thickness of about 200 μm at 350 ^oC could be explained by impulse thermal breakdown theory[4]. Linearly increasing voltages were used for the measurement and the time to breakdown was varied between 3.5 ms and 10 s.

In the case of steady-state thermal breakdown a maximum thermal voltage is derived from Eqn. 2-1. This assumes a situation where an infinite area slab with arbitrary thickness is fixed to the ambient temperature (T_0) at its electrode surfaces by a sufficient cooling capacity and the hottest point (T_m) is at the center of the slab. This means that the limiting factor on the dissipation of energy is the thermal insulation given by the dielectric itself. The first term in the Eqn. (2-1) can be ignored assuming that all the generated heat in the dielectric is dissipated to its surroundings. Then the Eqn. (2-1) for the one-dimensional case can be reduced to

$$-\frac{d}{dx}\left(\kappa\frac{dT}{dx}\right) = \sigma\left(\frac{dV}{dx}\right)^2 \quad (2\text{-}5).$$

Using the Arrhenius type of electrical conductivity in Eqn. (2-3), an integration of Eqn. (2-5) for x from the center of the sample to the electrode surface, the maximum thermal voltage (V) is described by

$$V^2 = 8\int_{T_0}^{T_m}\left[\frac{\kappa}{\sigma_0 \exp\left(-E_a/k_B T\right)}\right]dT \quad (2\text{-}6).$$

Further assuming that κ is independent of temperature, the critical maximum thermal voltage (V_c) where the temperature at the hottest point exceeds the melting temperature is

$$V_c \approx \left(\frac{8\kappa k_B T_0^2}{\sigma_0 E_a}\right)^{1/2} \exp\left(\frac{E_a}{2k_B T}\right) \quad (2\text{-}7).$$

For thick specimens, the maximum thermal voltage is independent of thickness. For AC fields where additional dielectric loss generates much more heat, thermal breakdown strength is normally lower than that of DC fields and decreases with increasing frequency of the AC field. Therefore it is important to control the dielectric loss as low as possible for applications of the dielectrics under AC fields. This type of breakdown has been reported for NaCl slabs[1]. Inge et al found that NaCl single crystals with thickness between 1.5 mm and 3.5 mm showed constant breakdown voltage at 700 ^{o}C with voltage rise time of the order of minutes.

2.1.3. Electronic breakdown mechanism

Electronic breakdown is caused by electronic processes such as electronic carrier multiplication and two different electronic breakdown mechanisms are discussed below.

2.1.3.1. Intrinsic breakdown

Intrinsic and electronic breakdown terms are often used interchangeably. The electron energy is governed by two important processes. Electron energy increases with the applied electric field. There is maximum rate of electron energy transfer to the lattice by electron-phonon scattering[2]. Thus there must be a critical field and corresponding electron energy above which electrons indefinitely acquire energy faster than they can lose it, thereby leading to breakdown. Although this mechanism is considered truly intrinsic to the material, in fact mechanisms other than electron-phonon scattering such as inelastic collisions with defects or scattering with other electrons (trapped or free) may also cause energy loss for high-energy electrons.

Electron traps are always present in a dielectric material due to impurities, structural defects or dislocations. Upon an applied field, E, free electrons in the conduction band will acquire energy at a rate of P_e which is given by

$$P_e = \sigma E^2 = \frac{dU}{dt} \tag{2-8}$$

where U is the energy acquired by electrons from the electric field. This energy can be dissipated with electron-electron scattering in the conduction band, electron-trapped electron scattering, and electron-phonon scattering by the lattice vibration from thermal energy. For high-purity crystals with low free electron concentration, the contribution from the first two kinds of scattering is trivial and electron-phonon scattering is the principal factor. Von Hippel has observed that the intrinsic breakdown strength of pure sodium chloride samples increases with temperature below room temperature[6]. The thickness of sodium chloride was between 100 and 200 μm. The breakdown strength was measured with constant voltage, not with linearly increasing voltage. Postulating a mechanism only with electron-phonon scattering, P_e depends on E, U and T (lattice temperature), whereas the energy loss (P_r) depends U and T. Thus the equation for energy balance can be described by

$$P_e = A(E, U, T)$$

$$P_r = B(U, T)$$

$$A(E, U, T) = B(U, T) \tag{2-9}.$$

This breakdown process occurs so rapidly that the energy loss by thermal conduction to the surroundings can be neglected. When P_e is greater than P_r, the dielectric will experience breakdown.

The high-energy (or high-temperature) criterion proposed by Frohlich assumes that the electron temperature (T_e) is always higher than the lattice temperature (T) and the energy obtained by electrons in the field needs some time to be transferred to the lattice. Scattering of

electrons with trapped electrons in crystal with traps may release the trapped electrons and therefore increase electron concentration in the conduction band. Electrical conductivity will in turn increase and result in the increased electron temperature and high-temperature breakdown.

Figure 2-3 shows that breakdown takes place at electron temperature T_e which is accounted within the electron energy, U_1, for applied field E_1.The breakdown is regarded as high-temperature breakdown if T_e is greater than the critical temperature (T_c) which corresponds to the critical energy U_c defined by Frohlich[1]. The average energy gain rate equals the average energy loss rate to the lattice at U_c for a critical field (E_c). The critical field (E_c) is expressed by

$$E_c = C\exp\left(\frac{\Delta E}{2k_B T}\right) \tag{2-10}$$

where C is a constant and ΔE is the average energy difference between the bottom of the conduction band and the excited trap states. The electron temperature (T_c) at the critical field can be determined by

$$\frac{1}{T} - \frac{1}{T_c} = \frac{k_B}{\Delta E} \tag{2-11}.$$

The instability takes place for $U>U_1$ where the electrical conductivity increases rapidly and resulting in final breakdown. In the high-temperature mechanism, the breakdown strength will decrease with increasing temperature. Figure 2-4 shows an example of this type of breakdown reported in NaCl and NaCl+AgCl crystals[1]. The thickness of sodium chloride was between 100 and 200 μm and the breakdown strength was measured with constant voltage. The lower breakdown strength of NaCl with silver impurities is attributed to additional electron scattering and energy loss.

The low-energy (or low-temperature) criterion proposed by von Hippel assumes that the electron-phonon interaction dominates in pure crystals and the energy transfer rate is proportional to the reciprocal of the relaxation time ($\tau(U)$) for energies less than U_c. Assuming the reciprocal of the relaxation time is proportional to $U^{1/2}$, then P_r can be expressed by

$$P_r = C_r U^{1/2} \tag{2-12}$$

where C_r is a constant. When a relaxation time is high, the energy loss rate is small and energy gain rate for electrons increases. For electrons in the conduction band with mean energy U, each electron will gain energy from the field within an average time and dissipate it by interactions with lattice vibrations. Assuming an average time between collisions is τ, the energy gain rate can be expressed as

$$P_e = \frac{q^2 E^2 \tau}{m^*} \tag{2-13}$$

where m^* is the effective mass of the electron. For P_e greater than P_r, the electrons continuously

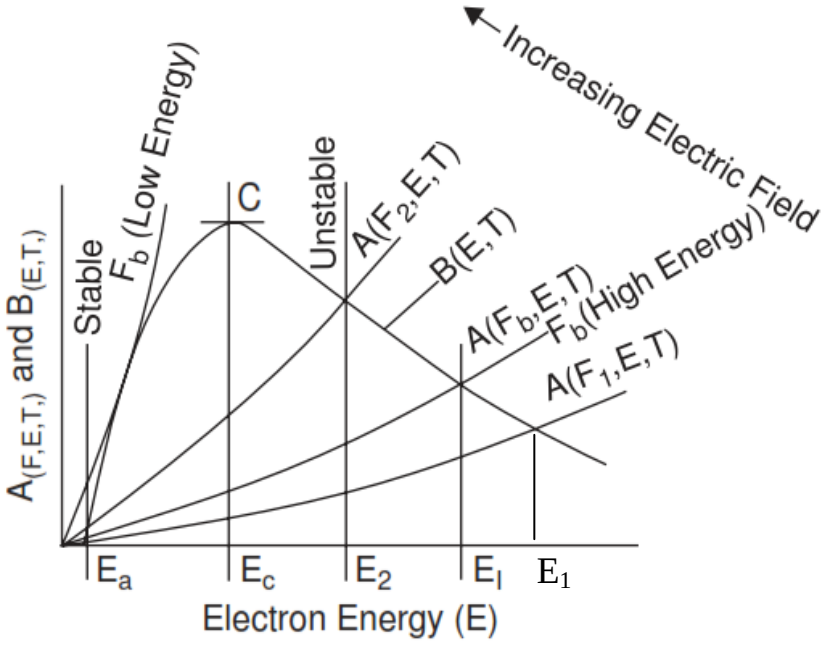

Figure 2-3 The average energy gain rate of electrons A(F,E,T) under the applied electric field F and the average energy loss rate to the lattice B(E,T) as a function of energy E; E_I is the ionization energy and F_b is the breakdown strength[3].

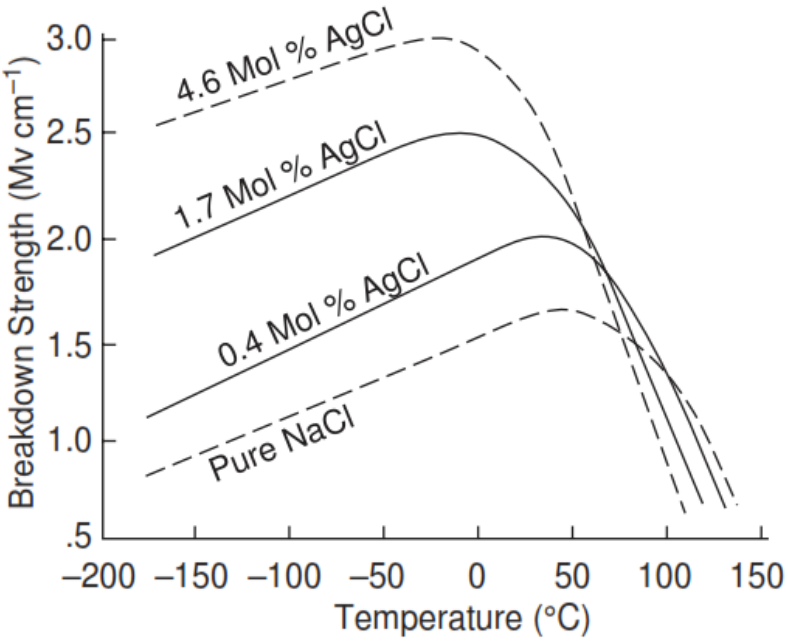

Figure 2-4 Breakdown strength as a function of temperature for pure NaCl crystals and NaCl crystals with AgCl impurities[1].

gain energy from the electric field and may be excited into a state where the electron with high energy can ionize atoms through direct impact. Impact ionization will generate much more free electrons and lead to an exponential increase in current through an avalanche process.

For the low-temperature criterion, breakdown takes place after the critical energy (U_c) is equal to or greater than ionization energy (U_I). Then the critical field (E_c) for breakdown can be obtained by setting Eqn. (2-12) and (2-13) equal and can be expressed as

$$E_c = \frac{1}{q}\left(\frac{C_r m^*}{\tau U_I^{1/2}}\right)^{1/2} \qquad (2\text{-}14).$$

The dependence of E_c on temperature is determined by τ, which is proportional to $T^{-3/2}$. For electron energy greater than U_a shown in Figure 2-3 thermal instability occurs. The temperature dependence of τ on electron-phonon scattering indicates that breakdown strength will increase

with increasing temperature, but not very rapidly. Examples are shown in Figure 2-4 for pure NaCl and NaCl with AgCl impurities. In the lower temperature region in the figure, E_c increases and shifts toward a lower temperature as the concentration of impurities increase. This can be explained if the increase in the concentration of impurities would increase the probability of scattering, thus decreasing the scattering time.

These two models for intrinsic breakdown were applied to alkali halides such as NaCl, KCl, and KBr. These models couldn't adequately explain experimental results although almost all experimental results lie within the boundaries of the estimated critical fields[1]. Both models also assume a homogeneous infinite medium without consideration of the boundary conditions of a finite sample and therefore cannot explain thickness dependence of breakdown strength for alkali halide crystals and other solids. Other assumptions such as a uniform electric field within the material and ignoring charge injection from electrical contacts also provide difficulties for explaining space charge effects and electrode effects on breakdown strength. The other experimental result which cannot be described by these models is light emission from the cathode observed in alkali halide crystals prior to breakdown[3]. Light emission from the cathode was caused by electron injection which is not accounted for in the intrinsic energy models.

2.1.3.2. Avalanche breakdown

Seitz proposed that breakdown in solids is primarily due to electron avalanches, similar to electrical breakdown of gases[7]. In this case high-energy electrons, either as a result of acceleration in the field, or hot injection from the electrode, or purely from chance fluctuations, collide with trapped or bound electrons imparting sufficient energy for both electrons to be free after the collision. Electrons quickly acquire enough energy from the high electric field to each cause a second generation of collisions leading to four free electrons. When this chain reaction continues the local concentration of high-energy electrons increases up to such an extent that

local destruction of the lattice occurs. From the theoretical point of view, if the sample is too thin the electrons may reach the anode before the avalanche has built up to a destructive size.

Forlani and Minnaja proposed an avalanche breakdown model where they considered the consequences of avalanche multiplication of Fowler-Nordheim or Shottky emission current from the cathode rather than taking account of the avalanche multiplication resulting from a single electron starting from the cathode[8]. If the current injection into conduction levels from the cathode is assumed to be given by the Fowler-Nordheim mechanism, the current density at the cathode (J_{cath}) can be expressed by

$$J_{cath} = J_0 \exp\left\{-\frac{4\sqrt{2m^*}\varphi^{3/2}}{3\hbar eE}\right\} \tag{2-15}$$

where J_0 is a field-dependent pre-exponential factor, m* an effective mass of electron, φ the effective height of the potential barrier at the cathode-dielectric interface. If the lattice vibrations in the dielectric are unable to slow down the electrons in a strong field, then the collision-ionization rate per unit length (α) is expressed approximately by

$$\alpha = \frac{eE}{I} \tag{2-16}$$

where I is the ionization energy for the material. The current reaching at the anode (J_{an}) as a result of this collision-ionization multiplication will be described by

$$J_{an} = J_{cath} \exp\left\{-\frac{4\sqrt{2m^*}\varphi^{3/2}}{3\hbar eE} + \frac{eEd}{I}\right\} \tag{2-17}$$

where d is thickness of the material. If it is assumed that zero exponent in Eqn. (2-17) corresponds to critical conditions, then the critical field strength is written by

$$E_c = \left(\frac{4\sqrt{2m^*}\varphi^{\frac{3}{2}}I}{3\hbar e^2}\right)^{1/2} d^{-1/2} \tag{2-18}.$$

Therefore the breakdown strength depends on the inverse square root of the thickness. Experimental results consistent with Eqn. (2-18) have been reported for various inorganic dielectrics such as CaF_2, SiO, CeO_2, and MgF_2 by Budenstein et al[9-11].

However, it was difficult to explain how electrons acquire sufficient energy from the applied field for impact ionization within such a small mean free path in solids. Typical mean free path in SiO_2 films is 3 nm. For electric field of 10^9 V/m the total energy gain for an electron is about 3 eV, which is much lower than the band gap of 9 eV[12]. Later O'Dwyer has explained that if impact ionization is an essential process and there are many ionizing collisions, then the assumption of a uniform field is unphysical[13]. It was pointed out that the positive hole space charges increase the local field near the cathode and thus electron injection. If the electron mobility is much higher than the hole mobility then the electron injection from the cathode plays an important role in breakdown process. Therefore impact ionization and injection lead to a large distortion of electric field which eventually causes breakdown of the solid. This model has been modified to include the effects of electron traps and hole traps additionally by Klein[14].

2.1.4. Electromechanical breakdown mechanism

Electromechanical breakdown is another breakdown mechanism believed to be common in polymer materials under high electric fields due to its low elastic modulus. The attractive force between two parallel electrodes with opposite electric charges will compress the dielectric, decreasing its dimension in the direction of the applied field. The elastic force expressed in a logarithmic relationship between stress and strain for polymers will balance this compressive force. Then a dimensional change in thickness under the applied electric field E can be expressed from the equilibrium between the electrostatic energy and the mechanical energy by

$$\frac{1}{2}\varepsilon_r\varepsilon_0\left(\frac{V}{d}\right)^2 = Y\ln\frac{d_0}{d} \qquad (2\text{-}19)$$

where Y is the Young's modulus, V the applied voltage, d_0 and d are respectively the specimen thickness before and after the application of the field. It is shown by differentiating Eqn. (2-19) in regards to d that a maximum of V takes place when d/d_0 is equal to 0.6. If V is greater than this

critical value, the dielectric turns into an unstable state, leading to a failure. Therefore the breakdown strength (E_b) for this mechanism is expressed by

$$E_b = \frac{V}{d_0} = 0.6\left(\frac{Y}{\varepsilon_r \varepsilon_0}\right)^{1/2} \quad (2\text{-}20).$$

Electromechanical breakdown has been reported for polyethylene and other polymers in the high temperature region since the elastic modulus tends to decrease as temperature increases[15]. This breakdown mechanism has also been reported in $BaTiO_3$ based ceramics[16].

2.1.5. Partial discharge breakdown mechanism

Solid materials such as polymer and ceramics inevitably have small voids even for the carefully prepared cases. These voids are filled with gas which has lower permittivity than that of surrounding host materials. This enhanced field from the dielectric contrast between the void and matrix material may induce the gas to breakdown or discharge within the void at the lower electric field than the intrinsic breakdown strength. This is called as a partial discharge since this local breakdown does not necessarily give rise to the breakdown of a whole material.

Partial discharge breakdown in voids of porous lead zirconate titanate ceramics is reported by Gerson et al. in 1950's[17]. In their analysis it is assumed that voids in the ceramic have one size and are distributed randomly throughout the ceramic. It is also assumed that the voids have zero dielectric breakdown strength. The volume of the ceramic is divided into cubes, the edge dimension of each cube being equal to the linear dimension of the average void. Then the probability of finding a column of n cubes containing x voids is given by

$$W_n(x) = \binom{n}{x}\left[\frac{\rho_0 - \rho}{\rho_0}\right]^n \left[\frac{\rho}{\rho_0}\right]^{n-x} \quad (2\text{-}21)$$

where ρ_0 is the theoretical density of void-free ceramic, ρ the bulk density of porous ceramic. As a critical point the maximum x for the test specimens (x_m) is determined by

$$NW_n(x_m) = 1 \quad (2\text{-}22)$$

where N is the number of columns in test specimens. Then the breakdown field for this column (E_b) is given by

$$E_b = E_0\left(\frac{n-x_m}{n}\right) \quad (2\text{-}23)$$

where E_0 is the breakdown field for the void-free samples. When this model was applied to lead zirconate titanate specimens with diameter of 1.7 cm, thickness of 1.6 mm, and void size of 0.12 mm, the theoretical breakdown strengths as a function of porosity were quite close to the experimental ones[17]. For this specific sample dimension and void size, this model predicted slope of 0.39 for thickness dependence of breakdown strengths in the log E_b vs log thickness plot[17].

The discharge sometimes produces carriers by the ionization which may cause erosion by impacting the opposite wall of the void if they have acquired sufficient energy. This process is related with the formation of electrical trees which is a specific type of electrical degradation in polymer materials[2].

2.1.6. Thickness and temperature dependence of breakdown strengths for breakdown mechanisms

Four different mechanisms for electrical breakdown are discussed above sections. From an application point of view, thickness dependence and temperature dependence of breakdown strengths are important. Moreover, this dependency helps to differentiate different breakdown mechanisms which are also scientifically important.

The thickness dependence of breakdown strength is generally described by

$$E_b = kd^{-n} \quad (2\text{-}24)$$

where k is constant, d the thickness of test samples, n the exponent describing thickness

dependence. For thermal breakdown mechanisms, this relationship is known for steady-state and impulse thermal breakdown. Assumption of steady-state thermal breakdown and field-independent conductivity leads to n=1 for thick slab approximation (temperature distribution within material) and n=0.5 for thin slab approximation (constant temperature within material)[2]. For field-dependent conductivity and steady-state breakdown the exponents rely upon conduction mechanisms and show independence or very weak dependence except space-charge limited conduction which shows n=1[2]. For impulse thermal breakdown it shows independence or weak dependence regardless of field dependence.

For electronic breakdown the intrinsic mechanism is independent of thickness. The avalanche mechanism shows strong dependence on thickness for which Fowler-Nordheim and Schottky emission result in n=0.5 and n=1[8]. Meanwhile, breakdown strength for electromechanical mechanism is independent of thickness. For the case of partial discharge breakdown it depends on the specimen dimension and void size and the thickness dependence shows n=0.39 for a case of lead zirconate titanate with dimension of diameter of 1.7 cm, thickness of 1.6 mm, and void size of 0.12 mm[17]. This thickness dependence of breakdown strength is summarized in Table 2-1.

Experimental and theoretical studies of the temperature dependence of breakdown strength are also important technically as well as scientifically. For steady-state thermal breakdown field-independent conductivity leads to exponentially decreasing strength with temperature and field-dependent conductivity leads to monotonously decreasing strength with temperature[1]. For impulse thermal case breakdown strength decreases exponentially with temperature for field-independent conductivity[1]. On the other hand, for electronic breakdown intrinsic mechanism shows exponentially decreasing strength with temperature and avalanche mechanism is independent of temperature[1, 2]. Temperature dependence of electromechanical breakdown strength rely on temperature dependence of Young's modulus[2]. For the last partial

discharge breakdown strengths is independent of temperature[17]. The temperature dependence of breakdown strength is summarized in Table 2-2.

Table 2-1 Thickness dependence of breakdown strengths for different mechanisms.

Mechanisms		Electrical conductivity		Thickness dependence	Notes	References
Thermal breakdown	Steady-state	Field-independent (Arrhenius type)	Thick samples	$E_b \propto d^{-1}$	T distribution within material	[2]
			Thin samples	$E_b \propto d^{-0.5}$	Constant T within material	
		Field-dependent	Klein model	$E_b \propto -\ln d$	Weak dependence on d	
			Schottky emission	$E_b \approx$ constant		
			Space charge limited	$E_b \propto d^{-1}$		
			Poole-Frenkel	$E_b \propto -\ln d$	Weak dependence on d	
	Impulse-state	Field-independent		$E_b \approx$ constant		
		Field-dependent	Klein	$E_b \propto -\ln d$	Weak dependence on d	
			Poole-Frenkel	$E_b \approx$ constant		
Electronic breakdown	Intrinsic			$E_b \approx$ constant		[2]
	Avalanche		Fowler-Nordheim emission	$E_b \propto d^{-0.5}$		[8]
			Schottky emission	$E_b \propto d^{-1}$		
Electromechanical breakdown				$E_b \approx$ constant		[18]
Partial charge breakdown				$E_b \propto d^{-0.39}$	different n with sample dimension and void size	[17]

Table 2-2 Temperature dependence of breakdown strengths for different mechanisms.

Mechanisms		Electrical conductivity	Temperature dependence	Notes	References
Thermal breakdown	Steady-state	Field-independent (Arrhenius type)	$E_b \propto \exp(\varphi/2k_BT)$	φ is activation energy	[1]
		Field-dependent (Klein model)	$E_b \propto -aT$	a is constant	
	Impulse-state	Field-independent (Arrhenius type)	$E_b \propto \exp(\varphi/2k_BT)$	φ is activation energy	
Electronic breakdown	Intrinsic		$E_b \propto \exp(\Delta E/2k_BT)$		[3]
	Avalanche		$E_b \approx$ constant		[1]
Electromechanical breakdown			$E_b \propto Y(T)$	Dependence of Young's modulus on T (Y(T))	[2]
Partial charge breakdown			$E_b \approx$ constant		[17]

2.2. Electrical conduction under high electric fields

Electrical conduction, especially under high electric field, plays an important role in both electrical breakdown phenomena and electrical degradation phenomena. These high-field conduction theories are divided into two groups as shown in Table 2-3; electrode-limited mechanisms and bulk-limited mechanisms. This table also shows the electric field dependence for each conduction theory. Schottky and Fowler-Nordheim theories belong to the electrode-limited mechanism and Poole-Frenkel, hopping and space-charge limited conduction theories belong to the bulk-limited mechanism.

Table 2-3 High field conduction mechanisms and their electric field dependency; J: current density, J_0: pre-exponential factor for current density, β_s: Schottky coefficient, E: electric field, k_B: Boltzmann constant, T: absolute temperature, A,B: constant for Fowler-Nordheim equation, σ: electrical conductivity, σ_0: pre-exponential factor for electrical conductivity, β_{PF}: Poole-Frenkel coefficient, e: elementary charge, E_a: activation energy for conduction, ε: permittivity, μ: mobility, V: applied voltage, d: thickness.

Mechanisms		Electric field dependency
Electrode-limited mechanism	Schottky	$J = J_0 \exp\left(\frac{\beta_s \sqrt{E}}{k_B T}\right)$
	Fowler-Nordheim	$J = AE^2 \exp\left(-\frac{B}{E}\right)$
Bulk-limited mechanism	Poole-Frenkel	$\sigma = \sigma_0 \exp\left(\frac{\beta_{PF} \sqrt{E}}{2k_B T}\right)$
	Hopping	$J = J_0 \sinh\left(\frac{eEa}{2k_B T}\right)$
	Space-charge limited	$J = \frac{9}{8} \varepsilon \mu \frac{V^2}{d^3}$

2.2.1. Electrode-limited conduction mechanisms

Electron or hole injection arise above a critical electric field, and these charge carriers contribute conduction in the dielectric. The interface between the electrode and the dielectric plays an important role in these conduction processes. When an electrode is placed in contact with the dielectric, free carriers will transport between them until the Fermi levels become identical. Ideally in the absence of surface states, the difference of work function between the electrode and the dielectric is a crucial factor for the carrier movement.

Two kinds of electrical contact are possible between the electrode and the dielectric; ohmic contact, and blocking contact[3]. Figure 2-5 shows blocking and ohmic contacts based on the energy band diagram where E_{Fm} is the Fermi level of the electrode, E_F the Fermi level of the dielectric, χ the electron affinity of the dielectric, E_c the lowest conduction band of the dielectric, E_V the highest valence band of the dielectric, E_G the band gap of the dielectric, $E_{F'}$ the Fermi level of the contact, and φ_B the potential barrier height at the interface. Blocking contacts are established when the work function of the electrode (φ_m) is greater than the work function of the dielectric (φ). For blocking contacts the flow of electrons from the electrode to the dielectric is blocked by the energy barrier. Therefore this results in a positively charged depletion region in the dielectric area near the interface. For ohmic contacts, where $\varphi_m < \varphi$, electrons flow from the electrode to the dielectric, leading to a negatively charged area near the interface. The potential barrier at the interface will ideally be defined by the work function of the electrode and the electron affinity of the dielectric. However, practically the surface states formed by structural

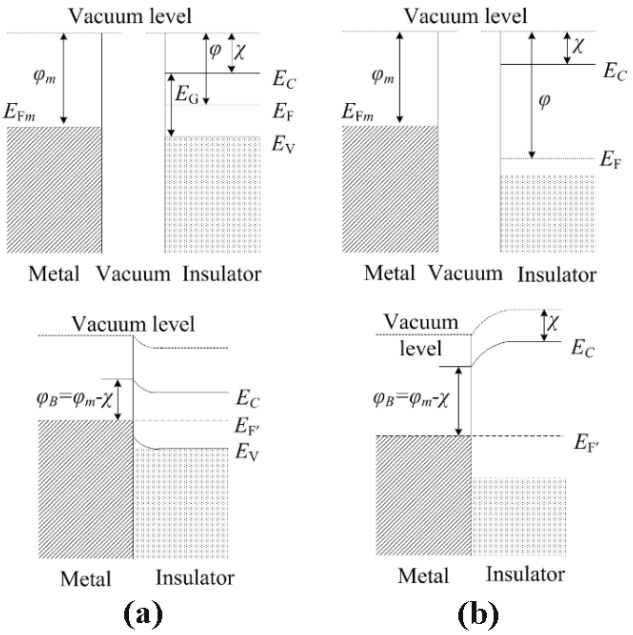

Figure 2-5 Energy band diagram for electrical contacts between electrode and an n-type dielectric;(a) blocking contact (b) ohmic contact[3].

defects and/or impurities will determine the actual potential barrier height, which affects the electrical performance.

2.2.1.1 Schottky conduction mechanism

The flow of electrons from the electrode to the dielectric is impeded by the potential barrier at the interface. This potential barrier height can be reduced by an applied electric field and the image force from charges at the electrode, leading to the enhanced electron injection through the interface. The potential barrier before applying electric field can be defined by

$$\varphi_B = \varphi_m - \chi \qquad (2\text{-}25).$$

After applying the field, the potential barrier height ($\Psi(x)$) will be reduced to

$$\Psi(x) = \varphi_m - \chi - \frac{q^2}{16\pi\varepsilon x} - qEx \qquad (2\text{-}26),$$

where the third term on the right side is the contribution from image charges (q) and the fourth term is the contribution from the applied field as shown in Figure 2-6. The applied field forces the electrons to move towards the anode, while the image charges induced at the electrode attract emitted electrons towards the cathode. The balance between these forces gives rise to the equilibrium position where the net force on electrons is zero and the potential Ψ(x) is at minimum. This point can be determined by making the derivative of Eqn. (2-26) with respect to x zero. Hence the equilibrium point x_{min} can be expressed as

$$x_{min} = \left(\frac{q}{16\pi\varepsilon E}\right)^{1/2} \qquad (2\text{-}27).$$

The amount of a decrease for the potential barrier height can also be evaluated from x_{min}, which can be evaluated by

$$\Delta\varphi_B = \left(\frac{q^2}{16\pi\varepsilon x}\right) + qEx = \left(\frac{q^3 E}{4\pi\varepsilon}\right)^{1/2} \qquad (2\text{-}28).$$

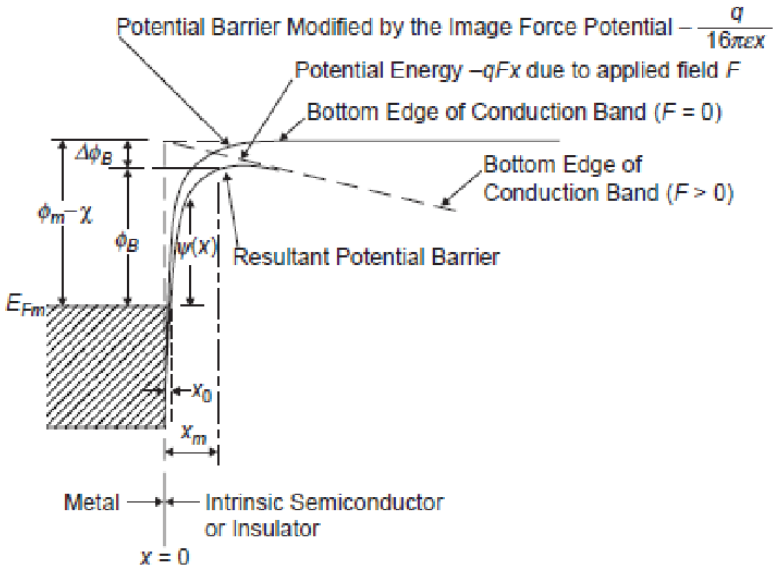

Figure 2-6 The decrease of potential barrier between the electrode and the dielectric from the image forces and the applied field[3].

Then the minimum potential barrier height will be

$$\Psi = \varphi_B - \Delta\varphi_B = \varphi_m - \chi - \left(\frac{q^3 E}{4\pi\varepsilon}\right)^{1/2} \quad (2\text{-}29).$$

The current density for thermionic emission of electrons from the electrode is given by the Richardson-Dushman equation, which can be expressed as

$$J = AT^2 \exp\left(-\frac{\Psi}{k_B T}\right) \quad (2\text{-}30)$$

where A is the Richardson constant. After substituting the potential barrier height by Eqn. (2-29), the current density will be

$$J = AT^2 \exp\left(-\frac{\varphi_B}{k_B T}\right) \exp\left(\frac{1}{k_B T}\left(\frac{q^3 E}{4\pi\varepsilon}\right)^{\frac{1}{2}}\right) \quad (2\text{-}31).$$

This current density equation from thermionic emissions expresses the Schottky conduction mechanism.

2.2.1.2 Fowler-Nordheim tunneling mechanism

A field emission process is also possible for electron transfer from an electrode to a dielectric through a potential barrier, which involves the quantum mechanical tunneling of electrons. Under a high electric field and at low temperature there is a probability for electrons to tunnel through the potential barrier into a conduction band of the dielectric. The shape of the potential barrier, the wave function for electrons, and the applied field will influence this probability. The current density for this field emission process is called the Fowler-Nordheim tunneling and can be defined by

$$J = \frac{q^3 m_0 E^2}{8\pi h m_e \varphi_B} \exp\left(-\frac{8\pi\sqrt{2m_e}}{3qhE}\varphi_B^{\frac{3}{2}}\right) \quad (2\text{-}32),$$

where q is the electronic charge, m_0 the mass of free electron, m_e the effective mass of tunneling

electron, E the applied field, h the Planck constant, φ_B the potential barrier height. Assuming m_e and m_0 are m, this current density can be further reduced to

$$J = \frac{q^3 E^2}{8\pi h \varphi_B} \exp\left(-\frac{8\pi\sqrt{2m}}{3qhE}\varphi_B^{\frac{3}{2}}\right) \quad (2\text{-}33).$$

Note that unlike the Schottky mechanism, current density is independent of temperature for the Fowler-Nordheim mechanism.

2.2.2. Bulk-limited conduction mechanisms

The low conductivity of dielectrics is related with their relatively large band gap in comparison to semiconductors. However, the conduction mechanisms for insulators and semiconductors are similar. For both insulators and semiconductors, the conduction mechanism may change depending on the applied electric field. For example, Figure 2-7 shows the typical current-field relationship for a polyimide on p-Si where different slopes suggest different conduction mechanisms depending on the field intensity. Bulk processes play an important role in conduction phenomena in addition to the charge injection from electrodes. Under high electric fields space charges can be accumulated within the dielectric and modify the local electric field. In region II of Figure 2-7, the current in the first ramp cycle is much larger than that in the second and the third cycles at the same electric field, indicating the buildup of a negative space charge which restricts current flow across the electrode-dielectric boundary. The understanding of bulk-limited conduction mechanisms in conjunction with electrode-limited conduction mechanisms will provide a path to understanding the electrical breakdown and the electrical degradation process. In this section bulk-limited conduction mechanisms such as hopping mechanism, Poole-Frenkel mechanism, and space-charge limited current will be discussed.

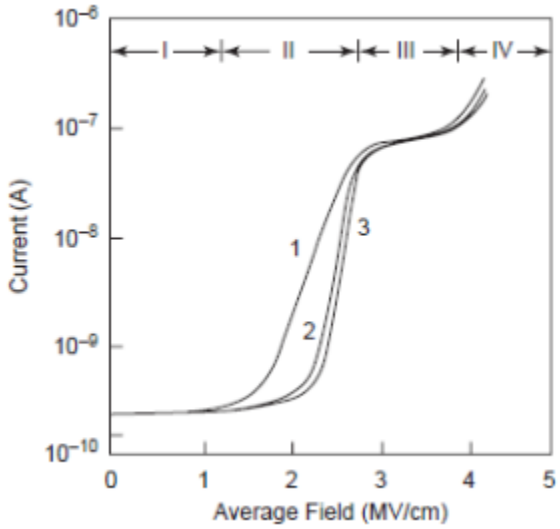

Figure 2-7 Typical current-field relationship for a polyimide film on p-Si with the ramp rate of 0.026 $MVcm^{-1}s^{-1}$; I: displacement current, II: Fowler-Nordheim emission, III: Poole-Frenkel detrapping, IV: double injection. 1, 2, and 3 denote the first, second, and third ramp cycle[3].

2.2.2.1 Hopping mechanism

For amorphous materials including semicrystalline solids such as polyethylene, localized electronic states are created through the structural disorder. Structural disorders and impurities also create localized energy states in the band gap which act as trap sites for free carriers and limit the charge transport. Figure 2-8 shows a schematic diagram of energy band for amorphous material. Although it is difficult for electrons to overcome the large band gap, there is a possibility for electrons to hop over or tunnel through the potential barrier between localized states below the conduction band. This will contribute the charge transport in amorphous material.

The energy of excited electrons, the shape of the potential barrier, and the separation distance between trap sites can determine the type of transport (hopping or tunneling). This mechanism can also be applied to the hole transport for trap sites above the valence band.

If there are a series of trap sites with a single energy level of φ which are separated by the distance a, trapped electrons in these sites can leap over the potential barrier upon thermal stimulus. The probability for electrons to hop over the barrier per unit time can be expressed as

$$P = \nu \exp\left(-\frac{\varphi}{k_B T}\right) \tag{2-34}$$

where ν is the attempt-to-escape frequency. Then the hopping mobility for electrons can be given by

$$\mu = \frac{q\nu a^2}{k_B T} \exp\left(-\frac{\varphi}{k_B T}\right) \tag{2-35}.$$

Upon the applied electric field E, the potential barrier will tilt down in the direction of field, leading to the lowering of the barrier height given by

$$\varphi - \frac{1}{2} qaE \tag{2-36}.$$

Then the current density for the hopping mechanism can be expressed as

$$J = 2qn\nu a \exp\left(-\frac{\varphi}{k_B T}\right) \sinh\left(\frac{qEa}{2k_B T}\right) \tag{2-37}$$

where n is the concentration of charge carriers.

2.2.2.2 Poole-Frenkel effect

Trapped electrons in localized states can also transport into the conduction band within dielectrics from an internal Schottky effect. This effect will reduce the potential barrier height by the columbic interaction induced by a positively charged ionic center which can be created from dissociation under high applied field. Contrary to the Schottky effect from image forces at electrodes, the columbic force in the Poole-Frenkel effect results in the decrease of potential barrier height as large as twice that of the Schottky effect. Thus the lowering of the potential barrier height is given by

$$\Delta\varphi_{PF} = \beta_{PF}E^{1/2} = 2\beta_{Sch}E^{1/2} = (\frac{q^3E}{\pi\varepsilon})^{1/2} \quad (2\text{-}38)$$

where β_{Sch} is the Schottky constant, β_{PF} the Poole-Frenkel constant. From this result the conductivity for the Poole-Frenkel effect in the dielectric can be defined by

$$\sigma = \sigma_0 \exp(\frac{\beta_{PF}E^{1/2}}{2k_BT}) \quad (2\text{-}39)$$

where σ_0 is the low-field conductivity of the dielectric.

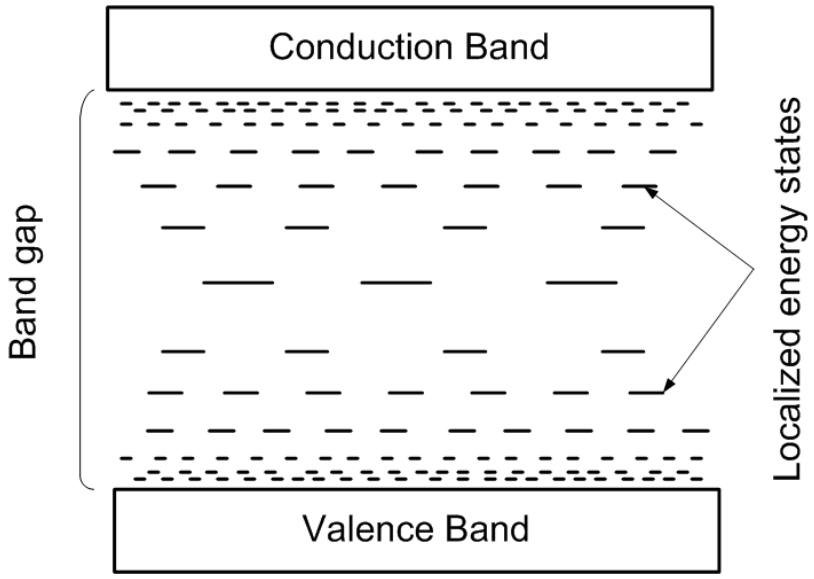

Figure 2-8 A schematic diagram of energy band in amorphous material.

2.2.2.3 Space-charge limited conduction

The space-charge-limited conduction in solids describes the current due to space charges injected from electrodes. Originally this conduction mechanism was proposed by Mott and Gurney[19] and further developed by Rose[20] and Lampert[21, 22]. This mechanism can be applied to perfect solids without traps or solids with traps. For the latter case the trap energy level can be single or exponentially distributed or uniformly distributed[22]. The type of charge injection can be a single injection (electrons or holes) or double injection (electrons and holes). For solids without traps, several assumptions are necessary to further proceed with this theory:

(1) Ohmic contact is assumed for the charge injecting electrode.

(2) A single type of charge carriers is introduced from the electrode into solids.

(3) The mobility of charge carriers is independent of the applied field.

(4) The diffusion of charge carriers is ignored.

If holes are injected into a dielectric, a positive space charge is accumulated and this tends to limit the rate of further hole injection. The current density under an applied field can be described by

$$J = q\mu_h n_h(x)E(x) \tag{2-40}$$

where μ_h is the hole mobility, $n_h(x)$ the hole concentration within the dielectric, E(x) the electric field within the dielectric, x the thickness from the anode. The electric field within the dielectric can be described by Poisson's equation,

$$\frac{dE(x)}{dx} = \frac{qn_h(x)}{\varepsilon} \tag{2-41}$$

where ε is the permittivity of the dielectric. After substituting Eqn. (2-41) into Eqn. (2-40), the current density can be expresses as

$$J = \varepsilon\mu_h E(x)\frac{dE(x)}{dx} \tag{2-42}.$$

Integration of Eqn. (2-42) with the boundary conditions of E(0)=0 and $\int_0^d E(x) = V$ leads to the Mott and Gurney square law,

$$J = \frac{9}{8}\varepsilon\mu_h\frac{V^2}{d^3} \tag{2-43}$$

where V is the applied voltage, d the specimen thickness. When the applied field is low, the current density will be determined by ohmic conduction since the thermally generated carrier density (n_0) is much greater than that of space charge carriers. The ohmic conduction can be expressed as

$$J_{ohmic} = qn_0\mu_h\frac{V}{d} \tag{2-44}.$$

When the applied field increases, the conduction mechanism shifts from the ohmic conduction into the space-charge-limited conduction as shown in Figure 2-9. The transition voltage (V_{tr}) between them can be defined by

$$V_{tr} = \frac{8qn_0d^2}{9\varepsilon} \tag{2-45}.$$

These relationships are only valid for trap-free dielectrics. However, there are always traps generated by structural defects and impurities which interfere with charge carriers and reduce their mobility. Moreover, the distribution of trap energy levels can be generalized by a single level of trap energy, an exponential distribution of trap energy, and a uniform distribution of trap energy. Thus the space-charge-limited conduction for trap-free dielectrics has been modified to take the effects of traps into account[22]. For a single level of trap energy the space-charge-limited current density can be expressed as

$$J = \frac{9}{8}\varepsilon\mu_h\theta\frac{V^2}{d^3} \tag{2-46}$$

where θ is the ratio of free carrier density to the total carrier density which includes both the trapped carriers and free carriers.

2.2.2.4 Classification of space charge

Upon the applied field charges can be injected from electrodes into dielectrics by thermionic emission or field emission and also be generated by dissociation of impurities inside dielectrics. When these charges such as electrons, holes, and ions accumulate within the bulk of dielectric or at interfaces between electrodes and dielectrics they are called as space charges. These charges can drift within the dielectric under the electric field or be captured by trap sites.

Space charges can be divided into two groups : homocharges and heterocharges. When a same polarity of charges is present near electrodes, they can be described by homocharges. Meanwhile, when an opposite polarity of charges exists near electrode, they can be described by heterocharges. Charge injection from electrodes can result in homocharges within dielectrics. Electrons can be injected from the cathode and holes from the anode. On the other hand, heterocharges can be generated from ionization. Impurities within dielectric may be dissociated

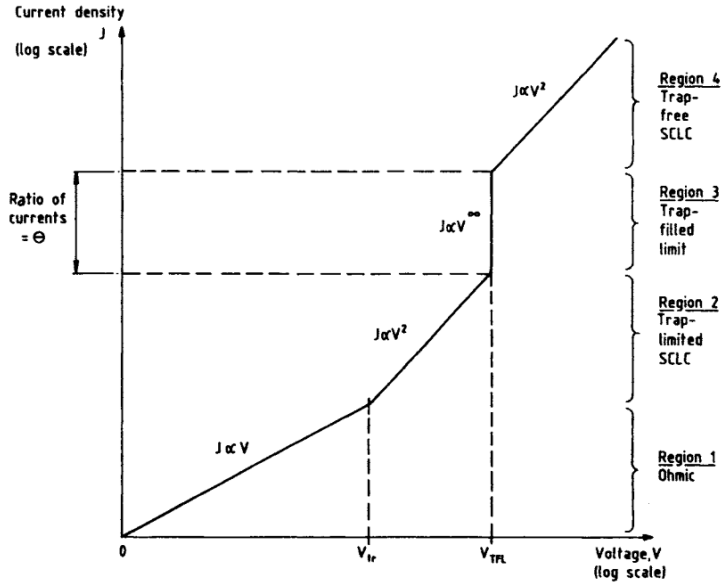

Figure 2-9 A schematic graph of current density versus voltage for the space-charge-limited current[2].

under high electric field and create electrons and a positively charged ions. These can be attracted to the electrode with an opposite polarity and build heterocharges.

2.3. Summary

In this chapter, the fundamental mechanisms for electrical breakdown are first discussed. There are four different breakdown mechanisms including electronic breakdown, thermal breakdown, electromechanical breakdown and partial discharge breakdown. Among them electronic and thermal breakdown mechanisms can be connected with the electrical conduction under high electric fields through local electric field and joule heating. Therefore high field conduction mechanisms for dielectrics are also reviewed as a second part.

2.4. References

1. O'Dwyer, J.J., *The theory of electrical conduction and breakdown in solid dielectrics*. 1973: Clarendon Press Oxford.
2. Dissado, L.A. and J.C. Fothergill, *Electrical degradation and breakdown in polymers*. Vol. 9. 1992: Peter Peregrinus Ltd.
3. Kao, K.C., *Dielectric phenomena in solids*. 2004: Academic Press.
4. Hanscomb, J.R., *High temperature electrical breakdown in sodium chloride.* Australian Journal of Physics, 1962. **15**(4): p. 504-512.
5. Hanscomb, J., *Thermal breakdown caused by field-enhanced conduction in alkali halides.* Journal of Physics D: Applied Physics, 1969. **2**(9): p. 1327.
6. Von Hippel, A. and R. Maurer, *Electric breakdown of glasses and crystals as a function of temperature*. Physical Review, 1941. **59**(10): p. 820.
7. Seitz, F., *On the theory of electron multiplication in crystals.* Physical Review, 1949. **76**(9): p. 1376.
8. Forlani, F. and N. Minnaja, *Electrical Breakdown in Thin Dielectric Films.* Journal of Vacuum Science and Technology, 1969. **6**(4): p. 518-526.
9. Budenstein, P.P. and P.J. Hayes, *Breakdown Conduction in Al-SiO-Al Capacitors.* Journal of Applied Physics, 1967. **38**(7): p. 2837-2851.
10. Budenstein, P.P., et al., *Destructive Breakdown in Thin Films of SiO, MgF_2,CaF_2,CeF_3, CeO_2 and Teflon.* Journal of Vacuum Science and Technology, 1969. **6**(2): p. 289-303.
11. Smith, J.L. and P.P. Budenstein, *Dielectric Breakdown in Thin Evaporated Films of CaF_2, MgF_2, NaF, and LiF*. Journal of Applied Physics, 1969. **40**(9): p. 3491-3498.

12. Fischetti, M.V., et al., *Theory of high-field electron transport in silicon dioxide.* Physical Review B, 1985. **31**(12): p. 8124.
13. O'Dwyer, J., *Theory of high field conduction in a dielectric.* Journal of Applied Physics, 1969. **40**(10): p. 3887-3890.
14. Klein, N., *Electrical breakdown of insulators by one-carrier impact ionization.* Journal of Applied Physics, 1982. **53**(8): p. 5828-5839.
15. Fava, R. *Intrinsic electric strength and electromechanical breakdown in polythene*. in *Proceedings of the Institution of Electrical Engineers*. 1965: IET.
16. Kishimoto, A., K. Koumoto, and H. Yanagida, *Mechanical and dielectric failure of $BaTiO_3$ ceramics.* Journal of Materials Science, 1989. **24**(2): p. 698-702.
17. Gerson, R. and T.C. Marshall, *Dielectric Breakdown of Porous Ceramics.* Journal of Applied Physics, 1959. **30**(11): p. 1650-1653.
18. Stark, K. and C. Garton, *Electric strength of irradiated polythene.* 1955.
19. Mott, N.F. and R.W. Gurney, *Electronic processes in ionic crystals*. 1964: Dover New York.
20. Rose, A., *Space-charge-limited currents in solids.* Physical Review, 1955. **97**(6): p. 1538.
21. Lampert, M.A., *Simplified theory of space-charge-limited currents in an insulator with traps.* Physical Review, 1956. **103**(6): p. 1648.
22. Lampert, M.A., *Volume-controlled current injection in insulators.* Reports on Progress in Physics, 1964. **27**: p. 329.

Chapter 3: High Electric Field Conduction in Low-alkali Boroaluminosilicate Glass

3.1. Introduction

Low-alkali boroaluminosilicate glass material is a promising candidate for high energy density capacitor applications due to its high breakdown strength. DC breakdown strength as high as $1.2x10^9$ V/m was reported for commercial boroaluminosilicate glass and energy density calculation showed a value exceeding 30 J/cm^3 for laboratory size samples[1-3]. It is important to understand the electrical conduction mechanism under high electric field in the glass system since it is closely linked to breakdown strength. Leakage currents in ceramic and polymer insulators have been understood with several conduction mechanisms including Schottky emission, Fowler-Nordheim tunneling, Poole-Frenkel emission, space-charge-limited current, and hopping conduction[4-18]. Conduction mechanisms for glasses have also been studied with the primary focus on the hopping conduction on glasses with transition metal ions or ionic conduction on glasses with alkali ions[19-21]. In this chapter the field, thickness, and temperature dependence of the leakage currents for low-alkali boroaluminosilicate(Schott AF 45) will be discussed to determine conduction mechanism under high electric field.

3.2. Electrical measurement condition

Commercial low-alkali boroaluminosilicate glass (AF 45 manufactured by Schott Glass) samples with weight percent composition of 49.6 SiO_2-14.2B_2O_3-11.4Al_2O_3-24.1BaO and 400 ppm of Na were chemically etched from 50 μm thickness to 5 ~ 14 μm of thickness range.

Platinum was deposited with an area of 1.583 mm^2 and a thickness of 50 nm for both top and bottom electrodes. Electrical measurements were performed through the thickness of layer using a pA meter (4140B, Hewlett Packard) and amplifier (Model BOP 1000M, KEPCO). The DC leakage currents were measured using a step voltage technique in the temperature range of 323 ~ 498 K. While charging the dielectric, current density decreased monotonically with time and reached the steady state DC leakage regime after about 1200s. Thus all of the reported measurement for leakage currents was performed after 1200s in order to measure leakage current in the steady state.

3.3. Current-voltage behavior in AF45 glass

The I-V characteristics of metal/glass/metal structure with a 5 μm thick glass have been measured as a function of temperature and the results are shown in Figure 3-1(a). Two distinct regimes may be distinguished: at low fields, the current density increases approximately linearly with voltage; at higher fields, non-linear behavior is observed. The current flowing through the glass capacitor increased with increasing temperature and decreased with increasing glass thickness. The reported I-V curves are reproducible, and the non-linearity of the I-V characteristics indicates that the prevalent conduction mechanism is non-ohmic. In order to determine a conduction mechanism, the I-V data shown in Figure 3-1(a) were fitted with various models, including electrode-limited as well as bulk-limited conduction models. Figure 3-1(b) shows the bulk conductivity of the glass capacitor measured as a function of electric field and temperature. It could be assumed that the applied electric field reduces energy barrier for charge transport and the temperature aids in the thermal excitation of charged carriers. Consequently, the bulk conductivity increases with increasing electric field and temperature. Figure 3-1(c) shows the I-V curves measured at 473 K as a function of glass thickness. , and non-linearity was

observed in all samples with different thicknesses. Bulk conductivity based on the Figure 3-1(c) is presented in Figure 3-1(d). It is clear that the bulk conductivity depends on the glass thickness and is proportional to applied field.

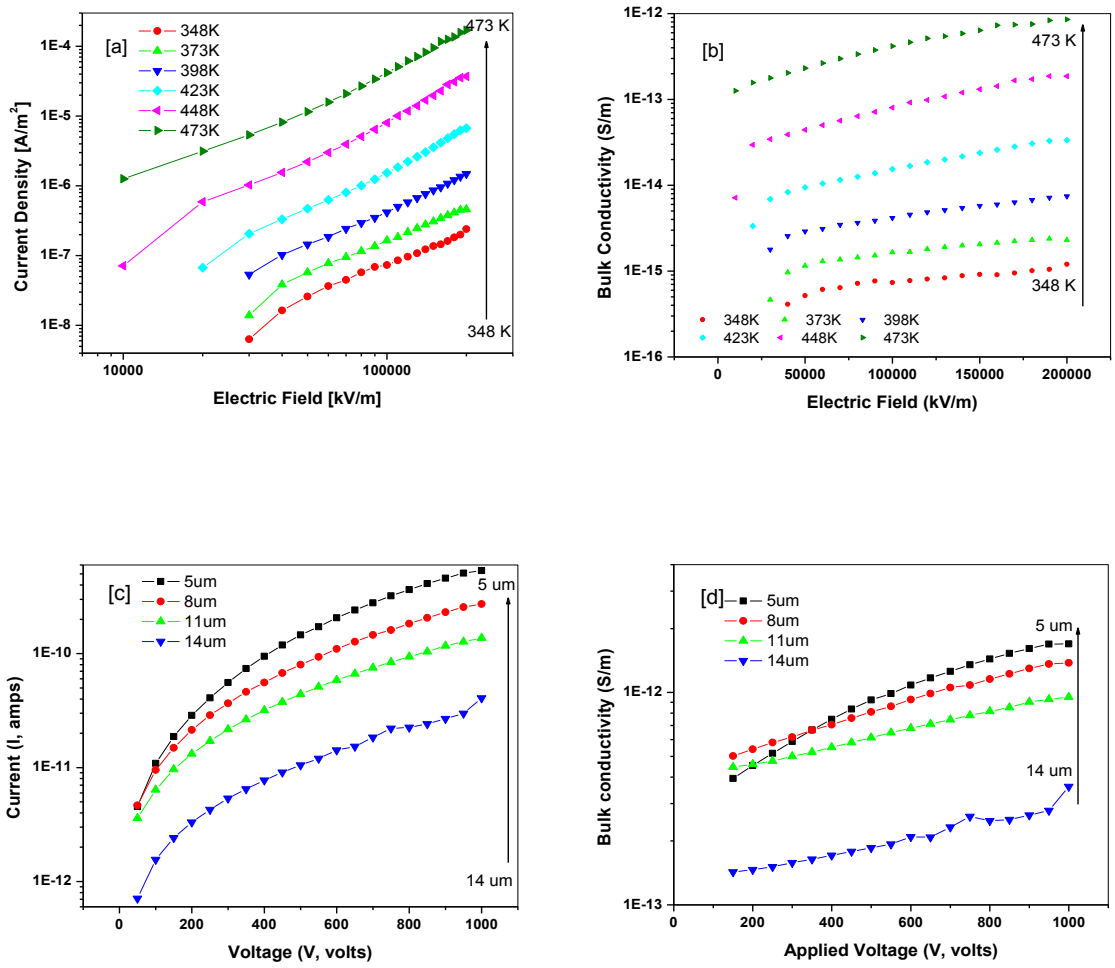

Figure 3-1 (a) I-V curves measured for 5 μm thick glass capacitor as a function of temperature, (b) bulk conductivity of 5 μm glass capacitor as a function of field and temperature, (c) I-V curves measured at 473 K as a function of thickness, and (d) bulk conductivity dependence on the glass thickness at 473 K.

3.4. Application of electrode-limited conduction mechanism

Electrode-limited conduction mechanisms can be divided into Schottky and Fowler-Nordheim types depending on the electron emission process from an electrode to the dielectric. In the Schottky mechanism, electron transfer takes place by thermionic emission which is field and temperature dependent. On the other hand, in the Fowler-Nordheim mechanism a quantum tunneling process contributes to an electron transfer over the potential barrier and it is temperature independent.

3.4.1. Application of Schottky mechanism to electrical conduction for AF45 glass

The Schottky emission current (J) can be described by

$$J = AT^2 \exp\left(-\frac{q\Phi_B}{k_B T}\right) \exp\left(\frac{\beta_s \sqrt{E}}{k_B T}\right)$$

$$\beta_S = \left(\frac{q^3}{4\pi\varepsilon_r\varepsilon_0}\right)^{1/2} \qquad (3\text{-}1)$$

where A is the Richardson coefficient, T the absolute temperature, q the elementary charge, Φ_B the Schottky barrier height, k_B the Boltzmann constant, β_s the Schottky coefficient, E the electric field, ε_r the relative permittivity, ε_0 the permittivity of the free space. It is clear from Eqn. (3-1) that the logarithm of the current is a linear function of the square root of the field strength if the Schottky mechanism holds. Figure 3-2 shows the Schottky plot for 5 μm AF 45 glass sandwiched between Pt electrodes for different temperatures. For temperatures between 348 and 473 K, there is a linear relationship for current density vs square-root of voltage. The slopes in Figure 3-2 are related to the relative permittivity as described in. The calculated permittivity values Eqn. (3-1) are summarized in Table 3-1 and the permittivity values decrease from 13 to 5.5 with increasing

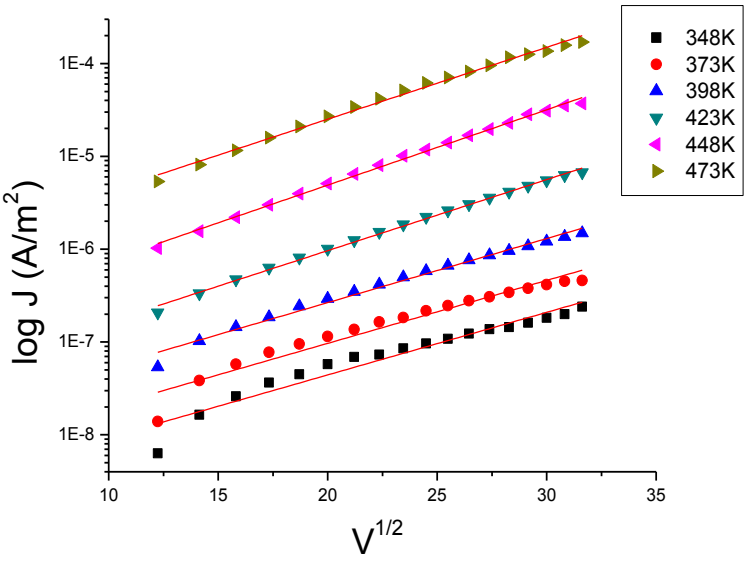

Figure 3-2 Schottky plots for 5 μm glass capacitor for different temperatures. Symbols are the measurements and solid lines are fits to the data.

Table 3-1 Permittivities calculated from slopes in Schottky plots for 5 μm AF 45 glass capacitors.

Temperature (K)	Slope	β_s	ε_r
348	0.067	0.000345	13
373	0.068	0.000350	11
398	0.069	0.000355	9.7
423	0.076	0.000391	7.1
448	0.081	0.000417	5.5
473	0.077	0.000397	5.5

temperature. If the electrons have a high velocity and move through the barrier in a short time with respect to the period of a long wavelength longitudinal optical phonon, then the interaction between injected electrons and phonons is very limited[22]. Then the permittivity in Eqn. (3-1) is the optical permittivity which is given by the square of the refractive index. The refractive index of AF 45 glass is 1.52 and therefore the optical permittivity is about 2.3. Compared to permittivities at several temperatures in Table 3-1, the optical permittivity has a value more than two times. It is noteworthy that the calculated permittivity from 423 to 473 K is close to the static permittivity measured at 1 MHz and room temperature (6.0) [1]. Actually, the use of both the static and the optical permittivity have been proposed for Schottky conduction mechanism for insulators[23-25]. The key issue is how fast a carrier is assumed to move in the dielectric materials. A fast carrier induces only the electronic component of the polarization and the dielectric response should be optical. On the other hand, if the carrier is slow, such as in the polaron model, then the static permittivity should be used[26]. The thickness of glass is 5 μm and therefore there is a high possibility for the interaction between injected electrons and phonons. This can explain why the calculated permittivity is similar to the static permittivity.

The potential barrier between Pt electrode and the glass can be obtained from the slope if the logarithm of J/T^2 is plotted with the 1/T where J is an extrapolated current density at zero voltage. Figure 3-3 shows this plot and the potential barrier from the linear slope is 0.85 eV. The lower potential barrier between 348 and 398 K may comes from non-steady state condition[22]. The ideal potential barrier can be determined from work function of electrode and electron affinity of dielectric materials. The work function of Pt electrode is about 5.6 eV. The electron affinity of AF 45 glass is unknown. If it is assumed that the electron affinity of AF 45 glass is similar to that of borosilicate glass(4.5 eV), the potential barrier will be 1.1 eV[27]. Considering surface states can affect the potential barrier, the calculated potential barrier from Figure 3-3 is reasonable.

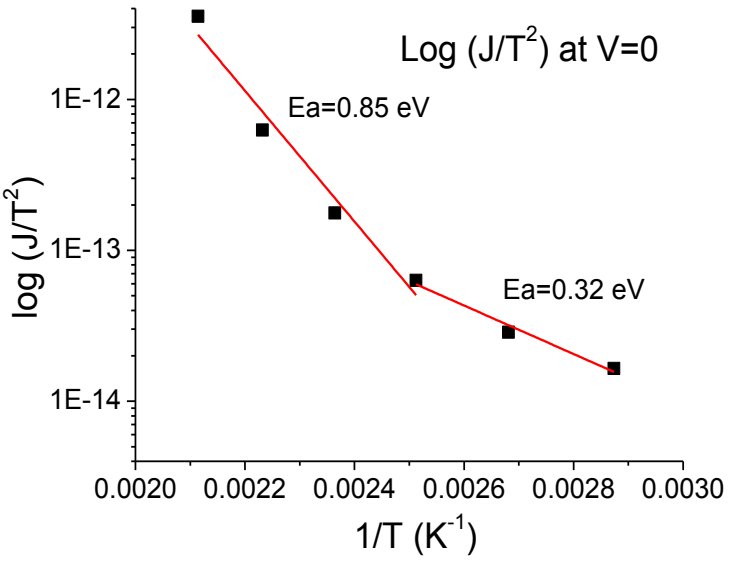

Figure 3-3 Schottky barrier height in 5 μm AF 45 glass capacitor determined from extrapolated leakage current. Symbols are the measurements and solid lines are fits to the data.

There is also modified Schottky conduction mechanism that accounts for electron scattering within the bulk of the insulator. Eqn. (3-1) is originally derived for a metal-vacuum interface where electronic mean free path is larger than distance between electrodes. However, if electronic mean free path in insulator is smaller than electrode spacing, Eqn. (3-1) is not strictly correct any more[28]. In that case the modified Schottky mechanism has been proposed[12, 28]. The current density for this mechanism can be described by

$$J = \alpha T^{\frac{3}{2}} E \mu \left(\frac{m^*}{m_0}\right)^{3/2} \exp\left(\frac{-\Phi_B}{k_B T}\right) \exp\left(\beta_s \sqrt{E}\right) \qquad (3\text{-}2)$$

where α is constant of $3\text{x}10^{-4}$ $As/cm^3K^{3/2}$, μ the electronic mobility in the insulator, m_0 the free-electron mass, m^* the effective mass. This is a combination of electrode-limited and bulk-limited conduction mechanism because the potential barrier and Schottky coefficient are electrode-

limited properties and mobility is a bulk property. This theory is successfully applied for the conduction mechanism of barium strontium titanate thin films[12]. From Eqn. (3-2) the log (J/E) vs $V^{1/2}$ should give a linear relationship for this conduction mechanism and is plotted in Figure 3-4. The permittivities can also be obtained from the slopes and are summarized in Table 3-2. They vary from 23 to 83 and are much higher even compared to the static permittivity. Therefore this modified Schottky conduction model is inadequate for interpreting leakage currents of 5 μm AF 45 glass capacitor.

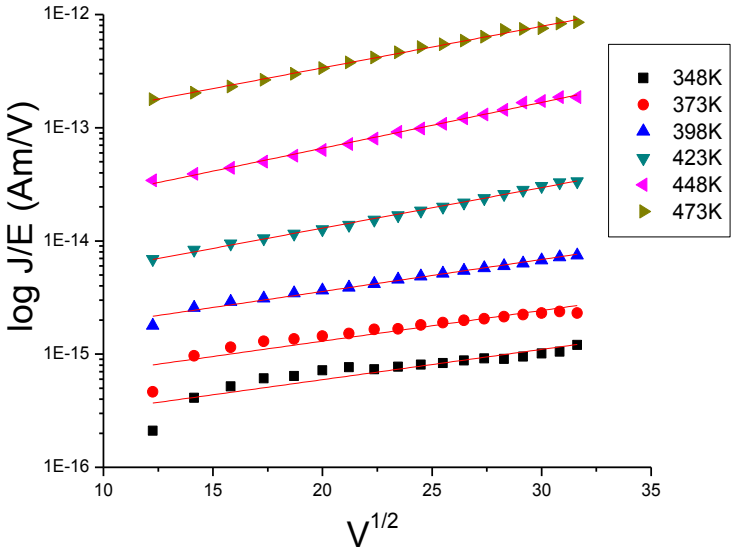

Figure 3-4 Dependence of steady-state current on the square root of applied voltage for 5 μm AF 45 glass capacitors. Symbols are the measurements and solid lines are fits to the data.

Table 3-2 Permittivities calculated from slopes in modified Schottky plots for 5 μm AF 45 glass capacitors.

Temperature (K)	slope	β_s	ε_r
348	0.027	0.000139	83
373	0.027	0.000139	72
398	0.028	0.000144	59
423	0.036	0.000185	32
448	0.040	0.000206	23
473	0.037	0.000191	24

3.4.2. Application of Fowler-Nordheim mechanism to electrical conduction for AF 45 glass

The Fowler-Nordheim conduction mechanism is a quantum-mechanical tunneling of electrons from a metal surface into a dielectric and the emission current can be described by

$$J = AE^2 \exp\left(-\frac{B}{E}\right) \qquad (3\text{-}3)$$

where A and B are constants for the Fowler-Nordheim mechanism. Eqn. (3-3) shows a linear relationship when log (J/V^2) is plotted against 1/V and the slope is negative. Figure 3-5 shows the plot for 5 μm AF 45 glass capacitors. There is no linear relationship with negative slope in Figure 3-5. Therefore the Fowler-Nordheim conduction mechanism cannot explain the leakage current in 5 μm AF 45 glass capacitors.

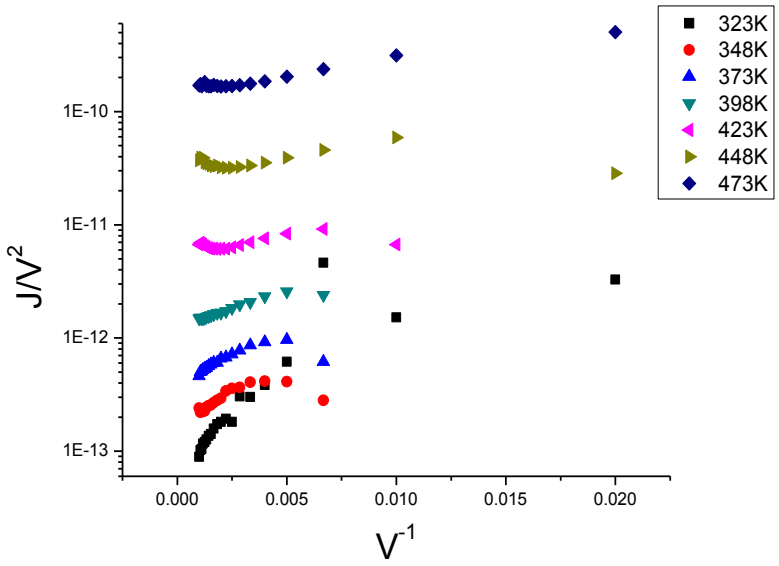

Figure 3-5 Dependence of steady-state current divided by the square of voltage on the inverse applied voltage for 5 μm AF 45 glass capacitors.

3.5. Application of bulk-limited conduction mechanism

Bulk-limited conduction mechanism can be divided into Poole-Frenkel mechanism, space-charge-limited current mechanism and hopping conduction mechanism. In the following section, each conduction mechanism will be discussed.

3.5.1. Application of Poole-Frenkel mechanism to electrical conduction for AF45 glass

In Poole-Frenkel mechanism electrons are injected from not metal electrode but bulk traps. This mechanism is sometimes called as the internal Schottky mechanism because two

mechanisms are similar except the origin of electrons. This Poole-Frenkel mechanism can be described by

$$J = J_0 \exp\left(-\frac{\Phi}{k_B T}\right) \exp\left(\frac{\beta_{PF}\sqrt{E}}{k_B T}\right) \quad (3\text{-}4)$$

where J_0 is the pre-exponential factor, Φ the potential barrier, β_{PF} the Poole-Frenkel coefficient. The Poole-Frenkel coefficient depends on the compensation in dielectric materials. If the dielectric is compensated, the Poole-Frenkel coefficient is given by

$$\beta_{PF} = \left(\frac{e^3}{\pi \varepsilon_r \varepsilon_0}\right)^{1/2} \quad (3\text{-}5).$$

So in the compensated case the slope in the Schottky plot is two times higher than that of Schottky mechanism. If the dielectric is uncompensated, the Poole-Frenkel coefficient is given by

$$\beta_{PF} = \left(\frac{e^3}{4\pi \varepsilon_r \varepsilon_0}\right)^{1/2} \quad (3\text{-}6).$$

In this case the slope is same with the slope in the Schottky plot. Figure 3-6 shows Poole-Frenkel plot for 5 μm AF 45 glass capacitors whose slopes will provide permittivities. Calculated permittivities by Eqns. (3-5) and (3-6) are summarized in Table 3-3. Permittivities calculated from compensated cases vary from 22 to 54. This is much higher than both the optical permittivity and the static permittivity. On the other hand, permittivities calculated from uncompensated case at temperatures between 423 and 473 K shows comparable values to the static permittivity. The higher permittivity below 398 K can't be explained by the Poole-Frenkel mechanism for uncompensated cases and more studies will be necessary to understand it.

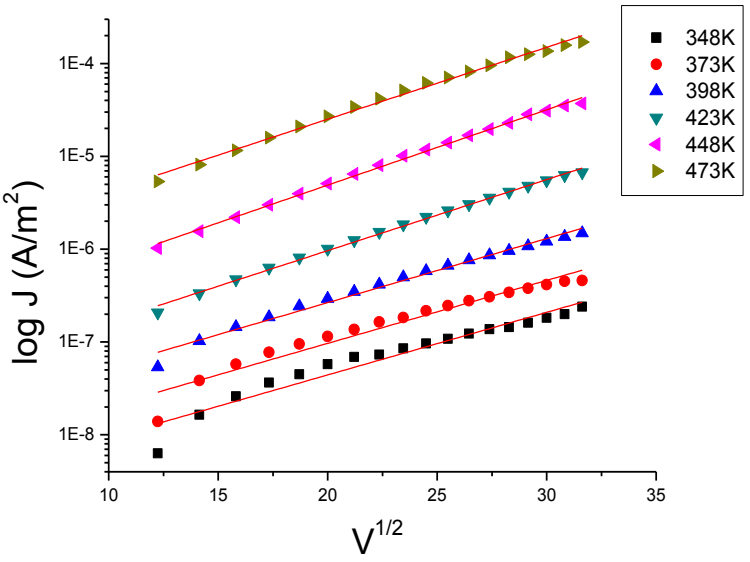

Figure 3-6 Poole-Frenkel plots for 5 μm AF 45 glass capacitors at different temperatures. Symbols are the measurements and solid lines are fits to the data.

Table 3-3 Permittivities calculated from slopes in Poole-Frenkel plots for 5 μm AF 45 glass capacitors.

Temperature (K)	slope	Permittivities for compensated case	Permittivities for uncompensated case
348	0.067	54	13
373	0.068	45	11
398	0.069	39	9.7
423	0.076	28	7.1
448	0.081	22	5.5
473	0.077	22	5.5

3.5.2. Application of space-charge-limited conduction mechanism to electrical conduction for AF45 glass

When one of above conduction mechanisms reaches a certain threshold level, such that the current is no longer limited by details of the electrode interface, the current becomes limited by the injected space charge in dielectric materials. For dielectric materials with defects, the current density in the space-charge-limited current (SCLC) model can be described by

$$J = \frac{9}{8}\mu\varepsilon_r\varepsilon_0\theta\frac{V^2}{L^3} \qquad (3\text{-}7)$$

where θ is the ration of free electron density to total electron density including trapped electron density, V the applied voltage, L the glass thickness. To determine this conduction mechanism, square relationship in Log J vs Log V and cubic relationship in Log J vs Log L should be confirmed. Figure 3-7 shows the voltage dependence of current density for 5 μm AF 45 glass capacitors. For temperatures below 398 K current density data can be fitted with one linear slope. These slopes are 1.7 which is smaller than theoretical slopes of 2 in space-charge-limited current models. For temperatures from 423 to 473 K there are two different slopes. In the lower voltage range slopes are between 1.4 and 1.6. In the higher voltage range slopes are between 2.0 and 2.1.

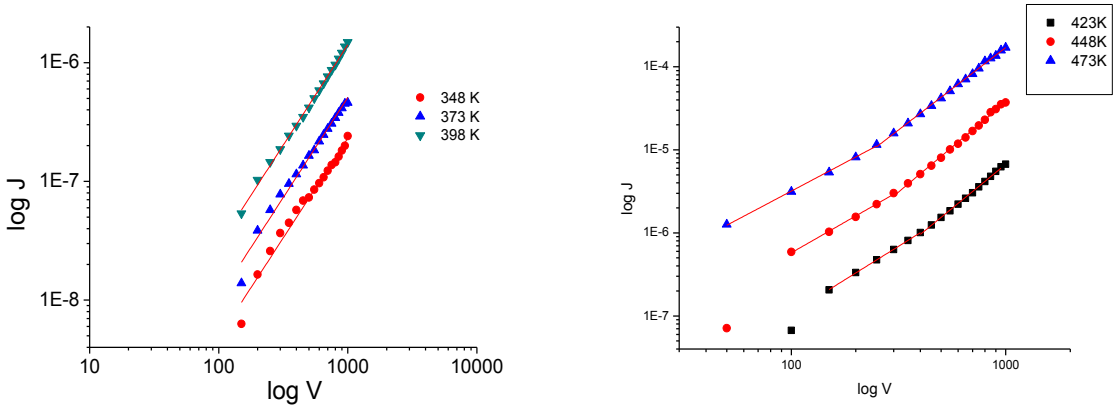

Figure 3-7 Voltage dependence of current density for 5 μm AF 45 glass capacitors at different temperatures in bilogarithmic scales.

These slopes are summarized in Table 3-4.

Figure 3-8 shows thickness dependence of current density for AF 45 glass at 473 K. In the voltage dependence of current density at 473 K there are two regimes (a region with slope of less than 2 and another region with slope of about 2). Therefore the thickness dependence is analyzed at two regions. In the high voltage region the slope in Log J vs Log L is 2.6 and close to the theoretical value of 3 in the space-charge-limited current model as shown in Figure 3-8(b). On the other hand, in the low voltage region the slope in Log J vs Log L is 1.9 and this is explainable neither ohmic law nor SCLC. It is interesting that if the mobility is field-dependent and proportional to the inverse square root of electric field, then the current density can be expressed by

Table 3-4 Slopes in voltage dependence of current density for 5 μm AF 45 glass capacitors at different temperatures in bilogarithmic scales.

Temperature (K)	Slope	
348	1.7	
373	1.7	
398	1.7	
423	1.6	2.1
448	1.5	2.2
473	1.4	2.0

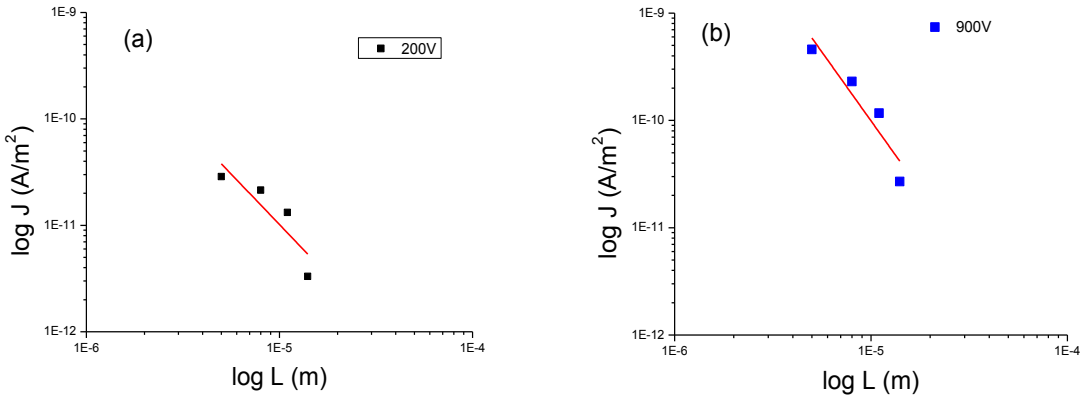

Figure 3-8 Thickness dependence of current density for AF 45 glass capacitor at 473 K in bilogarithmic scales; (a) low voltage current (200 V) (b) high voltage current (900 V).

$$J = \frac{2}{3}\left(\frac{5}{3}\right)^{3/2}\theta\varepsilon_r\varepsilon_0\mu_0 E_0^{1/2}\frac{V^{3/2}}{d^{5/2}}$$

$$\mu = \mu_0 E_0^{1/2} E^{-1/2} \qquad (3\text{-}8)$$

where μ_0 is the field independent mobility at the low field, E_0 the critical field beyond which the field dependence of the mobility is dominant[11]. Then the voltage dependence of current density will be 1.5 and the thickness dependence of current density will be 2.5. Their experimental data for $Bi_4Ti_3O_{12}$ thin films also show that the square relationship in the voltage dependence follows the slope of 1.5 since there is a strong injection of electrons above critical voltage. However, this analysis cannot explain the thickness dependence of 1.9 in the low voltage region.

The discrepancy between theoretical voltage dependence and experimental smaller voltage dependence could also be attributed to non-steady state ionic conduction. The depletion region is not fully developed in this case.

3.5.3. Application of ionic hopping conduction mechanism to electrical conduction for AF45 glass

As was mentioned previously, the current density is a strong function of electric field and temperature, suggesting that a thermally and field activated process is important component of conduction mechanism as well. Therefore the ionic hopping mechanism which is commonly observed in disordered materials is studied to determine the applicability to current density of AF 45 glass capacitors. The current density in the ionic hopping model can be expressed by

$$J = 2ne\lambda\nu \exp\left(-\frac{\Phi}{k_B T}\right)\sinh\left(\frac{\lambda eE}{2k_B T}\right) = J_0 \sinh\left(\frac{\lambda eE}{2k_B T}\right) \qquad (3\text{-}9)$$

where n is the carrier density, e the elementary charge, λ the hopping distance, ν the attempt to escape frequency, Φ the potential barrier between hopping sites. Figure 3-9 shows the current density as a function of electric field at different temperatures. The fitted lines to Eqn. (3-9) agree

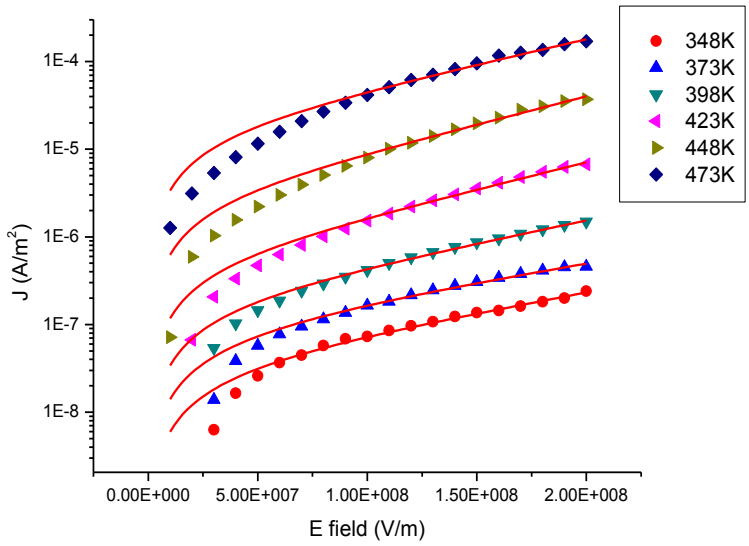

Figure 3-9 Current density for 5 μm AF 45 glass capacitors at different temperatures. Symbols are the measurements and solid lines are fits to the data using Eqn. (3-9).

Table 3-5 Hopping distances calculated from fitting current data to Eqn. (3-9).

Temperature (K)	Hopping distance (nm)
348	0.66
373	0.62
398	0.82
423	1.0
448	1.2
473	1.1

well with measured current data. Hopping distances are calculated from the equation and summarized in Table 3-5. At some measurement temperatures such as 373 and 473 K, the hopping distance did not fit the trend. However, there is an increasing trend in hopping distances with temperatures and values were in the range of 0.62 ~ 1.2 nm. These hopping distances have similar orders of magnitude to those (0.7 ~1.55 nm) reported by Vermeer et al. for various alkali-containing glasses[19]. Generally hopping conduction can be expected in glass containing alkali ions. AF 45 glass materials also have about 440 ppm of sodium ions which support the possibility for ionic hopping conduction. It is necessary to mention that doubly charged alkaline-earth cations and protons are also possible charge carriers. These three possible charge carriers are reported in alkali-free alumino-phosphate glasses[29, 30]. In AF 45 glass systems proton transfer can be occurred by hopping through a hydrogen bond to the next site and alkaline-earth cations are also possible charge carriers since there is a 24.1 wt% of BaO in the glass system. However, it is reported that in this glass system migrations of barium cations are most active at about 450 ^{o}C[31]. But our current measurement is performed up to temperature of 473 K and electric field of 200 MV/m and therefore there is less possibility of the motion of barium cations. On the other hand, during preparation of thin glass samples for current measurement they are etched in 2.5 vol% hydrofluoric acid solution at room temperature. Then hydrogen contamination in the glass surface can be removed during the etching process. So there is also less possibility of proton charge transfer during the current measurement.

To evaluate the activation energy, ln (J_0) versus 1/T was plotted in Figure 3-10 and the activation energy was calculated from Eqn. (3-9). The activation calculated from the plot was 0.65 eV which is somewhat lower that activation energy(0.82 ~ 0.9 eV) for sodium migration in this glass system[31]. This discrepancy in the activation energy can be attributed to the electric field by which sodium ions can be migrated. In this current measurement much higher electric

field (~200 MV/m) was used than the thermoelectric poling field (35 MV/m) in the reference. So higher electric field may lower the effective activation energy in this measurement.

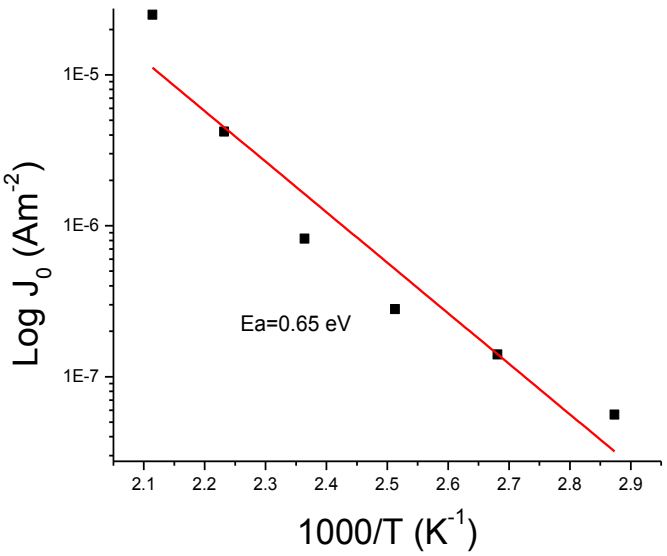

Figure 3-10 Log J_0 vs 1000/T plot to calculate activation energy for ionic hopping conduction mechanism of 5 μm AF45 glass capacitors.

3.6. Summary and conclusion

Several possible conduction mechanisms including both electrode-limited and bulk-limited mechanisms are applied to understand the leakage current of low-alkali boroaluminosilicate glass systems (AF 45). Schottky mechanism and Poole-Frenkel mechanism were successful to predict current density in this glass system at the highest measured temperatures (>423 K) where calculated permittivities were close to the static permittivity. Space-charge-limited conduction mechanism can be also applied to the leakage current data. The assumption of field-dependent mobility could explain the smaller voltage dependence of current density at lower temperature and less electric field regions. This discrepancy could also be attributed to non-steady state ionic conduction. The depletion region is not fully developed in this case. Lastly ionic hopping conduction mechanism is applied to the current measurement data. Hopping distances between 0.62 and 1.2 nm are calculated from the fitting and reasonable compared to other reported values. A sodium concentration of about 440 ppm also supports the possibility of ionic hopping conduction mechanism. Therefore it is hard to determine which specific conduction mechanism is valid for leakage current data at wide electric field and temperature range. It is more adequate to say that the conduction is governed by a combination of two or more conduction mechanisms. For example ion hopping conduction by sodium ion migration dominates the conduction at the initial stage and then space-charge-limited conduction starts to contribute from sodium ion depleted regions where electric field is enhanced.

3.7. References

1. Smith, N.J., et al., *Alkali-free glass as a high energy density dielectric material.* Materials Letters, 2009. **63**(15): p. 1245-1248.
2. Lee, H., et al., *Dielectric Breakdown of Thinned $BaO–Al_2O_3–B_2O_3–SiO_2$ Glass.* Journal of the American Ceramic Society, 2010. **93**(8): p. 2346-2351.

3. Murata, T., et al., *Electrode-Limited Dielectric Breakdown of Alkali Free Glass.* Journal of the American Ceramic Society, 2012.
4. Many, A., S. Weisz, and M. Simhony, *Space-charge-limited currents in iodine single crystals.* Physical Review, 1962. **126**(6): p. 1989.
5. Lampert, M.A., *Volume-controlled current injection in insulators.* Reports on Progress in Physics, 1964. **27**: p. 329.
6. Hartman, T., J. Blair, and R. Bauer, *Electrical conduction through SiO films.* Journal of Applied Physics, 1966. **37**(6): p. 2468-2474.
7. Servini, A. and A. Jonscher, *Electrical conduction in evaporated silicon oxide films.* Thin Solid Films, 1969. **3**(5): p. 341-365.
8. Jonscher, A., *Electronic properties of amorphous dielectric films.* Thin Solid Films, 1967. **1**(3): p. 213-234.
9. Stuart, M., *Electrode-Limited to Bulk-Limited Conduction in Silicon Oxide Films.* physica status solidi (b), 1967. **23**(2): p. 595-597.
10. Young, P.L., *dc electrical conduction in thin Ta_2O_5 films. I. Bulk-limited conduction.* Journal of Applied Physics, 1976. **47**(1): p. 235-241.
11. Joshi, P. and S. Desu, *Structural and electrical characteristics of rapid thermally processed ferroelectric BiTiO thin films prepared by metalorganic solution deposition technique.* Journal of Applied Physics, 1996. **80**: p. 2349.
12. Zafar, S., et al., *The electronic conduction mechanism in barium strontium titanate thin films.* Applied Physics Letters, 1998. **73**(24): p. 3533-3535.
13. Chutia, J. and K. Barua, *DC conduction phenomenon in polyvinylacetate films.* Journal of Physics D: Applied Physics, 1980. **13**: p. L9.
14. Ikezaki, K., T. Kaneko, and T. Sakakibara, *Effect of crystallinity on electrical conduction in polypropylene.* Jpn. J. Appl. Phys, 1981. **20**(3): p. 609.
15. Ieda, M., M. Nagao, and M. Hikita, *High-field conduction and breakdown in insulating polymers. Present situation and future prospects.* Dielectrics and Electrical Insulation, IEEE Transactions on, 1994. **1**(5): p. 934-945.
16. Ieda, M., *Electrical conduction and carrier traps in polymeric materials.* Electrical Insulation, IEEE Transactions on, 1984(3): p. 162-178.
17. Blom, P., et al., *Thickness scaling of the space-charge-limited current in poly (p-phenylene vinylene).* Applied Physics Letters, 2005. **86**(9): p. 092105-092105-3.
18. Teyssedre, G. and C. Laurent, *Charge transport modeling in insulating polymers: from molecular to macroscopic scale.* Dielectrics and Electrical Insulation, IEEE Transactions on, 2005. **12**(5): p. 857-875.
19. Vermeer, J., *The electrical conduction of glass at high field strengths.* Physica, 1956. **22**(6–12): p. 1257-1268.
20. Moridi, G., A. Nouruzi, and C. Hogarth, *Electrical properties of barium-borosilicate glasses.* Journal of Materials Science, 1991. **26**(23): p. 6271-6274.
21. Doi, A., *Ionic conduction and conduction polarization in oxide glass.* Journal of Materials Science, 1987. **22**(3): p. 761-769.
22. Scott, J.F., *Ferroelectric memories*. Vol. 3. 2000: Springer.
23. Mott, N., *Conduction in non-crystalline systems: VII. Non-ohmic behaviour and switching.* Philosophical Magazine, 1971. **24**(190): p. 911-934.
24. Kao, K. and W. Hwang, *Electronic Transport in Solids*. 1981, London: Pregamon.
25. Simmons, J.G., *Poole-Frenkel effect and Schottky effect in metal-insulator-metal systems.* Physical Review, 1967. **155**(3): p. 657.
26. Li, P. and T.-M. Lu, *Conduction mechanisms in $BaTiO_3$ thin films.* Physical Review B, 1991. **43**(17): p. 14261.

27. Nelson, R., *Electronic Conduction in Glass.* Journal of Applied Physics, 1963. **34**(3): p. 629-631.
28. Simmons, J.G., *Richardson-Schottky Effect in Solids.* Physical Review Letters, 1965. **15**(25): p. 967-968.
29. Trnovcova, V., E. Majkova, and E. Mariani, *Charge and mass transport in alkali-free aluminophosphate glasses; I, Electrical conductivity.* Physics and Chemistry of Glasses, 1977. **18**(4): p. 70-74.
30. Majkova, E., V. Trnovcova, and A. Bohun, *Charge and mass transport in" alkali free" aluminophosphate glasses: II, Diffusion of monovalent and bivalent cations.* Physics and Chemistry of Glasses, 1977. **18**(5): p. 83-86.
31. Dash, P., et al., *Activation energy for alkaline-earth ion transport in low alkali aluminoborosilicate glasses.* Applied Physics Letters, 2013. **102**: p. 082904.

Chapter 4: Modeling of cation depletion region in low-alkali boroaluminosilicate glasses under thermal poling

4.1. Introduction

The interest in thermal poling and cation depletion region of glass is related to both basic studies of glass conductivity and formation of spatial charge and such applications as anodic bonding, second optical harmonic generation, and electro-optical Pockels modulation[1-6]. In addition, creation of a high electric field region via cation depletion is a precursor to dielectric breakdown. It is commonly supposed that a strong electric field, related to negative spatial charge accumulation in the subsurface layer breaks central symmetry of the glass[3]. The thermal poling process can be defined by equilibrating a glass sample at modestly high temperature (200 – 500 ^{o}C), with subsequent application of a high voltage (1 – 6 kV) for a certain amount of time (5 – 60 min). During this time mobile ions within the glass network drift under the applied voltage, leading to the formation of a micron-scale cation depleted region beneath the anode. Upon cooling to room temperature with the applied voltage, the compositional change of ions in the glass is effectively quenched and results in a metastable internal electric field below the anode due to very low ionic mobility at the temperature.

Low-alkali boroaluminosilicate(BAS) glasses are interesting materials from the point of their finite sodium concentration that has a significant effect on electrical properties. Sodium concentrations range from 440 to 110 ppm-atom in barium boroaluminosilicate(Ba-BAS; Schott AF45) and calcium boroaluminosilicate(Ca-BAS; Nippon Electric Glass OA10G), respectively. These sodium concentrations of AF45 and OA10G are much lower than that of most commercial silicate glasses (Gorilla glass, E-glass having several atomic percent); however, the concentration

is still higher than that of commercial fused silica glasses by two orders of magnitude and the space charge developed from sodium movement results in electric field levels exceeding 10^8 V/m. There are many reports about thermal poling and second optical harmonic generation for silica and soda-lime glasses[2, 3, 5, 7-18]. Thermal poling and second optical harmonic generation of low-alkali BAS glasses have been recently reported by Smith et al[19] and the electric fields in the depletion regions were estimated through second order harmonic generation. In this chapter theoretical analysis and numerical modeling will be provided to better understand the thermal poling process and cation depleted region of low-alkali BAS glasses. Understanding of depletion region formation and the associated internal electric fields is essential in the development of a breakdown model for BAS glass.

4.2. Experimentally determined cation depletion width

The cation depletion width of low-alkali BAS glasses (AF45 and OA10G) by thermal poling has been explored by Smith et al., who determined the depletion width using second optical harmonic generation for 400 μm thick AF45 and 700 μm thick OA10G glasses [19]. Thermal poling was carried out in high vacuum ($0.5 – 3x10^{-6}$ Torr) to reduce the injection of H^+(or H_3O^+) from the atmosphere at the anode side. The temperature during poling ranged from 300 to 600 ^oC, and the poling time and applied voltage were 30 min and 4 kV, respectively. Press-contacted Pt electrodes were fabricated by sputter-depositing 100 nm of platinum onto thermally oxidized Si wafer substrates (1 μm thermal SiO_2) to form a stable Pt electrode without sputtering directly onto the glass. For the OA10G glasses, high-purity carbon foil was used as a non-blocking cathode. The resulting depletion widths are summarized in Table 4-1. Dash also reported the depletion widths for AF45 glasses with 50 μm thickness. These glasses were biased by the applied voltage of 700 - 2000 V at 500 - 550 ^oC for 60 - 120 min. In this case the poling

was performed in air atmosphere. The other difference was the Pt electrodes were deposited on both glass surfaces by sputtering. The depletion width was determined by second optical harmonic generation or impedance spectroscopy method. The resulting depletion widths are also summarized in Table 4-1. In the latter case the poling was also performed at 25 ^{o}C by the linearly increasing voltage of 10 V/s up to the half of dielectric breakdown strength. The depletion widths at the poling condition were summarized in Table 4-2. It is noteworthy that when the electric field is near the breakdown field at room temperature, there is a strong possibility of significant ionic migration during poling.

Table 4-1 Experimentally determined depletion widths for low-alkali BAS glasses using constant voltage; SHG(second optical harmonic generation), IS(impedance spectroscopy).

Material	Temperature	Atmosphere	Applied field	Time	Depletion width	Measurement	Ref
	^{o}C		MV/m	min	μm		
AF45	450	Vacuum	10	30	2.5	SHG	[19]
OA10G	400	Vacuum	5.7	30	5.9	SHG	[19]
AF45	500	Air	40	60	3.8	SHG	[20]
AF45	500	Air	20	60	2	SHG	[20]
AF45	550	Air	14	120	1.3	IS	[20]

Table 4-2 Experimentally determined depletion widths for AF45 glasses using linearly increasing voltage of 10 V/s; SHG(second optical harmonic generation).

Material	Temperature	Stop applied field	Time	Depletion width	Measurement techniques	Reference
	^{o}C	MV/m	min	μm		
AF45	25	440	37	6.8	SHG	[20]
AF45	25	400	33	6.4	SHG	[20]
AF45	25	300	25	4	SHG	[20]

4.3. The glass structure of low-alkali BAS glasses

In fused silica, the Si which is the network former is tetrahedrally coordinated to four oxygen ions forming $[SiO_4]^-$ tetrahedrons. The oxygen bonded to the Si (network former) is named as the bridging oxygen (BO). When an alkali oxide R_2O (where R can be Na, K, Li and so on) is introduced to the silicate glass network it breaks a Si-O bond and produces a non-bridging oxygen (NBO) which has a net negative charge as shown in Figure 4-1.Then the alkali ion compensates this negative charge on the NBO site. Therefore, addition of modifier oxides to a silicate glass is generally related to the formation of NBO sites.

In BAS glass systems such as AF45 and OA10G, SiO_2 and B_2O_3 are the glass network formers whereas Al_2O_3 plays as an intermediate compound between a network former and modifier. The basic building blocks of B and Al are triangularly coordinated to oxygen as shown

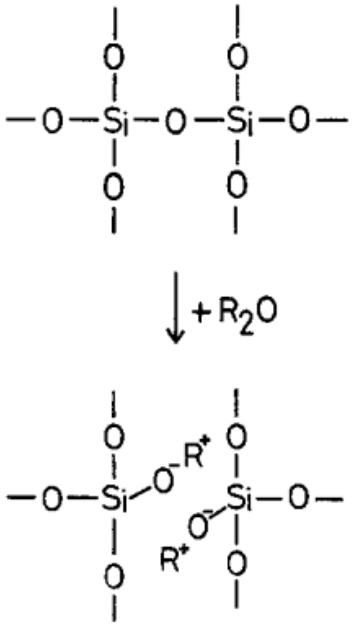

Figure 4-1 Formation of nonbridging oxygen ions by breaking some of Si-O-Si bonds when alkali (R_2O) is added to silica glass[21].

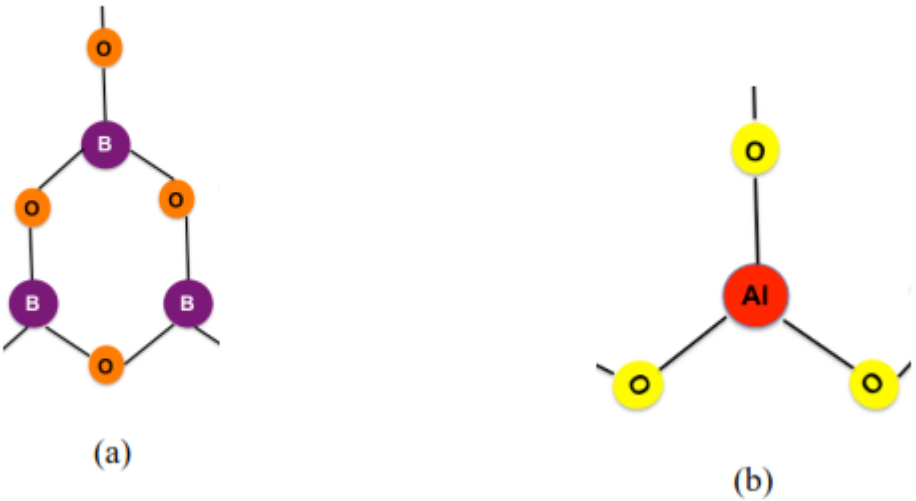

Figure 4-2 (a) Trigonal coordinated B exists as boroxol rings and (b) Trigonal coordinated Al in the glass network in the absence of modifier ions[20].

in Figure 4-2. Al_2O_3-B_2O_3-SiO_2 systems would rather prevail as a glass ceramic instead of forming a glass since the higher field strength of Si^{4+} and B^{3+} ions creates a deficiency of oxygen in the network of Al_2O_3-B_2O_3-SiO_2 system[22]. Consequently alkaline earth oxides with lower field strengths are added as modifiers to form BAS glasses. For instance if BaO is added to Al_2O_3-B_2O_3-SiO_2 system, Si holds its tetrahedral coordination. Meanwhile depending on the amount of added modifier Al and B can have a mixture of trigonal and tetrahedral coordination to oxygen where oxygen can be shared between $[AlO_4]^-$ and $[SiO_4]^-$[22, 23]. Since B^{3+} ions are relatively more stable than Al^{3+} ions, the modifiers preferentially associate with the Al ion by changing its coordination from Al^{3+} to Al^{4+}. Then B compensates the remaining modifiers by changing coordination from B^{3+} to B^{4+}.

In this chapter, two alkaline earth ion containing BAS glasses are studied. The compositions of these glasses are summarized in Table 4-3. The AF45 Ba-BAS glass has a molar ratio of 0.75 for Al_2O_3/BaO. Therefore, it can be assumed that the entire concentration of Al ions converts to tetrahedral coordination. Since Al is a trivalent ion, coordination with four oxygen ions leaves a negative charge on $[AlO_4]^-$, which is compensated by $1/2Ba^{2+}$. The remaining of the Ba^{2+} is compensated by $[BO_4]^-$ when B converts to tetrahedral coordination. It is suggested that ~75% of alkaline earth modifier cations are compensated at $[AlO_4]^-$ sites and ~25% at $[BO_4]^-$ sites in the AF45 glass[20, 23].

Table 4-3 Low-alkali BAS glass compositions used for this study[23].

Mole%	SiO_2	B_2O_3	Al_2O_3	MgO	CaO	SrO	BaO	As_2O_3	SnO_2	Na_2O
AF45	63.6	15.0	9.1			0.163	11.9	0.33	0.0007	0.074
OA10G	66.7	9.2	10.7	0.5	9.6	3.0	0.2		0.101	0.018

4.4. Ionic conduction of thermally poled low-alkali BAS glass

4.4.1. Na^+ motion in thermally poled low-alkali BAS glass

It is generally accepted that in these glasses the Na^+ ion is the most mobile charge carrier[14], and thus Na^+ ions will be the predominant charge carriers. In the current study, one expects that Na^+ ions will be swept away from the positive electrode resulting in Na depletion near that electrode and be the current conductor through the bulk of the glass. At the negative electrode, Na^+ is possibly reduced to metallic Na or Na compounds[5, 23]. In thermally poled borosilicate glass at 300 ^oC and 1.6 kV, an X-ray diffraction study demonstrated that sodium oxide and sodium aluminum oxide hydrate ($Na_2Al_2O_4 \cdot 6H_2O$) were developed near cathode side of the glass[5]. Smith also found that in thermally poled AF45 and OA10G glasses at 400 – 450 ^oC and 4 kV for 30 min Na_2O was detected near the cathode side from X-ray photoemission spectroscopy[19] as shown in Table 4-4. Electric fields for poling were 10 MV/m and 5.7 MV/m for AF45 and OA10G respectively. Once the Na^+ ions are swept away from near the anode, the current in that depleted region has to be carried some other charged species (i.e. protons, Ba or non-bridging oxygen).

Table 4-4 XPS surface composition(mol%) of BAS glasses poled at poling temperature for 4 kV and 30 min, compared to that of unpoled surface; T_p(poling temperature)[23].

Glass	Sample	SiO_2	B_2O_3	Al_2O_3	MgO	CaO	SrO	BaO	Na_2O
AF45	Unpoled surface	72.2	8.9	9.0				9.8	
T_p=450 ^oC	Poled anode	69.5	10.5	8.7				10.3	
	Poled cathode	65.2	9.3	9.4				12.1	3.9
OA10G	Unpoled surface	75.9	6.2	8.9	0.2	6.2	2.3	0.1	
T_p=450 ^oC	Poled anode	77.0	5.9	8.8	0.3	5.4	2.3	0.1	
	Poled cathode	75.2	5.9	8.9	0.7	5.6	2.3	0.1	1.3

4.4.2. Hydrogen ion motion in thermally poled low-alkali BAS glass

Several studies have reported the compositional changes of soda-lime glasses near the anode and as a function of thermal poling[14, 15]. Figure 4-3 shows the compositional profiles of thermally poled soda-lime glasses at 150 ^{o}C and 300 V (0.13 MV/m). This figure shows the presence of a thin layer of hydrogen immediately adjacent to the interface between the Na depleted glass and the bulk glass. The glass surface provides an H source prior to electrode deposition. Hydrogen is swept into the glass when the electric field is applied. However, since hydrogen is less mobile than the Na, it only moves in regions from which the Na has been depleted[24]. It is also generally observed that surfaces of all materials have proton site densities of 10^{16} cm^{-2} present on their surfaces, unless extraordinary efforts have been undertaken to clean the surface[25]. It should also be noted for Figure 4-3 that there is also hydrogen near the surface ,

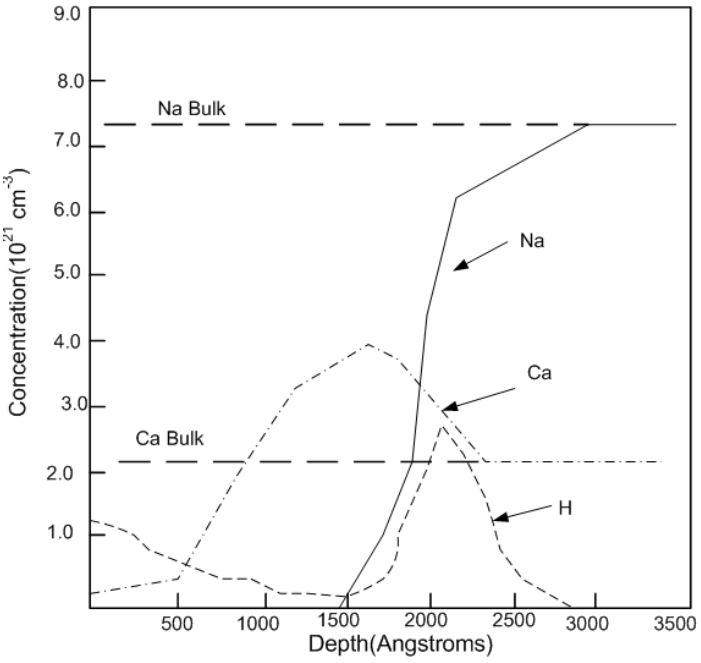

Figure 4-3 Compositional profiles of the Na, Ca, and H contents of poled soda-lime glass[14] The x-axis is the distance from the anode.

which is attributed to water in the atmosphere diffusing into the ion depleted glass after the electrodes have been removed. The hydrogen migration into thermally poled fused silica was also reported by secondary ion mass spectrometry[10].

Other researchers have also shown the presence of hydrogen in silicate glass. Ernsberger emphasized that hydrogen is diffused and transported into glass only as an oxygenated species such as molecular water or hydronium (H_3O^+), and not as a bare proton ion[26, 27]. Lanford et al. showed a three for one replacement of hydrogen atoms for Na atoms in soda-lime glass, implying that hydronium was the mobile species[24]. Nogami and Abe found that proton conduction in a 'wet' silica (sol-gel) glass is 'water-cooperative' with the conduction process described by protons hopping between hydroxyl and water molecules, and the activated state again being H_3O^+[28].

For low-alkali BAS glasses it is expected that there are hydrogen ions on the surface of glass. Their mobility could be slower than that of Na^+ ions, but it could be faster than that of other mobile ions such as Ba^{2+}(for AF45), Ca^{2+}(for OA10G), O^-. However, the existence of hydrogen ions is limited on the surface and then their concentration is much lower than the concentration charged species of Na^+, Ba^{2+}, Ca^{2+}, and O^-(or electron). Furthermore, the hydrogen injection at the anode depends on the type of electrode (deposited vs 'contact/pressed-on' electrodes). Contact electrodes allow for a continual supply of hydrogen ions, presumably from external surface moisture, whereas the deposited electrodes only allow movement of hydrogen already present at the surface[2]. It is also found that etching the surface of the glass prior to poling made a significant difference in the hydrogen profile concentration since it removed excess hydrogen already present at the surface[15]. Therefore its role in ionic charge transport could be less important when compared to the other ions.

4.4.3. Other mobile cations in thermally poled low-alkali BAS glass

The next most mobile ion present in soda-lime glass is the alkali-earth Ca^{2+} ion[14, 17]. As seen in Figure 4-3, the Ca moves from the surface region into the region depleted in Na^{+} ions. Since the Ca concentration in the region just below the Ca depleted layer is much more than that in the bulk of the glass, it seems that the Ca^{2+} ions can occupy the sites vacated by the Na^{+} ions[14]. Therefore in low-alkali BAS glass it is also expected that Ba^{2+} ion (for AF45) or the Ca^{2+} ion (for OA10G) is mobile.

4.4.4. Motion of O^{-} ions or electronic conduction in thermally poled low-alkali BAS glass

Once all the mobile modifier cations in the glass have been swept out of a region, the only possible charge carriers are negatively charged, either O^{-} ions or electrons[14, 18]. Based on the observation of oxygen evolution from the positive electrode, some authors have concluded that it is the O^{-} ions that move in the depletion layer near the anode[29]. However, other researchers have also concluded that negative space charge development is based on electronic conduction since resonant oxygen scattering measurement experiments demonstrated that no significant oxygen is transported from the glass into the Al metal electrode [14]. Therefore, it is still unclear which negatively charged species is dominant in depletion layer conduction. It is also expected that the type of charge carrier depends on the poling temperature and the applied voltage. O^{-} ions were reported as a charge carrier when poling was performed at high temperatures (300 to 500 ^{o}C) where ionic motion was possible. However, when the poling was performed at the temperature (100 to 150 ^{o}C), the electronic conduction is more probable. In any case negative charges transport should result in slowing down the drift of positive carriers and a corresponding increase in the poling depth due to weakened field screening from the negative charge

accumulation [30]. It is believed that the above situation is also applicable for the O^- ions or electronic conduction in low-alkali BAS glasses.

4.5. Consideration of mobility of Na^+ and other mobile ions in low-alkali BAS glass

4.5.1. Mobility of Na^+ ion in low-alkali BAS glass

Reported values for Na^+ mobility in different glasses, including fused silica, vary greatly. Stagg measured a sodium mobility of $5x10^{-11}$ $m^2V^{-1}s^{-1}$ in SiO_2 films at 250°C [31]. Schaeffer et al. found that the mobility of sodium ions was lowest for high OH-containing SiO_2[32]. Interpolating data gathered from Drury and Roberts leads to a value at 400 °C of approximately $3x10^{-15}$ $m^2V^{-1}s^{-1}$ for fused silica with 150 ppm OH (for Herasil) and $3x10^{-13}$ $m^2V^{-1}s^{-1}$ for fused silica with 10 ppm OH (for Infrasil)[33]. Schaeffer et al. explained a reduced sodium mobility at fused silica with higher OH concentration from the effect of immobilization of sodium ions in terms of an interaction between hydrogen and sodium ions[32]. This effect is similar to the "mixed-alkali effect" in alkali silicate glasses where the diffusivity of a specific alkali drastically decreases by adding another alkali. By examining the rise time of the SH signal, Myers calculated an effective sodium mobility in fused silica (for Optosil) of $\sim10^{-14}$ $m^2V^{-1}s^{-1}$ at 250 °C, assuming a space charge density of 10^{22} m^{-3}[3]. Shin and Tomozawa have reported extensive measurements of conductivities in fused silica[34]. Interpolating to 270 °C from their data for type II fused silica, and assuming a 1 ppm carrier concentration, gives a mobility of $\sim5x10^{-14}$ $m^2V^{-1}s^{-1}$, which agrees well with the mobility of Myers. The sodium mobility values in fused silica are summarized in Table 4-5 and the wide range of values could be due to variations in OH concentration.

For soda-lime glasses, a sodium mobility of $7x10^{-16}$ $m^2V^{-1}s^{-1}$ was reported at 150 °C assuming sodium concentration of $5x10^{27}$ m^{-3}[15]. Page et al. gave a mobility of $2x10^{-13}$ $m^2V^{-1}s^{-1}$ at 283 °C in soda-lime glass[35]. The sodium mobility in soda-lime glass depends on the mixed-alkali effect and therefore the relative concentration of alkali ions. These sodium mobilities are summarized in Table 4-5.

A sodium mobility in low-alkali BAS has not yet reported. Therefore it can be deduced from sodium mobility in the glass system using Einstein relationship. Tian et al. reported sodium tracer diffusion coefficients in alkaline-earth BAS glass[36]. The composition of this glass was 69.0 mol% SiO_2, 11.5 mol% Al_2O_3, 7.3 mol% B_2O_3, 5.0 mol% CaO, 4.4 mol% BaO, 1.4 mol% MgO, 1.2 mol% SrO and 0.2 mol% As_2O_5. This composition is similar to that of OA10G glass. This glass contained sodium as an impurity (~0.06 wt%). They concluded that below 664 ^oC, sodium diffusivity (D_{Na}^*) can be described by

$$D_{Na}^* = 10^{-2.21} \exp\left(-\frac{1.35}{k_B T}\right) cm^2 s^{-1} \quad (4\text{-}1).$$

Sodium mobility (μ_{Na}) can be obtained by the Einstein relation of

$$\mu_{Na} = \frac{D_{Na}^*}{k_B T} \quad (4\text{-}2).$$

The sodium mobility given by Eqn. (4-2) is also summarized in Table 4-5. The sodium mobility in alkaline-earth BAS shows a value of 8.3×10^{-16} $m^2V^{-1}s^{-1}$ at 400 ^oC which is three orders of magnitude lower than that of fused silica (Infrasil). Interestingly the lower sodium mobility cannot be related to a sodium concentration since a sodium concentration in alkaline-earth BAS (~600 ppm) is much higher than the concentration in Infrasil (~6 ppm). Therefore its lower mobility is very likely related to the presence of alkaline-earth ions in combination with the network formers Al and B[36].

Table 4-5 Sodium mobility in several types of glasses.

Glass	Temperature(^{o}C)	Na mobility($m^2V^{-1}s^{-1}$)	Reference
SiO_2 film	250	$5x10^{-11}$	[31]
Soda-lime	283	$2x10^{-13}$	[35]
Soda-lime	150	$7x10^{-16}$	[15]
Fused silica(Herasil)	400	$3x10^{-15}$	[32]
Fused silica(Infrasil)	400	$3x10^{-13}$	[32]
Fused silica(Optosil)	250	10^{-14}	[3]
Fused silica(type II)	270	$5x10^{-14}$	[34]
Alkaline earth BAS	400	$8.3x10^{-16}$	[36]
Alkaline earth BAS	450	$3.8x10^{-15}$	[36]
Alkaline earth BAS	500	$1.5x10^{-14}$	[36]
Alkaline earth BAS	550	$4.7x10^{-14}$	[36]

4.5.2. Mobility of hydrogen species in low-alkali BAS glass

Hydrogen mobility in a number of silicate glass systems has been reported by several authors. Hetherington et al. observed high temperature (800-1300 ^{o}C) electrolysis in fused silica and concluded that protons were injected through atmospheric moisture present at the glass surface before Pt electrode deposition[38]. The movement of hydrogen was found to be much slower than sodium. Hetherington et al. extrapolated available literature data and gave a mobility ratio of ~10^{-4} between hydrogen and sodium in fused silica[37]. At 250 ^{o}C Doremus predicted a hydrogen/sodium mobility ratio of $4x10^{-4}$ in silica glass[38]. Sodium and other ions present in silica as impurities are an important factor determining a mobility of hydrogen species. Sodium and other ions present in silica as impurities, which is in very low concentration. In this case the decomposition of atmospheric water vapors can produce the amount of hydrogen (hydronium) ions sufficient to compensate spatial charge arising due to electric field induced drop of the concentration of mobile ions in silica glass. Soda-lime glass contains several atomic percent of sodium and calcium where inflow of hydrogen species is insufficient to compensate the negative space charge[39]. Thus additional charge compensation and glass polarization mechanisms are possible from the less mobile ions such as Ba^{2+}, Ca^{2+}, O^{-} (electron). From the modeling point of view, effective mobility which is less than the measured mobility can be used if there is a deficit of hydrogen. This effective mobility depends on the boundary condition for H^{+} (H_3O^{+}) such as air humidity, surface properties, type of electrodes, etching and so on. It is worth to note that the measurement performed to evaluate mobility of hydronium in soda-lime glass were carried out with the glass immersed in water that correspond to unlimited source of hydronium[38]. Thus the use of hydrogen to sodium ions mobility ratio, one or two orders of magnitude less than one evaluated for the case of unlimited source of hydrogen can be reasonable. For example Petrov et al. assumed $2x10^{-20}$ $m^2V^{-1}s^{-1}$ of hydrogen mobility at 150 ^{o}C for soda-lime glass[30]. This

mobility agrees well with a value of $7x10^{-19}$ $m^2V^{-1}s^{-1}$ at 100 ^oC for soda-lime glass[40]. This hydrogen mobility is about nine orders of magnitude lower than that of proton-conduction oxide ($Ba(Zr_{0.9}Y_{0.1})O_{3-\delta}$, $3x10^{-11}$ $m^2V^{-1}s^{-1}$)[41]. It is also noteworthy that the coefficient of hydronium diffusion and hence its mobility strongly depends on its concentration[24].

4.5.3. Mobility of barium or calcium ions in low-alkali BAS glass

Barium or calcium mobility influences the formation of depletion region beneath the anode if the concentration of hydrogen species is not enough to compensate sodium depletion. This is the case when the poling is performed in the vacuum atmosphere or on vacuum deposited metals that are considered blocking electrodes. There are several reports on the diffusion of Ba^{2+} or Ca^{2+} in silicate glasses[42-44]. These diffusivities are converted into the mobility of corresponding ions using Eqn. (4-2) at temperatures between 400 and 550 ^oC which are summarized in Table 4-6 and 4-7. At these temperatures the mobility of Ba^{2+} ion for $0.1Na_2O$-$2.9BaO$-$4SiO_2$ and $3BaO$-$4SiO_2$ ranged from $1.5x10^{-22}$ and $2.6x10^{-20}$ $m^2V^{-1}s^{-1}$. The barium mobility in $0.1Na_2O$-$2.9BaO$-$4SiO_2$ is about two times higher than the mobility in $3BaO$-$4SiO_2$. This might be due to higher sodium mobility. For the mobility of Ca^{2+} ion the mobility in $0.1Na_2O$-$2.9CaO$-$4SiO_2$ was one order of magnitude of higher than that of $3CaO$-$4SiO_2$ at the same temperature. The Ca^{2+} mobility in $0.1Na_2O$-$2.9CaO$-$4SiO_2$ ranged from $3.1x10^{-22}$ to $1.4x10^{-19}$ $m^2V^{-1}s^{-1}$. On the other hand the Ca^{2+} mobility in $3CaO$-$4SiO_2$ ranged from $6.5x10^{-23}$ and $2.5x10^{-20}$ $m^2V^{-1}s^{-1}$.

Petrov et al. used a calcium mobility of $2x10^{-21}$ $m^2V^{-1}s^{-1}$ at poling condition of 150 ^oC and 1.7 kV for 1.2 mm thick soda-lime glass to model concentration distribution of mobile ions[30]. This is much higher mobility than the mobility calculated from the diffusivity. It is rationalized from the fact that there is a discrepancy in the width of interface regions evaluated for poled glass

on the base of diffusion coefficients and experimental data. The measured width of the interface regions always exceeds theoretical predictions by several nanometers for soda-lime glass[30]. This much higher mobility might come from electric field induced lowering of potential barrier. It has been known that in ionic conduction high electric field lowers the potential barrier in the direction of the field. These calcium and barium mobilities will be used to simulate the depletion region under thermal poling for low-alkali BAS in the later chapter.

Table 4-6 Mobility of Ba^{2+} ion in two kinds of silicate glasses converted from diffusivities[43, 44].

Temperature	Ba^{2+} mobility in $0.1Na_2O$-2.9BaO-4SiO_2	Ba^{2+} mobility in 3BaO-4SiO_2
^oC	$m^2V^{-1}s^{-1}$	$m^2V^{-1}s^{-1}$
400	$1.5x10^{-22}$	$1.6x10^{-22}$
450	$1.1x10^{-21}$	$7.9x10^{-22}$
500	$5.9x10^{-21}$	$3.3x10^{-21}$
550	$2.6x10^{-20}$	$1.1x10^{-20}$

Table 4-7 Mobility of Ca^{2+} ion in two kinds of silicate glasses converted from diffusivities[42, 44].

Temperature	Ca^{2+} mobility in $0.1Na_2O$-2.9CaO-4SiO_2	Ca^{2+} mobility in 3CaO-4SiO_2
^oC	$m^2V^{-1}s^{-1}$	$m^2V^{-1}s^{-1}$
400	$3.1x10^{-22}$	$6.5x10^{-23}$
450	$3.1x10^{-21}$	$6.3x10^{-22}$
500	$2.3x10^{-20}$	$4.5x10^{-21}$
550	$1.4x10^{-19}$	$2.5x10^{-20}$

Experimentally, researchers have found that several mobile ions in glass are transported under electric field. Sodium has been found to have the highest mobility in all glass systems (fused silica, soda lime and low-alkali BAS). Hydrogen in the form of protons or hydronium ions may also play a role in the total ionic current and space charge development by initiating from the glass surface. Alkaline earth (Ba^{2+}, Ca^{2+}) ions and NBOs have the lowest mobilities and their

contributions become important at high temperature and high electric fields. It is important to develop a model that incorporates all of these ionic contributions to the space charge formation, conduction, and depletion layer formation in glass as a function of electric field, temperature and time.

4.6. Analytical method to determine the depletion width for thermally poled low-alkali BAS

4.6.1. Single charge carrier model for the depletion width

Single charge carrier model derived by von Hippel from work on alkali halides is typically used as a starting point for models of thermal poling of glass[45]. This model is originally proposed to explain poling behavior of silica by Myers et al. and has successfully predict the depletion width of glass with low sodium concentration[3, 46]. According to the model, a positive charge carrier (Na^+) can leave and be accepted at the cathode (nonblocking cathode) but cannot reenter from the anode(blocking anode). The steady state will leave two distinct regions which consist of a negative space charge region (Na^+ depleted region) on the anode and the neutralized region for the rest of the sample as shown in Figure 4-4. The built-in electric field as a function of distance (z) during the poling can be obtained by Poisson equation and be described by

$$E(z) = \frac{en(z-z_a)}{\varepsilon} \text{ for } 0 < z < z_a \qquad (4\text{-}3)$$

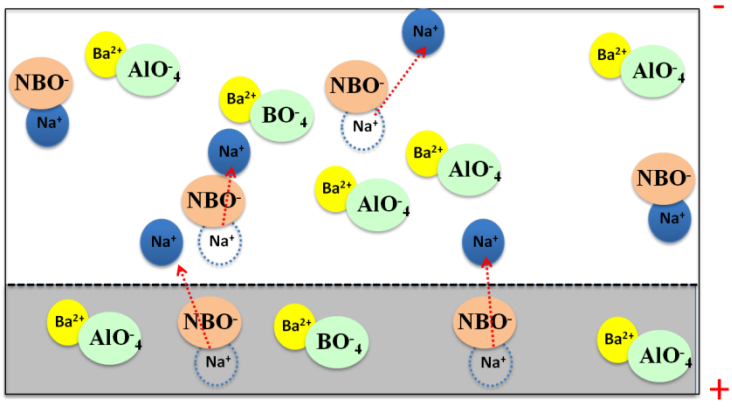

Figure 4-4 Space-charge region in low-alkali BAS based on single charge carrier model assuming only Na^+ motion. Shaded area represents a space-charge region.

where n is the negative ion concentration in the glass, e the elementary charge, z_a the depletion width, ε the permittivity. The depletion width (z_a) can be obtained by applied voltage and given by

$$z_a = \sqrt{\frac{2\varepsilon V_{app}}{en}} \quad (4\text{-}4).$$

The maximum electric field is located at the anode and described by

$$E_{max} = \sqrt{\frac{2enV_{app}}{\varepsilon}} \quad (4\text{-}5).$$

Assumption of neutrality in the glass provides the negative ion concentration (n) is equal to the positive ion concentration. Then Eqn. (4-5) suggests that as sodium concentration increases the maximum electric field at the anode also increases. However, this maximum electric field will be limited by the intrinsic breakdown strength of glass. After the poling the applied voltage is removed and then the field distribution can be expressed by

$$E(z) = \frac{en(z - z_a)}{\varepsilon} - \frac{V_{app}}{L} \text{ for } 0 < z < z_a$$

$$= -\frac{V_{app}}{L} \text{ for } z > z_a \quad (4\text{-}6).$$

This is given by the boundary condition that the applied voltage will be zero after poling. This electric field distribution during and after poling is compared in Figure 4-5. Lastly a characteristic time (τ) for the formation of space charge region can be described by

$$\tau = \frac{L}{\mu}\sqrt{\frac{\varepsilon}{2neV_{app}}} \quad (4\text{-}7)$$

where L is the sample thickness, μ the mobility of sodium at given temperature.

This single charge carrier model can be applied to AF45 and OA10G glass as shown in Table 4-8. Depletion widths from single charge carrier model under the poling condition of 4 kV are 0.53 and 0.98 μm for AF45 and OA10G, respectively. These are about five or six times smaller than experimental depletion widths. On the other hand the maximum electric field at the

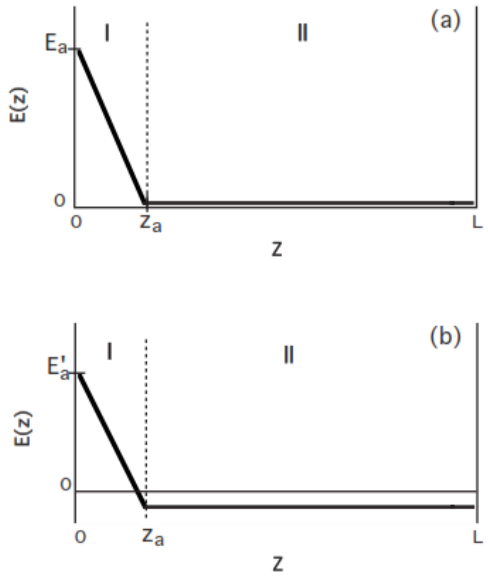

Figure 4-5 Electric field distribution (a) during and (b) after thermal poling according to the single charge carrier model[46].

anode is well above the intrinsic breakdown strength (~1.2×10^9 V/m) for both glass types[47, 48]. Therefore it is expected that additional mobile ions such as H_3O^+, O^- or Ba^{2+} (Ca^{2+}) contribute the charge compensation as shown in Figure 4-6. Multiple charge carriers during thermal poling will result in decrease of the maximum electric field and increase of the depletion width by Poisson's equation due to charge compensation in depletion region. The characteristic time for space charge region formation from sodium depletion also support this idea. From Eqn. (4-7), the time showed 265 and 285 seconds for given poling conditions. If this single charge carrier model is possible in the initial stage of thermal poling, after this characteristic time mobile ions other than Na^+ can compensate the space charge in the depletion region.

Table 4-8 Depletion widths and maximum electric field of AF45 and OA10G glasses according to the single charge carrier model.

	AF45	OA10G
Thickness (μm)	400	700
Applied voltage (V)	4000	4000
Poling temperature (^{o}C)	450	400
Na concentration (ppm)	440	110
Sodium concentration (atoms/m^{3})	9.41x10^{24}	2.45x10^{24}
Relative permittivity	6.0	5.3
Depletion width (μm)	0.53	0.98
Experimental depletion width (μm)	2.5	5.9
Maximum electric field (x10^{9} V/m)	15.1	8.2
Characteristic time for space charge formation (s)	265	285

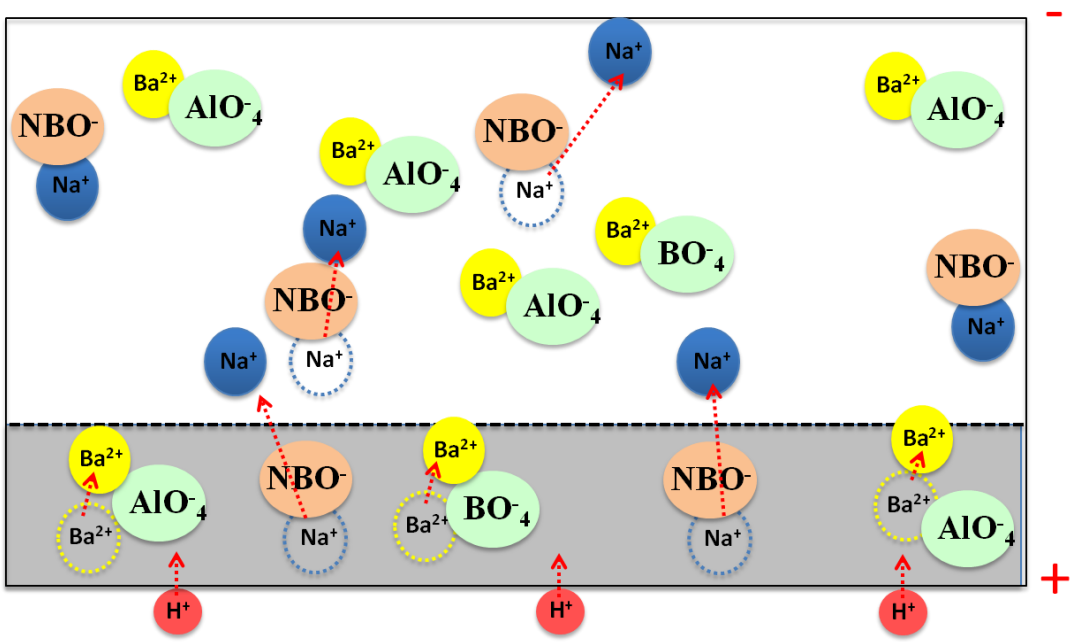

Figure 4-6 Space-charge region in low-alkali BAS based on multiple charge carrier model assuming motion of Na^{+}, Ba^{2+}, and H^{+}. Shaded area represents a space-charge region.

4.6.2. Two charge carrier model for the depletion width

Two charge carrier models for thermal poling were proposed by several authors where they assume nonblocking condition at both electrodes[18, 29, 40, 49, 50]. Carlson et al. assumed nonbridging oxygens move toward the anode and decrease the negative space charge in the sodium depletion region. This case is often reported for thermal poling at Ar and vacuum atmosphere or metalized samples. The authors proposed that it might be possible for nonbridging oxygens to break bonds with the silica network and move toward the anode in the form of O^- where they are neutralized and produce oxygen molecules. Therefore as the sodium ions move toward the cathode, they induce nonbridging oxygen movement toward the anode. In this case the depletion width (z_a) can be calculated from the total charge transport through an external circuit,

$$z_a \approx \frac{\int_0^t i dt}{peA} \tag{4-8}$$

where i is the external current over time t, p the concentration of mobile sodium ions, and A the electrode area. The electric field across the depletion region is approximately constant and given by

$$E_{max} \approx \frac{(\varepsilon+2)V_{app}}{3z_a} \tag{4-9}.$$

So the current evolution during thermal poling is necessary to calculate the depletion width and maximum electric field.

Another two charge carrier model assumes proton injection at the anode for charge compensation process. This is often reported for thermal poling in air atmosphere or pressed contact electrodes. The theoretical model is developed by Prieto et al. to analyze an ion exchange process assisted by a DC electric field for optical waveguide fabrication[50]. By assuming almost complete replacement of Na^+ by H_3O^+/H^+ ions, and neglecting the drift of other mobile ions like barium, calcium or oxygen, the sodium depletion layer thickness can be described by

$$z_a(t) = \left(\frac{1}{\alpha N_H} - 1\right)\left[\sqrt{\frac{2\alpha N_H \mu_H V}{(1-\alpha N_H)^2}t + L^2} - L\right]$$

$$\alpha = 1 - \frac{\mu_H}{\mu_{Na}} \qquad (4\text{-}10)$$

where L is the glass thickness, μ_H the proton mobility, μ_{Na} the sodium mobility, N_H the ratio of proton concentration to the intrinsic sodium ion concentration, t the poling time, V the applied voltage. N_H is 1 since it is assumed that the sodium ions in the depletion layer were exchanged completely to the protons. On the other hand, the electric field across the sodium depletion layer can be expressed by

$$E_{max}(t) = \frac{V}{(1-\alpha)\sqrt{\frac{2\alpha\mu_H V}{(1-\alpha)^2}t + L^2}} \qquad (4\text{-}11).$$

This two charge carrier model is applied to low-alkali BAS using Eqn. (4-10) and (4-11). Then the depletion widths and maximum electric field can be determined such as Table 4-9. The sodium mobility for the glasses at given temperature are determined to provide the closest depletion width to experimental ones. The sodium mobility for AF45 and OA10G were 1.0×10^{-16} and 3.0×10^{-16} $m^2V^{-1}s^{-1}$ respectively. Compared to Table 4-5 this sodium mobility is within reasonable range. The ratio of proton mobility to sodium mobility is fixed to 10^{-2}, which was reported as of the order of $10^{-2} \sim 10^{-3}$ for the case of soda-lime glass[2, 18, 30, 40]. Interestingly the maximum electric field within depletion layer decreased compared to the single charge carrier model and similar to the breakdown strength of low-alkali BAS.

Two charge carrier model provides much realistic depletion width and electric field in the layer. This model can also explain thickness and poling time dependence of depletion width. However, this model does not include the effect of different sodium concentration and other possible mobile ions such as barium, and NBO.

Table 4-9 Depletion widths and maximum electric field of AF45 and OA10G glasses according to the two charge carrier model proposed by Prieto et al.

	AF45	OA10G
Thickness (μm)	400	700
Applied voltage (V)	4000	4000
Poling temperature (^{o}C)	450	400
$\mu_{Na}(m^2V^{-1}s^{-1})$	$1.0x10^{-16}$	$3.0x10^{-16}$
μ_H/μ_{Na}	10^{-2}	10^{-2}
N_H	1	1
Relative permittivity	6.0	5.3
Depletion width (μm)	1.5	2.6
Experimental depletion width (μm)	2.5	5.9
Maximum electric field ($x10^9$ V/m)	0.73	0.42

4.7. Numerical method to determine the depletion width for thermally poled low-alkali BAS

4.7.1. Numerical method based on Proctor and Sutton model

Proctor and Sutton proposed a space charge development model in silica glass based on a charge recombination and dissociation mechanism[51]. Quiquempois et al. also used this model analytically to explain charge migration and a second-order nonlinearity during thermal poling in silica glasses[52]. There are several assumptions for this model to apply low-alkali BAS.

(1) It is assumed that a BAS sample is located at x=0 and x=d and the problem is one dimensional.

(2) Two kinds of charge carriers are present in the glass. A sodium ion of concentration of p is assumed to be mobile. Meanwhile, a NBO ion of concentration n is assumed to be immobile.

(3) Blocking electrode condition is present at the anode and cathode. So charge carriers cannot be neutralized at the electrode or penetrate through it. Injection of hydrogen species through the electrode is also assumed to be negligible.

(4) Sodium ions can move under the applied electric field (E). Then the current density(j) can be given by

$$j = \mu epE \tag{4-12}$$

where μ is the mobility of sodium ion, e the elementary charge, p the mobile sodium ion concentration. Current density from diffusion is ignored in this equation.

(5) The sodium ion and NBO ion can be recombined together or dissociated.

The electric field distribution and charge distribution in low-alkali BAS during thermal poling can be described by Eqn. (4-12), the local equation of continuity, and Poisson's equation below.

$$\frac{\partial p}{\partial t} = -\mu_{Na}\frac{\partial (Ep)}{\partial x} + q - a \quad (4\text{-}13)$$

$$\frac{\partial n}{\partial t} = -\mu_{NBO}\frac{\partial (En)}{\partial x} + q - a \quad (4\text{-}14)$$

$$\frac{\partial E}{\partial x} = \frac{e}{\varepsilon}(p - n) \quad (4\text{-}15)$$

where μ_{Na} is the mobility of sodium, μ_{NBO} the mobility of nonbridging oxygen, q the number of dissociated ions per volume per time, 'a' the number of recombined ions per volume per time. Proctor et al. assumed that 'a' is proportional to the number of positive uncombined charges times the number of negative uncombined charges. In the case of q it is proportional to the number of combined negative charges[51]. Thus the recombination rate per volume (a) and the dissociation rate per volume (q) can be calculated by

$$a = \alpha np \quad (4\text{-}16)$$

$$q = \kappa(c\text{-}n) \quad (4\text{-}17)$$

where α is the recombination coefficients, κ the dissociation coefficients, and c the total concentration of positive charge carriers within glass (dissociated and recombined). A dimensionless parameter called R is also introduced by Proctor et al. which is proportional to the ratio of the recombination coefficient to the dissociation coefficient. R can be described by

$$R = \frac{\alpha c}{\kappa} \quad (4\text{-}18).$$

Initially it is assumed that there are no dissociated ions. Using equations from Eqn. (4-12) to Eqn. (4-17) the electric field and the space charge distribution can be obtained. Finite difference method is used for the numerical modeling (see chapter 5.4).

Applying this model to low-alkali BAS with given parameters of sodium mobility, NBO mobility, dissociation coefficient, and R that are summarized in Table 4-10. The sodium mobilities are chosen based on values in Table 4-5 and adjusted to provide similar depletion width to experimental results. These sodium mobilities depend on the glass composition

Table 4-10 Modeling parameters based on Proctor model for low-alkali BAS.

	AF45	OA10G
Thickness (μm)	400	700
Applied voltage (V)	4000	4000
Poling temperature (^{o}C)	450	400
Sodium concentration (atoms/m^3)	$9.41x10^{24}$	$2.45x10^{24}$
Sodium mobility ($m^2V^{-1}s^{-1}$)	$3.0x10^{-16}$	$9.0x10^{-16}$
NBO mobility ($m^2V^{-1}s^{-1}$)	$6.0x10^{-20}$	$1.8x10^{-19}$
Dissociation coefficient(m^3s^{-1})	$5.6x10^{-6}$	$4.0x10^{-6}$
R (atoms/m^3)	$9.9x10^3$	$2.0x10^4$

and the concentration of OH. So they are assumed to be $3.0x10^{-16}$ and $9.0x10^{-16}$ $m^2V^{-1}s^{-1}$ respectively. The NBO mobilities are assumed to be $2x10^{-4}$ times of the sodium mobilities which mean NBOs are relatively immobile. This mobility ratio between sodium ion and NBO is also used in thermal poling of 1 mm thick soda-lime glass at 210 ^{o}C and 1.5 kV[18].

The dissociation coefficient can be estimated from the dissociated sodium ion concentration at equilibrium. From a microscopic point of view, it has been proposed that alkali transport in alkali silicate glasses occurs by interstitial cationic pairs, formed by two alkali cations sharing the same negatively charged NBO, which is an entity equivalent to a Frenkel defect for an ionic crystal or to a dissociated cation for electrolytic solutions[53]. The formation of interstitial cationic pairs would result from the dissociation of an alkali cation from its normal site, allowing it to jump to a neighboring cationic site that is already occupied as shown in Figure 4-7. Since the required energy to escape from a normal position is expected to be much higher than the mean thermal energy (k_BT), the concentration of such positively charged defects (p_+) is very low compared to the total concentration of alkali cations (p). The chemical equilibrium

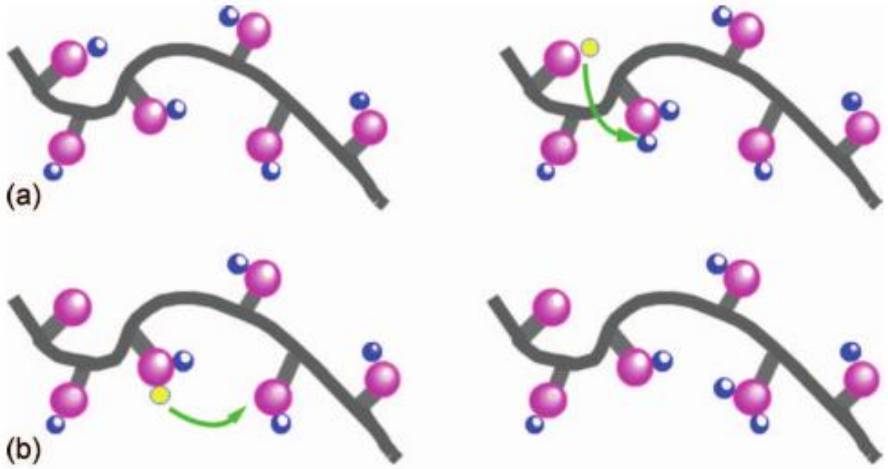

Figure 4-7 Schematic representation of conduction mechanisms in alkali silicate glasses; (a) Formation of an interstitial pair, (b) Interstitial pair migration following an activation mechanism[53].

between alkali cations in regular sites and in interstitial positions leads to the following relationship

$$p_+ = p\exp(-\frac{\Delta G_f}{2k_BT}) \tag{4-19}$$

where $\Delta G_f=\Delta H_f-T\Delta S_f$ is the free energy associated with the formation of an interstitial pair and a cationic vacancy. ΔH_f and ΔS_f are their formation enthalpy and entropy, respectively. The positively charged interstitial cationic pair could then migrate from one interstitial position to another when an electric field is applied. In case of a thermally activated mechanism, the cationic conductivity can be expressed by

$$\sigma = p\frac{e^2\lambda^2\nu}{6k_BT}\exp\left(-\frac{\frac{\Delta G_f}{2}+\Delta G_m}{k_BT}\right) = \sigma_0\exp\left(-\frac{\frac{\Delta H_f}{2}+\Delta H_m}{k_BT}\right) \tag{4-20}$$

where λ is the jump distance, ν the characteristic attempt frequency, ΔG_m the free energy for migration, σ_0 the pre-exponential factor, ΔH_m the migration enthalpy. Compared to the Arrhenius law, an experimentally determined activation energy (E_a) can be related to

$$E_a = \frac{\Delta H_f}{2} + \Delta H_m \quad (4\text{-}21).$$

If it is further assumed that the entropic terms are very low compared to k_B, the free energies ΔG_f and ΔG_m can be reduced to the enthalpies ΔH_f and ΔH_m. Thus Eqn. (4-19) can be rewritten by

$$p_+ = p\exp(-\frac{\Delta H_f}{2k_B T}) \quad (4\text{-}22).$$

Thus the concentration of dissociated alkali ions can be estimated from Eqn. (4-22) if the formation enthalpy is known. Eqn. (4-21) shows that the formation enthalpy can be estimated from the experimental activation energy and the migration enthalpy. Souquet et al. also showed the migration enthalpy is smaller than the formation enthalpy and is constant for Li^+, Na^+, and K^+ in alkali silicate glasses(~0.17 eV)[53]. This conduction mechanism is applied to the low-alkali BAS to determine its concentration of dissociated sodium ion and the dissociation coefficient. For this purpose the migration enthalpy of sodium in the low-alkali BAS is assumed to be 0.53 eV which is reasonable based on that of alkali silicate glasses. Dash et al. showed that the activation of sodium in this glass is 0.82 eV from analysis of thermally stimulated depolarization current[54]. Then the Eqn. (4-21) provides the formation enthalpy of 0.57 eV. Finally the Eqn. (4-22) gives the dissociated sodium concentration of 9.41×10^{22} and 1.74×10^{22} #/m^3 for AF45 and OA10G respectively at given temperature. The dissociation coefficient (κ) is obtained from Eqn. (4-17) with the ratio of dissociated sodium concentration to the total sodium concentration, which is 5.6×10^{-6} and 4.0×10^{-6}.

The last necessary parameter is R and at the steady state this can be calculated from $R = c(c - n)/pn$[52]. R for Infrasil was found to be approximately equal to 2×10^4[51, 52]. In low-alkali BAS calculated Rs were 9.9×10^3 and 2.0×10^4 for AF45 and OA10G respectively.

Figure 4-8 shows modeling results for thermal poling of 400 μm AF45 glass at 450 ^oC and 4 kV during 30 min. It is shown that the electric field near the anode(x=400 μm) increases during thermal poling which is much higher the applied field (10 MV/m). It is noteworthy that the

electric field at the anode after 1800 s approaches the dielectric breakdown strengths for 50 μm AF45 glasses[55]. Figure 4-8(c) and (d) show that during thermal poling sodium ions move toward the cathode (x=0) and NBOs move toward the anode (x=400 μm). Although much smaller NBO mobility ($\mu_{NBO}/\mu_{Na}=2x10^{-4}$) than sodium ion mobility is used, the NBO migration cannot be excluded due to high electric field near the anode. Figure 4-8(b) shows that negative space charge develops under the anode due to the depletion of sodium ion and this space charge results in the electric field enhancement as shown in Figure 4-8(a).The depletion width under the anode for

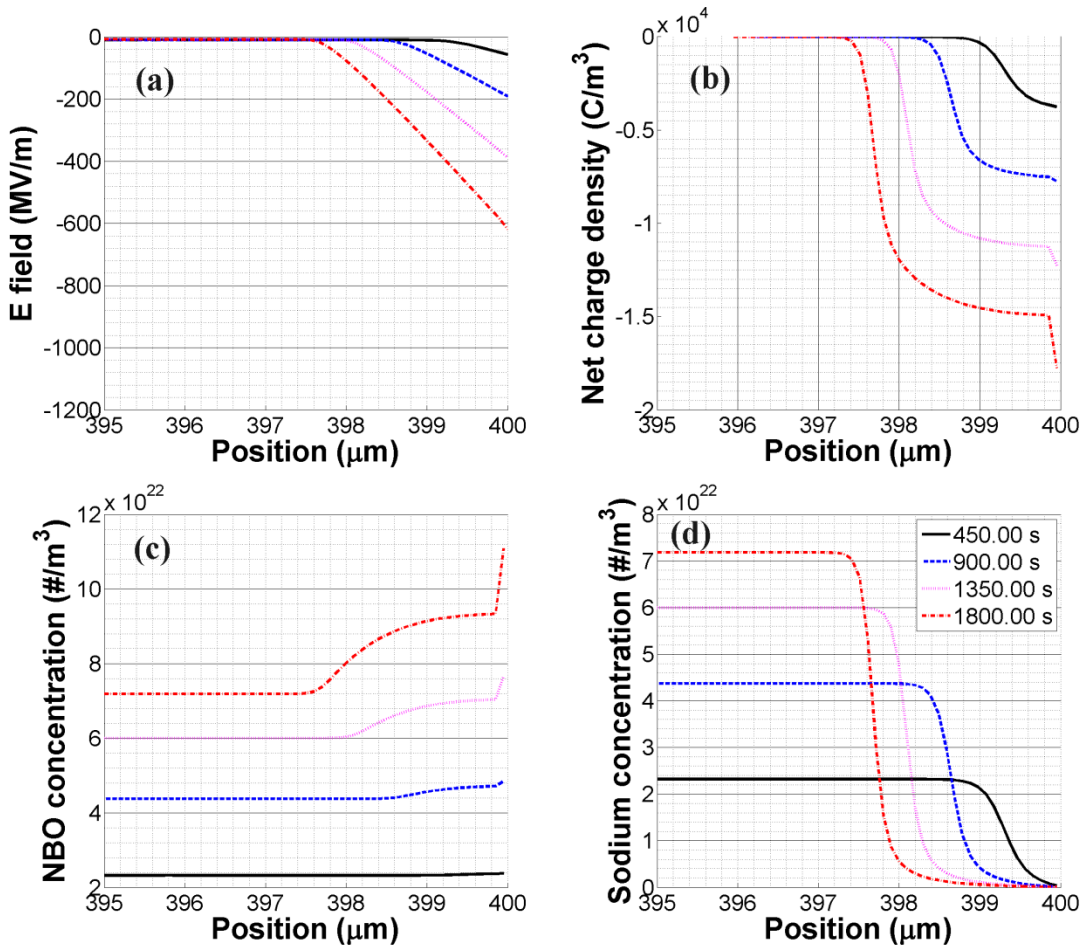

Figure 4-8 Modeling results near the anode (x=400 μm) for thermal poling of AF45 glass at 450 ^{o}C and 4 kV during 30 min ;(a) Electric field, (b) net charge density, (c) NBO concentration, (d) sodium concentration.

thermal poling condition can be determined from Figure 4-8(d), which provides 2.8 μm of depletion width. This simulated depletion width is comparable to the experimental one (2.5 μm) in the Table 4-1.

This numerical method using Proctor model is also applied to 700 μm OA10G glasses at 400 ^{o}C and 4 kV using parameters in Table 4-10. Other parameters are fixed compared to that of AF45 glasses. However, the sodium mobility increased to $9.0x10^{-16}$ $m^2V^{-1}s^{-1}$ to reflect much wider depletion width. Overall behavior is similar to that of AF45 glass. Sodium ions move toward the cathode and NBO ions move toward the anode. Due to the large mobility difference between these two mobile ions negative space charge develops under the anode. The depletion width under the anode for this poling condition reached 5.2 μm as shown in Figure 4-9(d) which is comparable to that of the experimental value (5.9 μm)[19].

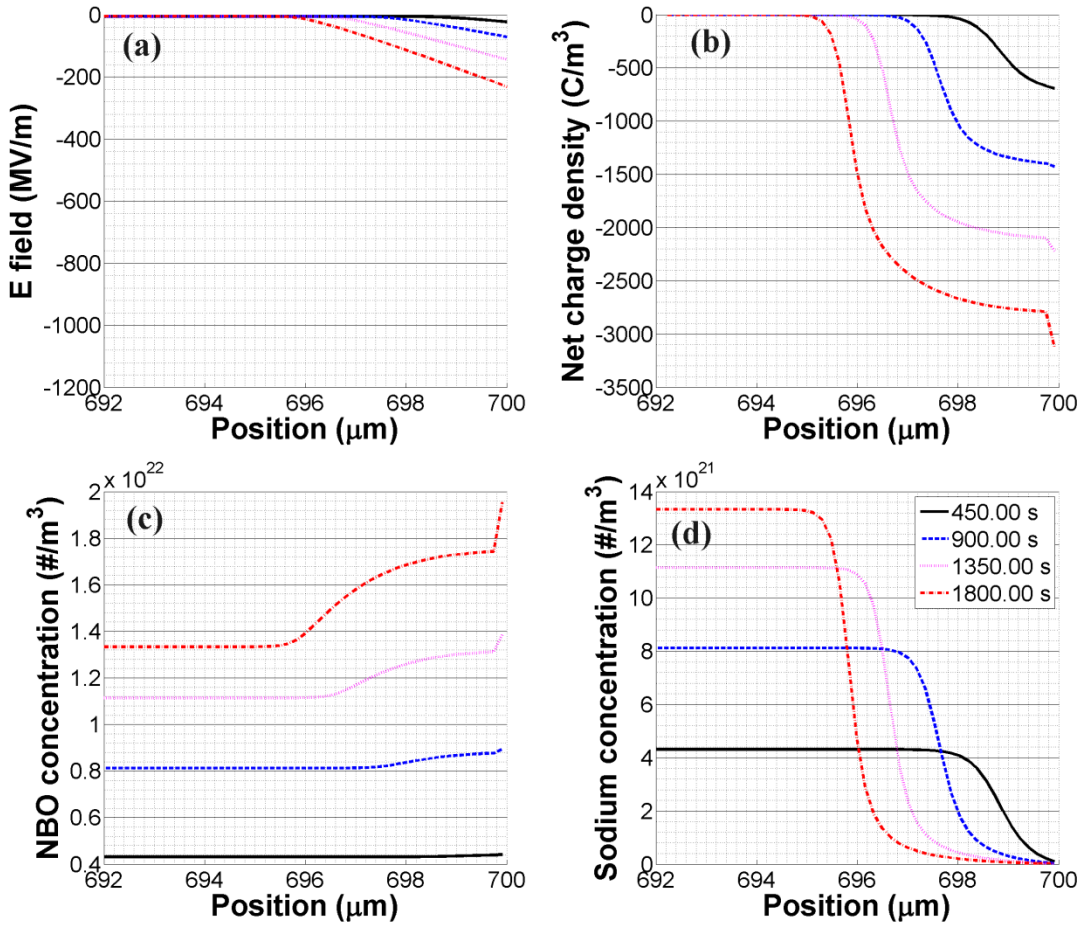

Figure 4-9 Modeling results near the anode (x=700 μm) for thermal poling of OA10G glass at 400 ^{o}C and 4 kV during 30 min ;(a) Electric field, (b) net charge density, (c) NBO concentration, (d) sodium concentration.

4.7.2. Numerical method based on multiple charge carriers

In the previous section, the Proctor model is used to describe thermal poling of low-alkali BAS. According to the model it is assumed that only sodium ions can move during the poling process. However, in low-alkali BAS composition it is also possible that other ions such as O^- and $Ba^{2+}(Ca^{2+})$ move under high electric field near the anode. It is also possible that H_3O^+/H^+ is injected from the anode surface by the high electric field which depends on the atmosphere (vacuum or air), type of electrode (blocking or nonblocking), and the surface etching process. There is no controversy that sodium ions are the fastest ions in low-alkali BAS. However, in the thermal poling condition of 400-450 ^oC and 30 min other mobile ions cannot be excluded. Therefore numerical models for multiple charge carriers in low-alkali BAS will be discussed below.

4.7.2.1. Numerical model based on the sodium and NBO movement

It has been known in the "anodic bonding community" that NBO can move within depletion region in alkali-containing glasses and recently this idea is also presented in the research of glass poling process[7, 17, 18, 29, 56]. This is especially important for the poling in N_2, Ar or vacuum atmosphere or for the case of metalized samples. There are several assumptions for this model to apply low-alkali BAS.

(1) It is assumed that a BAS sample is located at x=0 and x=d and the problem is one dimensional.

(2) Two kinds of charge carriers are present in the glass; sodium ions and NBO ions. It is further assumed that the ratio between NBO mobility to sodium mobility is $2x10^{-4}$[18].

(3) Non-blocking electrode condition is present at the anode and cathode. So charge carriers can be neutralized at the electrode. Injection of hydrogen species through the electrode is also assumed to be negligible.

(4) Sodium and NBO ions can move under the applied electric field (E). Then the current density can be given by

$$j_{Na} = \mu_{Na} epE$$

$$j_{NBO} = \mu_{NBO} enE \tag{4-23}$$

where p and n are mobile sodium and NBO concentration respectively. Others have their usual meaning. Current density from diffusion is ignored in this equation.

(5) The NBO mobility (μ_{NBO}) is assumed to grow exponentially with the magnitude of electric field due to the field-induced decrease of activation energy during glass poling process[18]. Then the NBO mobility can be expressed by

$$\mu_{NBO} = \mu_{NBO}^{0} \exp\left(\frac{elE}{2\varepsilon_r k_B T}\right) \tag{4-24}$$

where μ_{NBO}^{0} is the mobility in weak fields, l mean jump length between NBO sites, ε_r the permittivity of the glass.

The electric field distribution and charge distribution in low-alkali BAS during thermal poling can be described by Eqn. (4-23) and (4-24), the local equation of continuity, and Poisson's equation below

$$\frac{\partial p}{\partial t} = -\frac{\partial j_{Na}}{\partial x} \tag{4-25}$$

$$\frac{\partial n}{\partial t} = -\frac{\partial j_{NBO}}{\partial x} \tag{4-26}$$

$$\frac{\partial E}{\partial x} = \frac{e}{\varepsilon}(p - n) \tag{4-27}.$$

As an initial condition, it is assumed that 9.41×10^{22} #/m^3 of mobile sodium and NBO ions are uniformly distributed in AF45 glass. Modeling parameters for this method are summarized in

Table 4-11. It should be noted that the sodium mobility in this model is smaller than that of Proctor model. This could be justified by the fact that sodium concentration could be higher since ion dissociation and recombination are not assumed in current case.

Figure 4-10 shows simulation results for AF45 glass at 450 ^{o}C and 4 kV during 30 min. Details of the simulation are in Chapter 5.4. Compared to Figure 4-8 (Proctor model) the general trend is similar; sodium ions were depleted under the anode and NBO ions also moved toward the anode. The depletion width (2.1 μm) as shown in Figure 4-10(d) was also similar to both that (2.8 μm) of Proctor model and experimental one (2.5 μm). The most significant difference between them was that NBO ions moved to the anode faster and neutralized there as shown in Figure 4-10(c) due to the field enhanced NBO mobility. The electric field near the anode (x=400 μm) is also smaller than that of Proctor model due to more charge compensation by NBO ions.

Table 4-11 Modeling parameters based on sodium and NBO motion for low-alkali BAS.

	AF45
Thickness (μm)	400
Applied voltage (V)	4000
Poling temperature (^{o}C)	450
Initial sodium concentration (atoms/m^3)	9.41×10^{22}
Initial NBO concentration (atoms/m^3)	9.41×10^{22}
Sodium mobility ($m^2V^{-1}s^{-1}$)	1.0×10^{-16}
NBO mobility ($m^2V^{-1}s^{-1}$) in weak field	2.0×10^{-20}
Jump distance between NBO sites (m)	7×10^{-10}

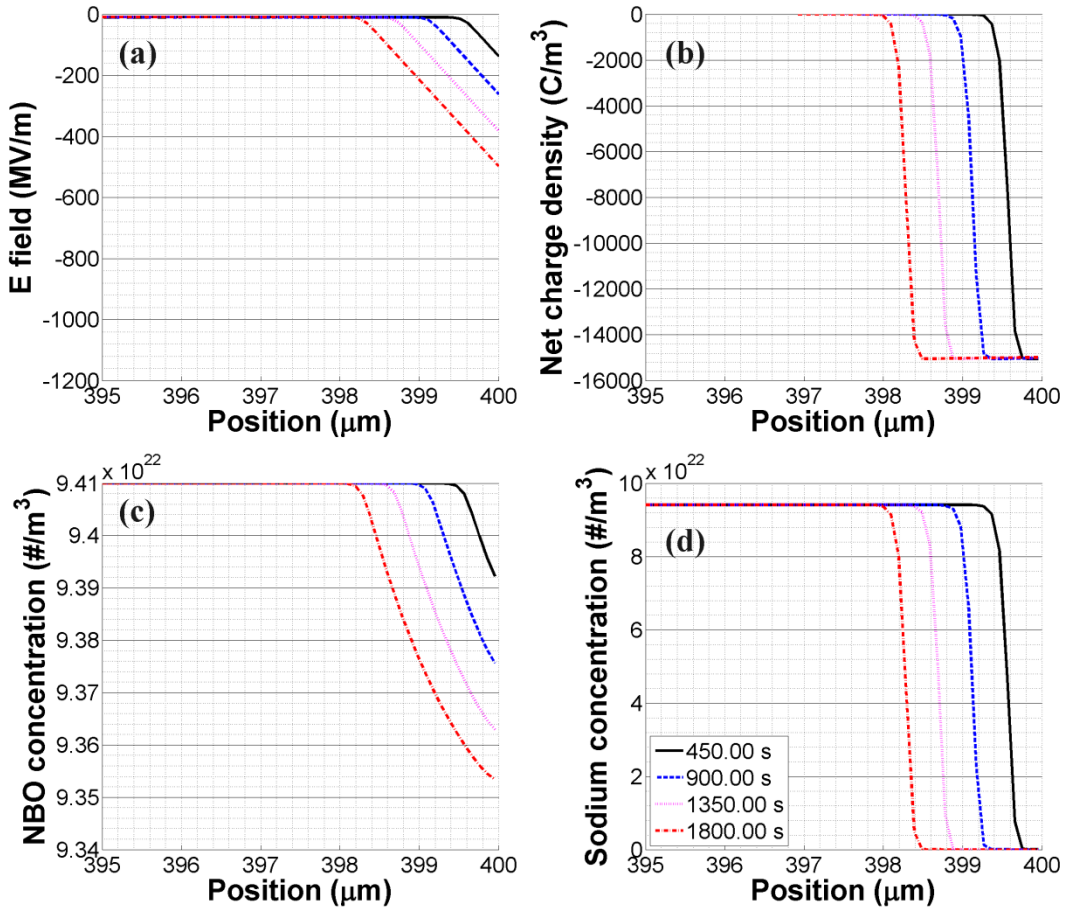

Figure 4-10 Modeling results near the anode (x=400 μm) for thermal poling of AF45 glass at 450 ^{o}C and 4 kV during 30 min assuming sodium and oxygen ion motion ;(a) Electric field, (b) net charge density, (c) NBO concentration, (d) sodium concentration.

4.7.2.2. Numerical model based on the sodium and H_3O^+/H^+ movement

It has been known that application of a dc voltage to an ion-conducting glass at high temperatures will cause field-assisted ion exchange in the case of anodes such as Ag and molten KNO_3[56]. Blocking anodes such as graphite and Pt may also become nonblocking when the furnace atmosphere contains sources of protons (H_2 or H_2O vapor)[56]. Then hydrogenated species can be injected from the surrounding atmosphere after ionization[2, 40]. Anodic proton injection has been experimentally proved for soda-lime glass by elastic recoil detection technique[14, 15]. Therefore in low-alkali BAS there is also possibility for proton injection from the anode due to the high electric field. In our case thermal poling is performed under vacuum atmosphere. However, it is difficult to completely remove H_2O in the equipment and the glass surface could already be hydrogenated. Therefore it is necessary to test two charge carrier model of sodium and proton. There are several assumptions for this model to apply low-alkali BAS.

(1) It is assumed that a BAS sample is located at x=0 and x=d and the problem is one dimensional.

(2) Two kinds of charge carriers are present in the glass; sodium ions and H_3O^+/H^+ ions. It is also assumed that initially there is no H_3O^+/H^+ ions in the glass and it is injected from the anode. The H_3O^+/H^+ injection at the anode can be described by

$$\left.\frac{\partial p_2}{\partial t}\right|_{x=d} = \sigma_2 E(x = d) \qquad (4\text{-}28)$$

where p_2 is H_3O^+/H^+ ions concentration, σ_2 an adjustable parameter describing charge injection into glass, E(x=d) the electric field at the anode. The σ_2 is set to be $5x10^{11}$ $m^{-2}V^{-1}s^{-1}$[39].The ratio between H_3O^+/H^+ ions mobility to sodium mobility is 10^{-2}.

(3) Non-blocking electrode condition is present at the anode and cathode. So charge carriers can be neutralized at the electrode.

(4) Sodium and H_3O^+/H^+ ions can move under the applied electric field (E). Then the current density can be given by

$$j_{Na} = \mu_{Na} e p_1 E$$

$$j_H = \mu_H e p_2 E \qquad (4\text{-}29)$$

where p_1 and p_2 are mobile sodium and H_3O^+/H^+ concentration respectively. Others have their usual meaning. Current density from diffusion is ignored in this equation.

The electric field distribution and charge distribution in low-alkali BAS during thermal poling can be modeled by Eqn. (4-29), the local equation of continuity, and Poisson's equation as discussed in a previous section. Modeling parameters for this method are summarized in Table 4-12. Figure 4-11 shows model results for AF45 glass at 450 ^oC and 4 kV during 30 min using the above model. Compared to Figure 4-8 and Figure 4-10 the general trend is again similar; sodium ions were depleted under the anode and H_3O^+/H^+ ions also moved toward the cathode. The depletion width (2.1 μm) as shown in Figure 4-11(d) was also similar to both that of previous models and experimental one (2.5 μm). The most significant difference from previous model was

Table 4-12 Modeling parameters based on sodium and H_3O^+/H^+ motion for low-alkali BAS.

	AF45
Thickness (μm)	400
Applied voltage (V)	4000
Poling temperature (^oC)	450
Initial sodium concentration (atoms/m^3)	9.41×10^{22}
Sodium mobility ($m^2V^{-1}s^{-1}$)	1.0×10^{-16}
H_3O^+/H^+ mobility ($m^2V^{-1}s^{-1}$)	1.0×10^{-18}
σ_2 ($m^{-2}V^{-1}s^{-1}$)	5.0×10^{11}

that electric field near anode has its maximum not at the anode but inside the glass. This different electric field distribution comes from positive charges(H_3O^+/H^+ ions) accumulated right next to the anode due to the proton injection.

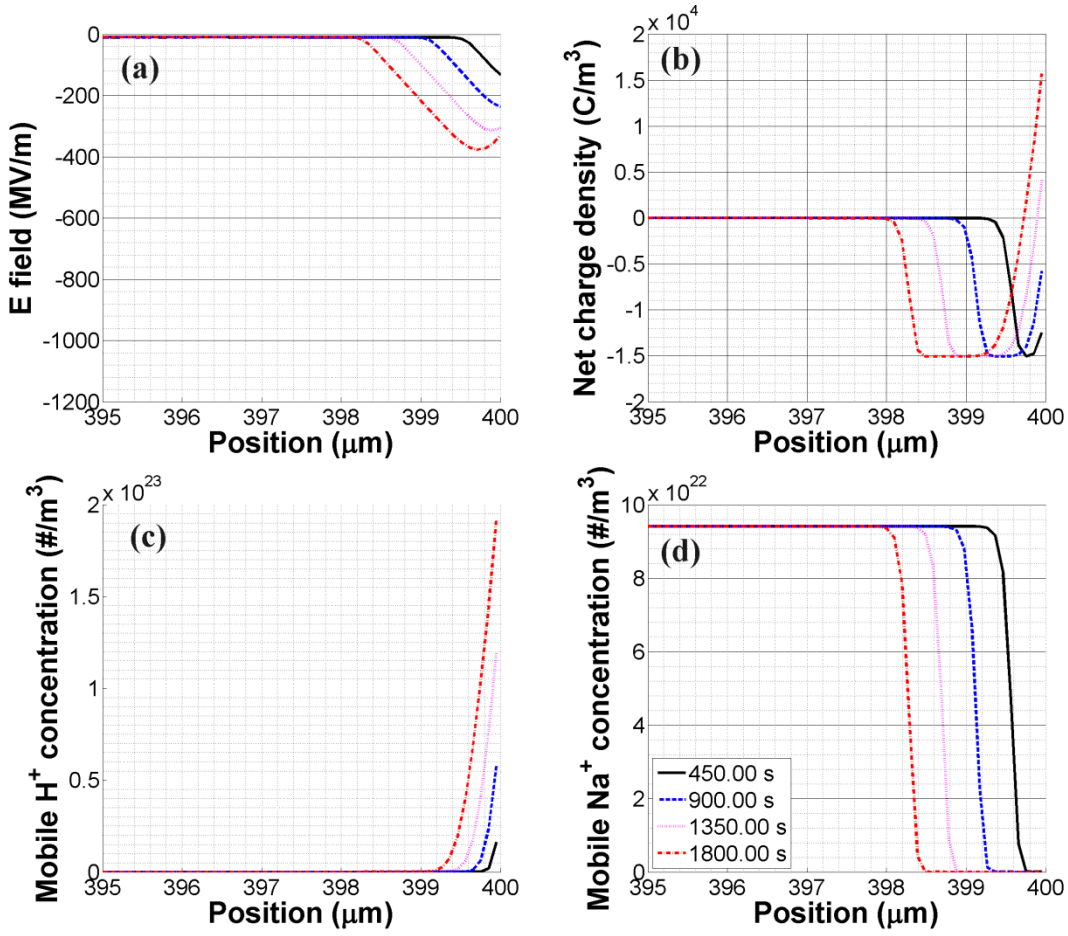

Figure 4-11 Modeling results near the anode (x=400 μm) for thermal poling of AF45 glass at 450 ^oC and 4 kV during 30 min assuming sodium and H_3O^+/H^+ ion motion ;(a) Electric field, (b) net charge density, (c) H_3O^+/H^+ concentration, (d) sodium concentration.

4.7.2.3. Numerical model based on the sodium, barium and H_3O^+/H^+ movement

In the previous section, two charge carrier models are considered for low-alkali BAS. The model is adequate for fused silica glasses where only sodium is an intrinsic mobile cation(H_3O^+/H^+ is an extrinsic cation). However for the case of soda-lime glass and low-alkali BAS there are other mobile cations such as Ca^{2+} and Ba^{2+}. It is known that the Ca^{2+} concentration can be depleted near anode during thermal poling of soda-lime glass[14, 15, 17]. Smith also showed that Ba^{2+} ion is depleted under the anode during thermal poling of AF45 glass at 600 ^oC and 4 kV for 30 min up to 90 nm[23]. Therefore it is necessary to test glass poling model for low-alkali BAS including Na^+, H_3O^+/H^+, and $Ba^{2+}(Ca^{2+})$ using numerical methods. There are several assumptions for this model to apply low-alkali BAS (AF45 glass).

(1) It is assumed that a BAS sample is located at x=0 and x=d and the problem is one dimensional.

(2) Three kinds of mobile charge carriers are present in the glass; sodium ions, barium ions and H_3O^+/H^+ ions. It is also assumed that initially there are no H_3O^+/H^+ ions in the glass which are injected from the anode. The same model for H_3O^+/H^+ injection in previous section is used. The ratio between H_3O^+/H^+ ions mobility to sodium mobility is 10^{-2}. The mobility of Ba^{2+} is set to be $1.0x10^{-20}$ $m^2V^{-1}s^{-1}$ based on Table 4-6.

(3) Non-blocking electrode condition is present at the anode and cathode. So charge carriers can be neutralized at the electrode.

(4) Sodium, barium and H_3O^+/H^+ ions can move under the applied electric field (E). Then the current density can be given by

$$j_i = \mu_i e p_i E \tag{4-30}$$

where the index i denotes one of the positive ionic species (1 is sodium ion, 2 is proton and 3 is barium ion). Current density from diffusion is ignored in this equation.

The electric field distribution and charge distribution in low-alkali BAS(AF45) during thermal poling can be described by Eqn. (4-30), the local equation of continuity, and Poisson's equation below

$$\frac{\partial p_i}{\partial t} = -\frac{\partial j_i}{\partial x} \tag{4-31}$$

$$\frac{\partial E}{\partial x} = \frac{e}{\varepsilon}\sum_i (p_i - p_{0,i}) \tag{4-32}$$

where p_i is the concentration for positive ions, $p_{0,i}$ the initial concentration for positive ions, j_i the current density for positive ions, e the elementary charge, ε the permittivity, respectively. As an initial condition, it is assumed that 9.41×10^{22} #/m^3 of mobile sodium and 2.00×10^{20} #/m^3 of mobile barium ions are uniformly distributed in the AF45 glass. These concentrations are calculated from weak electrolyte theory for glass in chapter 4.7.1. Modeling parameters for this method are summarized in Table 4-13. Figure 4-12 shows model results for AF45 glass at 450 ^oC and 4 kV during 30 min using the above model. Compared to Figure 4-11 the shape of the electric field distribution and mobile ions distribution is similar; sodium ions were depleted under the anode and H_3O^+/H^+ ions also moved toward the cathode. On the other hand, in this case barium ions also contribute to the charge compensation in the depletion region. However the concentration of mobile barium ions is too low to affect electric field distribution and net charge density as shown in Figure 4-11(a) and 4-11(b). The depletion width (2.1 μm) as shown in Figure 4-12(d) was similar to both that of previous models and experimental one (2.5 μm).

Table 4-13 Modeling parameters based on sodium, barium and H_3O^+/H^+ motion for low-alkali BAS.

	AF45
Thickness (μm)	400
Applied voltage (V)	4000
Poling temperature (^oC)	450
Initial sodium concentration (atoms/m^3)	$9.41x10^{22}$
Sodium mobility ($m^2V^{-1}s^{-1}$)	$1.0x10^{-16}$
H_3O^+/H^+ mobility ($m^2V^{-1}s^{-1}$)	$1.0x10^{-18}$
σ_2 ($m^{-2}V^{-1}s^{-1}$)	$5.0x10^{11}$
Initial barium concentration (atoms/m^3)	$2.00x10^{20}$
Barium mobility ($m^2V^{-1}s^{-1}$)	$1.0x10^{-20}$

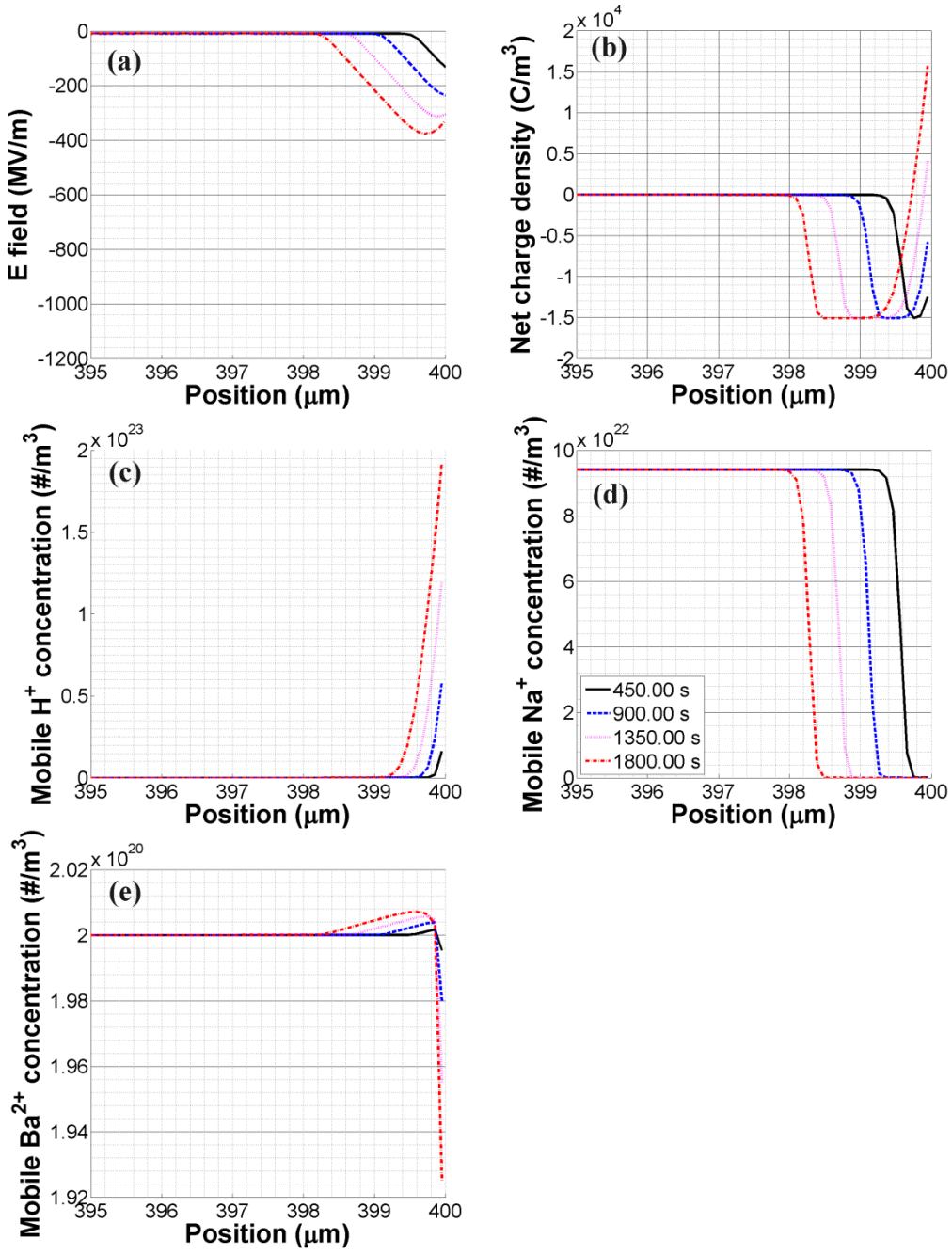

Figure 4-12 Modeling results near the anode (x=400 μm) for thermal poling of AF45 glass at 450 ^{o}C and 4 kV during 30 min assuming sodium, barium and H_3O^+/H^+ ion motion ;(a) Electric field, (b) net charge density, (c) H_3O^+/H^+ concentration, (d) sodium concentration, (e) barium concentration.

4.7.3. Summary of numerical method results for thermal poling in low-alkali BAS

Multiple charge carriers are possible for low-alkali BAS under thermal poling. The main charge carriers can be different according to the poling conditions of temperature, atmosphere, and electrode type. Therefore several numerical methods are tested for thermal poling in low-alkali BAS from single charge carrier model (Proctor model) to multiple charge carrier model including sodium, NBO, H_3O^+/H^+ or barium ions. There are common features in electric field distribution and mobile charge distribution during and after poling; During the poling sodium ions (fastest ions) move toward the cathode and sodium-depleted region build up near the anode. Since sodium-depleted region has negative space charge, the electric field increases towards the anode monotonously unless there is proton injection from the anode. For the case of proton injection, at the right next to the anode there is positive space charge from the proton similar to p-n junction in semiconductors. So the maximum electric field exists inside the depletion region not at the anode. Transport and space charge development of three charge carriers (sodium, barium, and proton ions) in BAS have been investigated through simulation. The electric field development and charge distribution results from three charge carrier model is similar to that of two charge carrier model with sodium and proton ions. However, the charge compensation from barium ions decreases the proton injection from the anode.

4.8. Conclusions

Cation depletion phenomena during thermal poling of low-alkali BAS is studied using a numerical method that is outlined in Chapter 5.4. There are several potential ionic species that are mobile under high electric field in BAS such as $Ba^{2+}(Ca^{2+})$, O^-, H_3O^+/H^+. In order to accurately predict the space charge distribution and the corresponding electric field distribution at the anode, von Hippel's single cation model was extended to multiple cations. A depletion layer formation mechanism was proposed, involving proton ion exchange with sodium ions provides a more realistic estimate of depletion width; however, this analytical model cannot quantify oxygen ion migration or barium ion migration in the depletion region. Therefore numerical methods for thermal poling in low-alkali BAS are developed by assuming two charge carrier (sodium/oxygen or sodium/proton) and three charge carrier models (sodium/barium/proton). These numerical results show that charge compensation from oxygen, proton, or barium can explain much wider depletion width as compared to results from analytical models. Moreover, proton injection accounts for the maximum electric field existing inside the depletion region, which has been experimentally determined through optical measurements[20].

Modeling results of electric field distribution for AF45 glass thermally poled at 450 ^oC and 4 kV after 1800 s are compared in Figure 4-13. When sodium ion is only mobile, the maximum electric field is located at the anode and it decreases toward the cathode. The strength is higher than that of other two models due to no charge compensation. In other two models the maximum electric field is diminished by charge compensation with NBO or $H^+/H_3O^+\&Ba^{2+}$. The maximum electric field is located not at anode but inside the glass for the case of H^+/H_3O^+ & Ba^{2+} compensation. The field distribution for the $H^+/H_3O^+\&Ba^{2+}$ case is similar to the experimentally determined field distribution in BAS glass[20].

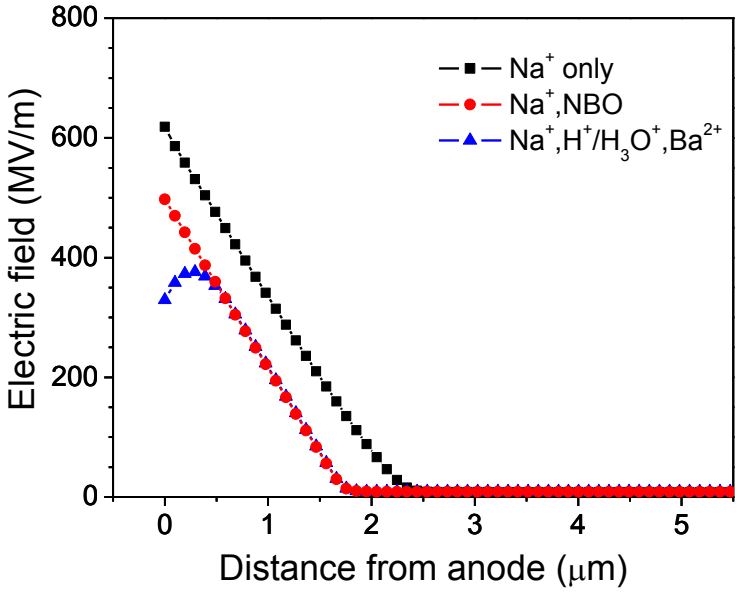

Figure 4-13 Modeling results of electric field for AF45 glass thermally poled at 450 ^{o}C and 4 kV after 1800 s.

Modeling results of mobile ion concentrations for AF45 glass thermally poled at 450 ^{o}C and 4 kV after 1800 s are compared in Figure 4-14. For the case of Proctor model where only sodium ion is mobile its concentration decreased up to 2.8 μm as shown in Figure 4-14(a). For two charge carrier model with Na^+ and NBO the NBO compensates negative space charge built with depletion of sodium ion. However due to its quite slow mobility the amount of displaced NBO is very limited and do not make remarkable difference in mobile sodium and NBO concentrations. For the case of three charge carrier model with Na^+, H^+/H_3O^+, and Ba^{2+} both H^+/H_3O^+ and Ba^{2+} compensate the negative space charge. The amount of displaced H^+/H_3O^+ and Ba^{2+} also are limited and the mobile Na^+ concentration profile is similar to previous two cases.

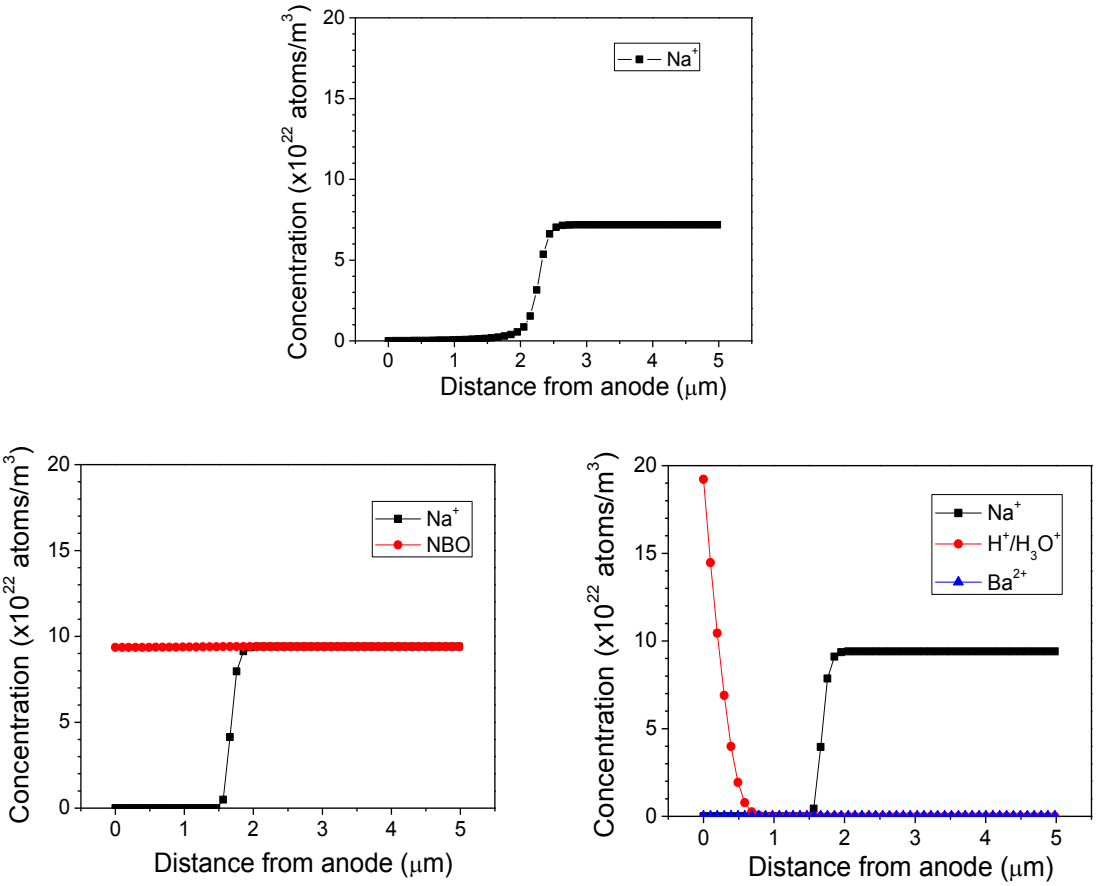

Figure 4-14 Modeling results of mobile ion concentration for AF45 glass thermally poled at 450 ^{o}C and 4 kV after 1800 s; (a) Proctor model, (b) Two carrier model with Na&NBO (c) Three carrier model with Na, $H^{+}/H_3O^{+}/Ba^{2+}$.

4.9. References

1. Schmidt, B., et al., *In situ investigation of ion drift processes in glass during anodic bonding.* Sensors and Actuators A: Physical, 1998. **67**(1): p. 191-198.
2. Alley, T.G., S. Brueck, and R.A. Myers, *Space charge dynamics in thermally poled fused silica.* Journal of Non-Crystalline Solids, 1998. **242**(2): p. 165-176.
3. Myers, R., N. Mukherjee, and S.R. Brueck, *Large second-order nonlinearity in poled fused silica.* Optics Letters, 1991. **16**(22): p. 1732-1734.
4. Long, X.-C. and S. Brueck, *Large-signal phase retardation with a poled electrooptic fiber.* Photonics Technology Letters, IEEE, 1997. **9**(6): p. 767-769.
5. An, H. and S. Fleming, *Second-order optical nonlinearity in thermally poled borosilicate glass.* Applied Physics Letters, 2006. **89**(18): p. 181111-181111-3.
6. An, H. and S. Fleming, *Second-order optical nonlinearity in thermally poled Pyrex borosilicate glass.* Optics Communications, 2008. **281**(5): p. 1263-1267.
7. Carlson, D., *Ion depletion of glass at a blocking anode: I, theory and experimental results for alkali silicate glasses.* Journal of the American Ceramic Society, 1974. **57**(7): p. 291-294.
8. Alley, T.G. and S. Brueck, *Visualization of the nonlinear optical space-charge region of bulk thermally poled fused-silica glass.* Optics Letters, 1998. **23**(15): p. 1170-1172.
9. Pruneri, V., et al., *Thermal poling of silica in air and under vacuum: The influence of charge transport on second harmonic generation.* Applied Physics Letters, 1999. **74**(17): p. 2423-2425.
10. Alley, T.G., S. Brueck, and M. Wiedenbeck, *Secondary ion mass spectrometry study of space-charge formation in thermally poled fused silica.* Journal of Applied Physics, 1999. **86**(12): p. 6634-6640.
11. Triques, A., et al., *Depletion region in thermally poled fused silica.* Applied Physics Letters, 2000. **76**(18): p. 2496-2498.
12. Faccio, D., V. Pruneri, and P. Kazansky, *Dynamics of the second-order nonlinearity in thermally poled silica glass.* Applied Physics Letters, 2001. **79**(17): p. 2687-2689.
13. An, H., S. Fleming, and G. Cox, *Visualization of second-order nonlinear layer in thermally poled fused silica glass.* Applied Physics Letters, 2004. **85**(24): p. 5819-5821.
14. Krieger, U.K. and W.A. Lanford, *Field assisted transport of Na^+ ions, Ca^{2+} ions and electrons in commercial soda-lime glass I: Experimental.* Journal of Non-Crystalline Solids, 1988. **102**(1): p. 50-61.
15. Lepienski, C., et al., *Electric field distribution and near-surface modifications in soda-lime glass submitted to a dc potential.* Journal of Non-Crystalline Solids, 1993. **159**(3): p. 204-212.
16. An, H. and S. Fleming, *Near-anode phase separation in thermally poled soda lime glass.* Applied Physics Letters, 2006. **88**(18): p. 181106-181106-3.
17. Ziemath, E., V. Araujo, and C. Escanhoela, *Compositional and structural changes at the anodic surface of thermally poled soda-lime float glass.* Journal of Applied Physics, 2008. **104**(5): p. 054912-054912-7.
18. Dussauze, M., et al., *How does thermal poling affect the structure of soda-lime glass?* The Journal of Physical Chemistry C, 2010. **114**(29): p. 12754-12759.
19. Smith, N.J., M.T. Lanagan, and C.G. Pantano, *Thermal poling of alkaline earth boroaluminosilicate glasses with intrinsically high dielectric breakdown strength.* Journal of Applied Physics, 2012. **111**(8): p. 083519-083519-9.

20. Dash, P., *Dynamics of Space Charge Polarization and Electrical Conduction in Low Alkali Boroaluminosilicate glasses,* in *Engineering Science and Mechanics*. 2013, The Pennsylvania State University: University Park.
21. Doi, A., *Ionic conduction and conduction polarization in oxide glass.* Journal of Materials Science, 1987. **22**(3): p. 761-769.
22. Sun, T., et al., *Effects of MO (M=Ba, Mg, Ca) on the crystallization of B_2O_3–Al_2O_3–SiO_2 glass-ceramics.* Ceramics International, 2009. **35**(3): p. 1051-1055.
23. Smith, N.J., *Novel Approaches to the Surface Modification of Glass by Thermo-electric Poling*. 2011, Pennsylvania State University.
24. Lanford, W., et al., *Hydration of soda-lime glass.* Journal of Non-Crystalline Solids, 1979. **33**(2): p. 249-266.
25. Lanford, W. and R. Golub, *Hydrogen surface contamination and the storage of ultracold neutrons.* Physical Review Letters, 1977. **39**: p. 1509-1512.
26. Ernsberger, F.M., *The role of molecular water in the diffusive transport of protons in glasses.* Physics and Chemistry of Glasses, 1980. **21**(4): p. 146-149.
27. Ernsberger, F.M., *The nonconformist ion.* Journal of the American Ceramic Society, 1983. **66**(11): p. 747-750.
28. Nogami, M. and Y. Abe, *Evidence of water-cooperative proton conduction in silica glasses.* Physical Review B, 1997. **55**(18): p. 12108.
29. Carlson, D., K. Hang, and G. Stockdale, *Electrode "Polarization" in Alkali-Containing Glasses.* Journal of the American Ceramic Society, 1972. **55**(7): p. 337-341.
30. Petrov, M., Y.A. Lepenkin, and A. Lipovskii, *Polarization of glass containing fast and slow ions.* Journal of Applied Physics, 2012. **112**(4): p. 043101-043101-8.
31. Stagg, J., *Drift mobilities of Na and K ions in SiO films.* Applied Physics Letters, 1977. **31**: p. 532.
32. MECHA, J. and J. STEINMANN, *Mobility of sodium ions in silica glass of different OH content.* Journal of the American Ceramic Society, 1979. **62**(7-8): p. 343-346.
33. Drury, T. and J. Roberts, *Diffusion in silica glass following reaction with tritiated water vapour.* Physics and Chemistry of Glasses (England), 1963. **4**.
34. Shin, D.W. and M. Tomozawa, *Effects of fictive temperature and water content on electrical conductivity of silica glasses.* Journal of Non-Crystalline Solids, 1996. **203**: p. 262-267.
35. Page, M., R. Oven, and D. Ashworth, *Scaling rules for glass based planar optical waveguides made by field assisted ion diffusion.* Electronics Letters, 1991. **27**(22): p. 2073-2076.
36. Tian, L. and R. Dieckmann, *Sodium tracer diffusion in an alkaline-earth boroaluminosilicate glass.* Journal of Non-Crystalline Solids, 2000. **265**(1): p. 36-40.
37. Hetherington, G., K. Jack, and M. Ramsay, *The high-temperature electrolysis of vitreous silica, part I. Oxidation, ultra-violet induced fluorescence, and irradiation colour.* Physics and Chemistry of Glasses, 1965. **6**(1): p. 6-15.
38. Doremus, R.H., *Mechanism of electrical polarization of silica glass.* Applied Physics Letters, 2005. **87**(23): p. 232904-232904-2.
39. Kudlinski, A., Y. Quiquempois, and G. Martinelli, *Modeling of the $\chi^{(2)}$ susceptibility time-evolution in thermally poled fused silica.* Optics Express, 2005. **13**(20): p. 8015-8024.
40. Ikeda, H., et al., *Generation of alkali-free and high-proton concentration layer in a soda lime glass using non-contact corona discharge.* Journal of Applied Physics, 2013. **114**: p. 063303.

41. Kreuer, K., *Proton-conducting oxides.* Annual Review of Materials Research, 2003. **33**(1): p. 333-359.
42. Natrup, F., et al., *Cation diffusion and ionic conductivity in soda-lime silicate glasses.* Physical Chemistry Chemical Physics, 2005. **7**(11): p. 2279-2286.
43. Grofmeier, M., F. Natrup, and H. Bracht, *Barium diffusion in mixed cation glasses.* Physical Chemistry Chemical Physics, 2007. **9**(43): p. 5822-5827.
44. Natrup, F., et al., *Diffusion of calcium and barium in alkali alkaline-earth silicate glasses.* Physical Chemistry Chemical Physics, 2002. **4**(14): p. 3225-3231.
45. von Hippel, A., et al., *Photocurrent, Space-Charge Buildup, and Field Emission in Alkali Halide Crystals.* Physical Review, 1953. **91**(3): p. 568-579.
46. Thamboon, P. and D. Krol, *Microscopic origins of the induced $\chi^{(2)}$ in thermally poled phosphate glasses.* Journal of Applied Physics, 2009. **105**(11): p. 113118-113118-11.
47. Smith, N.J., et al., *Alkali-free glass as a high energy density dielectric material.* Materials Letters, 2009. **63**(15): p. 1245-1248.
48. Murata, T., et al., *Electrode-Limited Dielectric Breakdown of Alkali Free Glass.* Journal of the American Ceramic Society, 2012.
49. Liu, X.-M. and M.-D. Zhang, *Theoretical study for thermal/electric field poling of fused silica.* Japanese Journal of Applied Physics, 2001. **40**: p. 4069.
50. Prieto, X. and J. Liñares, *Increasing resistivity effects in field-assisted ion exchange for planar optical waveguide fabrication.* Optics Letters, 1996. **21**(17): p. 1363-1365.
51. Proctor, T. and P.M. SUTTON, *Space-Charge Development in Glass.* Journal of the American Ceramic Society, 1960. **43**(4): p. 173-178.
52. Quiquempois, Y., N. Godbout, and S. Lacroix, *Model of charge migration during thermal poling in silica glasses: Evidence of a voltage threshold for the onset of a second-order nonlinearity.* Physical Review A, 2002. **65**(4): p. 043816.
53. Souquet, J.-L., M.L.F. Nascimento, and A.C.M. Rodrigues, *Charge carrier concentration and mobility in alkali silicates.* The Journal of Chemical Physics, 2010. **132**: p. 034704.
54. Dash, P., et al., *Activation energy for alkaline-earth ion transport in low alkali aluminoborosilicate glasses.* Applied Physics Letters, 2013. **102**: p. 082904.
55. Lee, H., et al., *Dielectric Breakdown of Thinned $BaO–Al_2O_3–B_2O_3–SiO_2$ Glass.* Journal of the American Ceramic Society, 2010. **93**(8): p. 2346-2351.
56. Carlson, D., *Anodic proton injection in glasses.* Journal of the American Ceramic Society, 1974. **57**(11): p. 461-466.

Chapter 5: Dielectric breakdown mechanism for low-alkali boroaluminosilicate glass

5.1. Introduction

Low-alkali boroaluminosilicate glasses are of interest for electrostatic energy storage since they have exceptionally high dielectric breakdown strength. It has been reported that barium boroaluminosilicate glasses and calcium boroaluminosilicate glasses have dielectric breakdown strengths exceeding 1000 MV/m and electrostatic energy density values as high as 38 J/cm^3[1-3]. In general, many commercial glasses have high dielectric breakdown strengths as reported for Pyrex glasses (900 MV/m) and silica glasses (700 MV/m)[4, 5]. Barium boroaluminosilicate glasses or calcium boroaluminosilicate glasses are attractive for portable or pulsed power applications because large-scale production processes for flat panel display glass provide commercially available glass sheets that are thin (10 -700 μm) and defect-free in addition to flat and smooth pristine surfaces.

In Chapter 2, several dielectric breakdown mechanisms are discussed which include electronic breakdown, thermal breakdown, electromechanical breakdown, and partial discharge breakdown. Among them, partial discharge breakdown can be excluded for the breakdown mechanism since very low porosity within the low-alkali boroaluminosilicate glasses. Therefore in this chapter, the three other breakdown theories will be applied to the glass system in order to determine the most likely breakdown mechanism.

5.2. Experimental breakdown strengths for low-alkali boroaluminosilicate glass

Dielectric breakdown tests are performed for two types of low-alkali boroaluminosilicate glasses as a function of thickness, temperature, and voltage ramp rate. The glasses used for the current research were manufactured by Schott Glass (Germany) and Nippon Electric Glass (Japan) respectively commercially known as AF45 and OA10G. The compositions of glasses are summarized in Table 5-1. These glasses are boroaluminosilicate glasses containing alkaline earth and have alkali contents below 500 ppm. To further reduce the thickness of as-received AF45 and OA10G glasses they are etched using hydrofluoric acid. The detail of etching process is explained in published papers by our group[2, 3]. Gold and platinum are deposited on top and bottom surfaces of the etched glass sample by sputter equipment (Bal-Tec SCD 050 sputter coater, Canonsburg, PA) to fabricate capacitor structures for dielectric breakdown measurements. The electrode spot area on top surfaces varied from 1.5 mm^2 to 3.1 mm^2. The electrode thickness was between 20 and 50 nm. The bottom electrodes were continuous and uniform films of gold or platinum. Dielectric breakdown measurements were performed on the electroded samples by immersing them in a bath containing dielectric fluid (Galden HT-200; Solvay Solexis, Houston, TX) onto a baseplate of high-conductivity copper connected to 30 kV-max DC high voltage supply (Model 30/20; Trek, Medina, NY). Each electrode spot on the top surface of the glass was contacted with a grounded and spring-loaded steel pin (0.66 mm diameter). The voltage was ramped at a constant linear rate between 100 and 5000 V/s. For high temperature breakdown tests above 200 ^oC dielectric fluid was not used and tests were performed in air atmosphere.

Table 5-1 Low-alkali boroaluminosilicate glass compositions used for this study[6].

Mole%	SiO_2	B_2O_3	Al_2O_3	MgO	CaO	SrO	BaO	As_2O_3	SnO_2	Na_2O
AF45	63.6	15.0	9.1			0.163	11.9	0.33	0.0007	0.074
OA10G	66.7	9.2	10.7	0.5	9.6	3.0	0.2		0.101	0.018

5.2.1. Effects of glass thickness on breakdown strengths of AF45 and OA10G glasses

Dielectric breakdown strengths at room temperature for AF45 glasses are summarized in Figure 5-1 as a function of thickness. Gold was used for electrodes and thickness of glass samples ranges from 5 to 50 μm. Samples with different thickness are obtained through etching from the as-received thickness of 50 μm. AF45 glasses were tested with linear voltage ramp rates of 100 V/s. As shown in Figure 5-1, there are two different thickness dependencies for the glass material[2]. At the lower thickness region the breakdown strengths are weakly thickness dependent. At the higher thickness region the breakdown strengths are strongly thickness dependent.

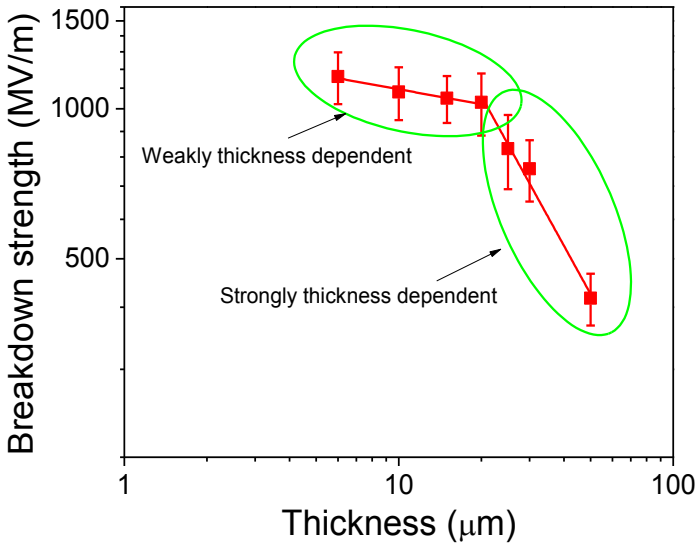

Figure 5-1 Dielectric breakdown strengths for AF45 (Au electrodes) as a function of thickness at room temperature(Electrode : Au, ramp rate : 100 V/s, electrode area : 1.583 mm^2, oil)[2].The error bars indicate a standard deviation of 1σ where Weibull distribution approximates Gaussian distribution for a Weibull modulus exceeding 3.

Dielectric breakdown strengths at room temperature for OA10G glasses are summarized in Figure 5-2 as a function of thickness. Gold and platinum were used as electrodes for as-received or etched OA10G glasses whose thickness ranges from 5 to 50 μm. As-received glasses with different thickness were provided by Nippon Electric Glasses Corporation. The glasses were tested with linear voltage ramp rates of 500 V/s. Similar to the AF45 glasses there are also two different dependencies of breakdown strengths on glass thickness; below 20 μm the breakdown strengths are weakly thickness dependent. Above 20 μm they are strongly thickness dependent.

From the thickness dependence of breakdown strengths for AF45 and OA10G glasses at room temperature, it can be concluded that there are two distinct regions for both glasses; A low thickness regime in which the dielectric breakdown has a weak thickness dependence and a high thickness regime in which the dielectric breakdown strength has a strong thickness dependence.

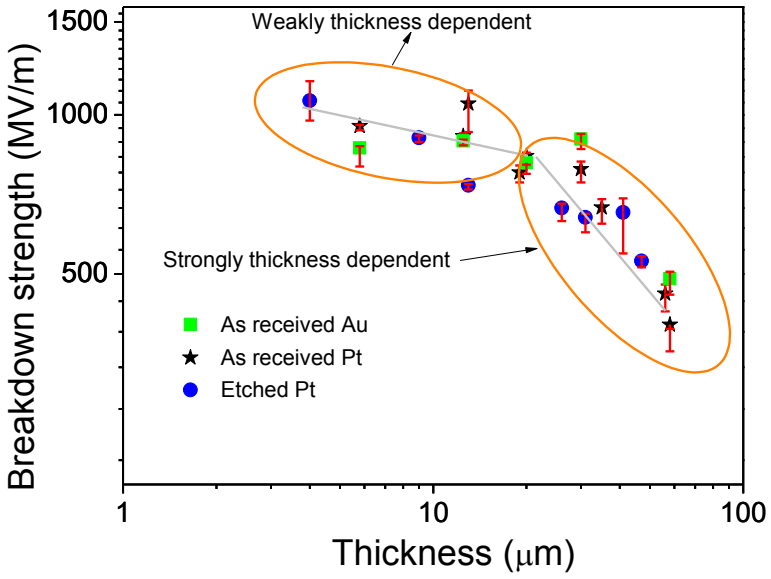

Figure 5-2 Dielectric breakdown strengths for OA10G (etched and as-received samples) as a function of thickness at room temperature(Electrode : Au or Pt, ramp rate : 500 V/s, electrode area : 3.1 mm^2, oil)[2].The error bars indicate 95% confidence level for Weibull analysis.

5.2.2. Effects of temperature on breakdown strengths of AF45 and OA10G glasses

Temperature dependence of breakdown strength is an important property especially for high temperature capacitor applications and understanding the fundamental breakdown mechanism. Figure 5-3 shows temperature dependence of breakdown strengths for AF45 glasses with 15 and 50 μm thicknesses. Gold was used as electrodes and temperature ranges from 25 to 150 ^{o}C. Glasses were tested with linear voltage ramp rate of 500 V/s. At 25 ^{o}C AF45 glass with 15 μm thickness showed breakdown strength of 1050 MV/m and it decreased to 626 MV/m as temperature rose to 100 ^{o}C. When temperature was further increased to 150 ^{o}C, the breakdown strength was unchanged within experimental error. AF45 glasses with 50 μm thickness show a different trend. As temperature increased to 100 ^{o}C the breakdown strength did not change within experimental errors. As temperature further increased to 150 ^{o}C the breakdown strength decreased to 324 MV/m.

So in conclusion, the dielectric breakdown strengths of the AF45 samples decreased about 30 % as the temperature increased to 175 ^{o}C from room temperature.

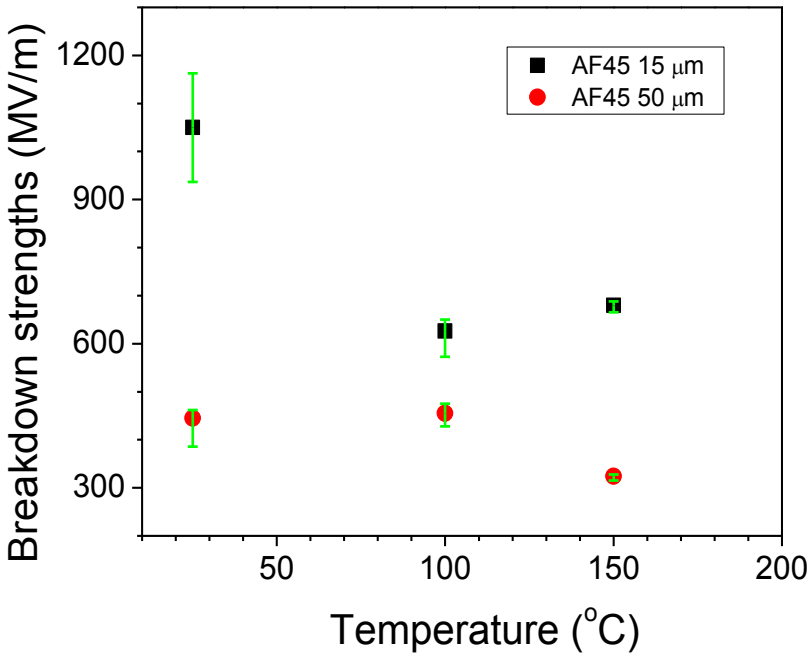

Figure 5-3 Dielectric breakdown strengths as a function of temperature for AF45 glasses with 15 (etched) and 50 μm(as-received) thicknesses; Electrode : Au, ramp rate : 500 V/s, electrode area : 3.1 mm^2, oil. The error bars indicate 95% confidence level for Weibull analysis except AF45 15 μm at room temperature (standard deviation in this case).

5.2.3. Effects of voltage ramp rate on breakdown strengths of OA10G glasses

Dependence of breakdown strengths on voltage ramp rate could be used as a criterion to determine a breakdown mechanism since electronic breakdown mechanisms such as avalanche and intrinsic breakdown are independent of a linear voltage ramp rate. Figure 5-4 shows ramp rate dependence of breakdown strengths for OA10G glasses with 5 and 10 μm thicknesses. Gold was used as electrodes and linear voltage ramp rate ranges from 50 to 5000 V/s. Glasses were tested at room temperature. Breakdown strengths of as-received 5 μm OA10G glasses are independent of voltage ramp rate. However, breakdown strengths of as-received 10 μm OA10G glasses increased from 841 to 1042 MV/m as the ramp rate increased from 500 to 5000 V/s. So the ramp rate affects the breakdown strengths differently for two different thicknesses.

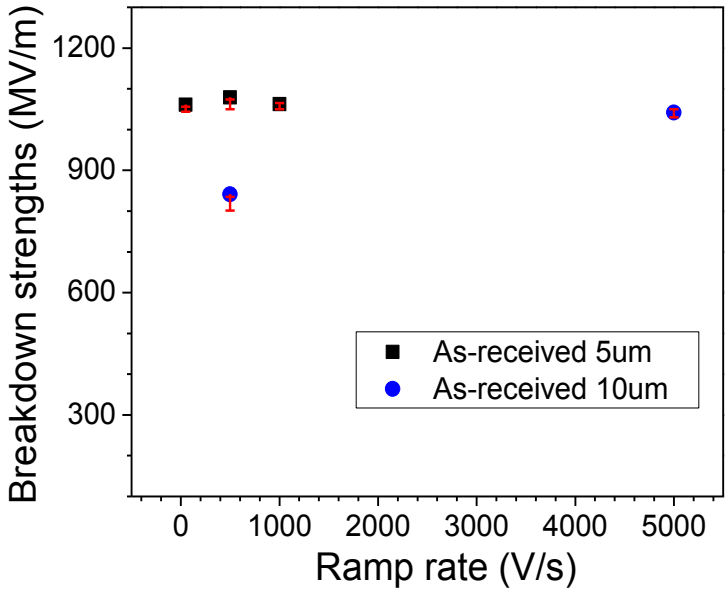

Figure 5-4 Dielectric breakdown strengths for as-received OA10G glasses as a function of ramp rate at room temperature (Electrode: Au, electrode area: 3.1 mm^2, oil). The error bars indicate 95% confidence level for Weibull analysis.

Figure 5-5 further investigates whether temperature affects the dependence of breakdown strength on voltage ramp rate. The breakdown strength at 135 ^{o}C was similar to that at room temperature and the breakdown strength at 100 ^{o}C is also expected to be similar. Therefore the breakdown enhancement at 100 ^{o}C was similar to the increase at room temperature. Within this temperature range there is no dependence of breakdown strength on voltage ramp rate.

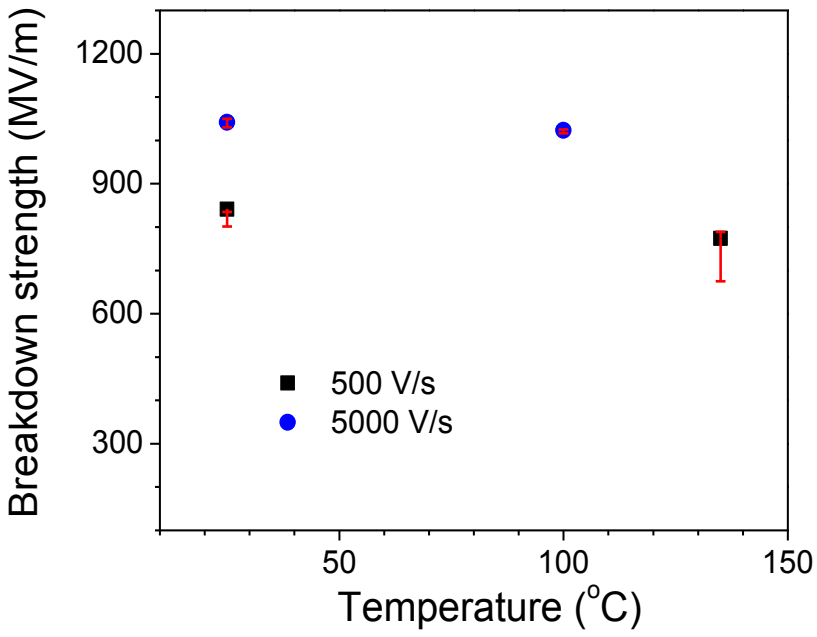

Figure 5-5 Dielectric breakdown strength of as-received 10 μm OA10G glasses as a function of temperature for two different linear voltage ramp rates (Electrode : Au, electrode area : 3.1 mm^2, oil). The error bars indicate 95% confidence level for Weibull analysis.

5.2.4. Summary of experimental breakdown strengths of low-alkali BAS

Thickness dependence of breakdown strengths for both AF45 and OA10G glasses at room temperature show that there are two distinct regimes; A low thickness regime in which the dielectric breakdown is weakly thickness dependent and a high thickness regime in which the dielectric breakdown strength strongly thickness dependent. For temperature dependence of breakdown strengths AF45 glasses with 15 and 50 μm thicknesses show 30 % decrease as temperature increases from room temperature to 150 ^{o}C.

5.3. Application of electromechanical breakdown mechanism to experimental breakdown strengths for low-alkali boroaluminosilicate glass

Electromechanical breakdown mechanism can be attributed to the instability from energy imbalance between the electrostatic energy and the mechanical energy. This breakdown strength (E_b) is given by

$$E_b = \frac{V}{d_0} = 0.6\left(\frac{Y}{\varepsilon_r \varepsilon_0}\right)^{1/2} \quad (5\text{-}1)$$

where V is the applied voltage, d_0 the initial dielectric thickness, Y the Young's modulus, ε_r the permittivity. Therefore if Y and ε_r are known, the electromechanical breakdown can be estimated. The parameters used for this calculation and results are summarized in Table 5-2. This electromechanical breakdown mechanism predicts much higher breakdown strength (about 20 times) compared to experimental breakdown strength. Therefore the assumption of an electromechanical breakdown is unrealistic for low-alkali boroaluminosilicate glass system.

Table 5-2 Theoretical electromechanical breakdown strength from Stark and Garton relationship (Eqn. (5-1))[1, 2, 7, 8].

Material	Young's modulus (GPa)	Permittivity	Theoretical electromechanical breakdown strength (MV/m)	Experimental breakdown strength MV/m
AF45	66	6.0	21,000	1160
OA10G	73	5.3	24,000	953

5.4. Numerical model for breakdown strengths of low-alkali boroaluminosilicate glass

5.4.1. Thermal and electronic breakdown combined model assuming electronic conduction

5.4.1.1. Theoretical background for the breakdown model assuming electronic conduction

Electronic breakdown is initiated by the local electric field enhancement from space charge formation and thermal breakdown occurs from Joule heating by conduction current. Thermal breakdown is explained by the following power balance equation

$$C_v \frac{\partial T}{\partial t} - \mathrm{div}(\kappa \nabla T) = JE \qquad (5\text{-}2)$$

where T is the local temperature, t the time, C_v the volumetric heat capacity, κ the thermal conductivity, J the transient current density, and E the local electric field. At the breakdown criterion, thermal breakdown occurs when a local temperature in the dielectric attains the melting temperature of the glass. For impulse thermal breakdown, thermal conduction is ignored, and this assumption has often been used to model breakdown process in the dielectric due to the simple mathematical relationship[9, 10]. However, impulse thermal breakdown is only valid if the time to breakdown is smaller than thermal relaxation time[11]. For AF45 glass with thickness of 6 μm the time to breakdown is about 70 seconds at 25 ^{o}C assuming 100 V/s of ramp rate. Meanwhile, the thermal relaxation time (τ_d) governed by

$$\tau_d = \frac{d^2 C_v}{4\kappa} \qquad (5\text{-}3)$$

where d is the sample thickness shows about 15 μs. The time to breakdown is much longer than the thermal relaxation time. Then thermal conduction cannot be ignored and assumption of impulse thermal breakdown is invalid in this case. Instead of impulse thermal breakdown Eqn. (5-2) is used to model thermal breakdown.

Considering that the thickness is much smaller than the width and breadth of the sample, a one-dimensional problem can be assumed for thermal breakdown. The governing equation for thermal breakdown reduces to

$$C_v \frac{\partial T}{\partial t} - \kappa \frac{\partial^2 T}{\partial x^2} = J(x,t)E(x,t) \qquad (5\text{-}4)$$

where x is the distance from the cathode in the direction of thickness. It is assumed that the thermal conductivity is independent of temperature.

Charge injection and space charge formation in dielectric materials are closely related to the electronic breakdown. Space charge dynamics play an important part in breakdown process because it governs the local electric field. It has been experimentally demonstrated that under high dc electric field the charge injection and space charge formation occurs in polyethylene and polypropylene[9, 12-16]. In our breakdown model, it is assumed that injected charges from electrodes produce space charge within bulk and its electric field enhancement determine the breakdown. For breakdown criterion, it occurs when local electric field within the bulk reaches intrinsic breakdown strength of glass. The intrinsic breakdown strength of glass is determined based on the literature and set to 1160 MV/m[2].

The theoretical breakdown field based on electronic and thermal models can be determined if the electric field and the temperature in the insulator is numerically calculated for each time and each position. For every time step, the local temperature is compared with the melting point and the local electric field is compared with intrinsic breakdown strength. Dielectric breakdown occurs when either of the two criteria is reached. Both electric field and temperature can be evaluated from charge injection and charge transport through Poisson's equation and Joule heating.

In this model, the charge generation and transport are described by charge injection and conduction of electrons where the motion of holes is ignored. Charge carriers are injected at the

interface of electrode/dielectric according to the Schottky process. Under an externally applied electric field, electrons move within the dielectric towards the anode. Initially no charges are assumed within the dielectric. Dipolar polarization has been ignored for the simplicity.

Assuming one-dimensional problem along the thickness, the current densities at the cathode (x=0) from the Schottky mechanism is governed by

$$J(0,t) = AT^2 \exp\left(\frac{-w_i}{k_B T}\right) \exp\left(\frac{e}{k_B T}\sqrt{\frac{eE(0,t)}{4\pi\varepsilon}}\right) \quad (5\text{-}5)$$

where J(0,t) is the flux of electrons at cathode, A the Richardson constant, T the temperature, k_B the Boltzmann constant, E(0,t) the electric fields at the cathode, ε the permittivity of the dielectric, e the elementary charge, w_i the potential barriers for electrons. Assuming no extraction barrier at the electrode, extraction current density for electrons at the anode is described by

$$J(d,t) = \mu n(d,t) E(d,t) \quad (5\text{-}6)$$

where n is the charge density for electrons, and μ is the mobility for electrons.

The behavior of charge carriers within dielectrics as a function of time and distance are governed by three fundamental equations:

for Poisson's equation

$$\frac{\partial E(x,t)}{\partial x} = \frac{n(x,t)}{\epsilon} \quad (5\text{-}7),$$

for transport equation

$$J(x,t) = \mu n(x,t) E(x,t) \quad (5\text{-}8),$$

for continuity equation

$$\frac{\partial n(x,t)}{\partial t} + \frac{\partial J(x,t)}{\partial x} = 0 \quad (5\text{-}9),$$

where E is the electric field, n the charge density for electrons.

To solve the coupled problem of Eqn. (5-4), (5-7), (5-8), and (5-9) for our breakdown model, several numerical techniques are utilized. The electric field and potential in the dielectric are evaluated using finite difference method (FDM) through direct discretization of Eqn. (5-7) as

shown in Figure 5-6. The modeled glass sample is divided into m slices and the electric field difference at each cell associated with the net charge density can be calculated with the boundary condition. The continuity equation, Eqn. (5-9), can be evaluated using upwind scheme. The time step in the calculation is selected based on the condition of Courant-Friedrichs-Lewy (CFL) which is necessary for the stability of the numerical technique. The power balance equation, Eqn. (5-4), can be calculated using the FDM with the backward Euler method in time and the forward Euler method in spatial coordinate. The backward Euler method in time is applied due to its superior numerical stability regardless of the time step although the computation is much rigorous.

The important part for solving this problem numerically is to determine the electron mobility and Schottky barrier height for electron injection. This could be performed either by experiments or literature reviews. In our case these parameters are obtained from literature reviews and summarized in Table 5-3. The Schottky barrier is calculated from the work function of Au electrodes (5.4 eV) and the electron affinity of glass material. The electron affinity (4.5 eV) of borosilicate glass (Corning No. 774) is assumed for that of this glass material[17]. The electron mobility is assumed to be limited by traps within the bulk and often called as ‘trap-limited mobility’. Therefore the electron mobility is given by the multiplication of trap-free electron mobility and the ratio of free electrons to total electrons. The trap-free electron mobility is

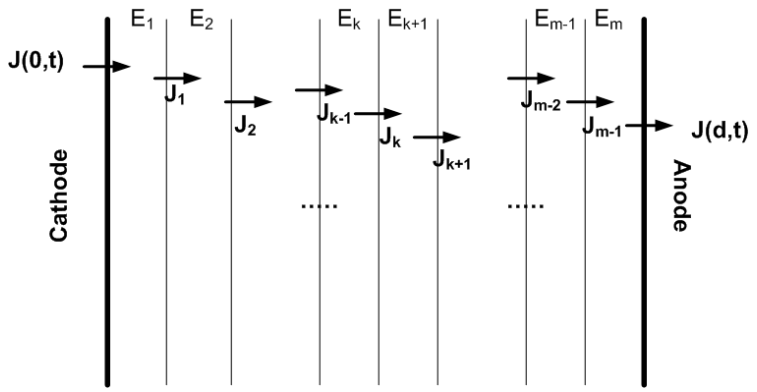

Figure 5-6 Discretization of modeled glass dielectric under breakdown tests.

assumed to be that ($5x10^{-9}$ m^2/Vs) of borosilicate glass. The ratio of free electrons to total electron is difficult to determine and usually affected by trap density and trap depth. These values for polymers is reported to have $10^{-10} \sim 10^{-6}$[18]. This consideration predicts the trap-limited mobility between $5x10^{-15}$ and $5x10^{-19}$ m^2/Vs. These values are reasonable compared to other reported values for the trap-limited mobility[19, 20]. In our simulation the trap-limited mobility will range from $5x10^{-14}$ and $5x10^{-17}$ m^2/Vs. These parameters will be employed to describe electronic breakdown and thermal breakdown process for AF45 glass samples under dc stress of 100 V/s voltage ramp rate at several temperatures.

Table 5-3 Parameters in the simulation of breakdown strengths for AF45 glass.

Parameters	Value	Unit
Barrier height for injection(w_{ei})	0.9	eV
Electron mobility	$5.0x10^{-14}$~$5.0x10^{-17}$	$m^2V^{-1}s^{-1}$
Permittivity	6.0	
Volumetric heat capacity	$1.84x10^6$	J/m^3K
Thermal conductivity	1.11	W/mK
Voltage ramp rate	100	V/s

5.4.1.2. Simulation results for breakdown strengths of AF45 glasses

5.4.1.2.1. Effects of trap-limited mobility on breakdown strengths of 50 μm AF45 glasses

The trap-limited mobility is difficult to determine experimentally and a range of values are assumed in the simulation. This mobility significantly affects the breakdown strength and therefore its effects on breakdown strength are studied. Figure 5-7 shows modeling results of electron charge density for 50 μm AF45 glasses using 4 different electron mobilities. As the electron mobility decreases the charge density near the cathode increases. In the figure zero and 50 in the position indicate cathode and anode. When the electron mobility is $5.0x10^{-17}$ m^2/Vs electrons don't arrive in the anode even in the breakdown event. Figure 5-8 shows the electric field distribution until dielectric breakdown for 50 μm AF45 glasses using different electron mobilities. When electron mobilities are larger than $5x10^{-16}$ m^2/Vs the electron charge density is distributed through the glass. Then the electric field is distorted throughout the glass according to the Poisson's relationship. However, when the electric mobility is $5x10^{-17}$ m^2/Vs electron charge density is limited below about 20 μm from the cathode. The electric field is also distorted through this range and above the region the electric field is uniform.

The breakdown strength is calculated using the above electron mobilities for 50 μm AF45 glasses. Figure 5-9 shows the modeling results and all breakdown events are governed by electronic breakdown mechanism since the electric field reached the intrinsic breakdown strength of 1160 MV/m. The temperature rise was within 1 ^oC for all electron mobility conditions. When the electron mobility is larger than $5x10^{-16}$ m^2/Vs the breakdown strength are between 777 and 801 MV/m. When the electron mobility is $5x10^{-17}$ m^2/Vs the calculated breakdown strength was 1044 MV/m.

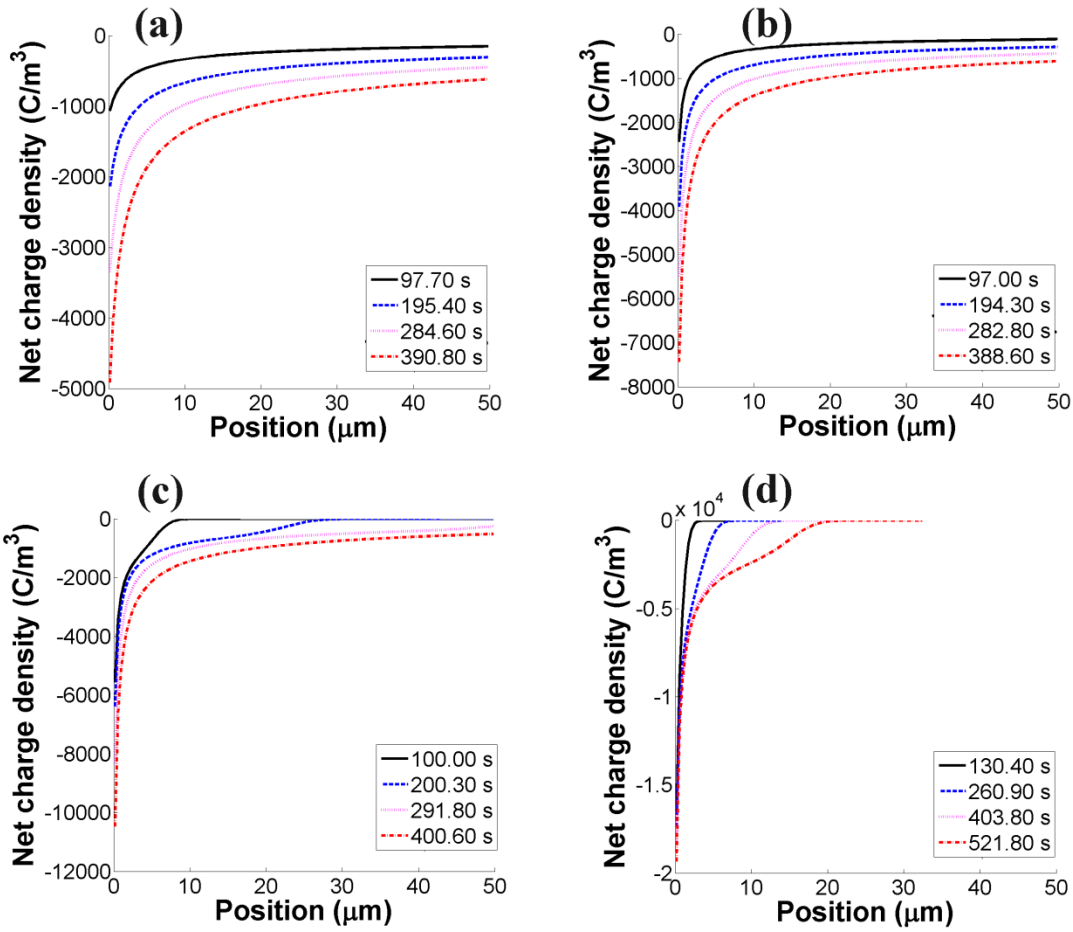

Figure 5-7 Modeling results of electron charge density(Net charge density) for 50 μm AF45 glasses with different electron mobility; (a) $5.0x10^{-14}$ m^2/Vs (b) $5.0x10^{-15}$ m^2/Vs (c) $5.0x10^{-16}$ m^2/Vs (d) $5.0x10^{-17}$ m^2/Vs

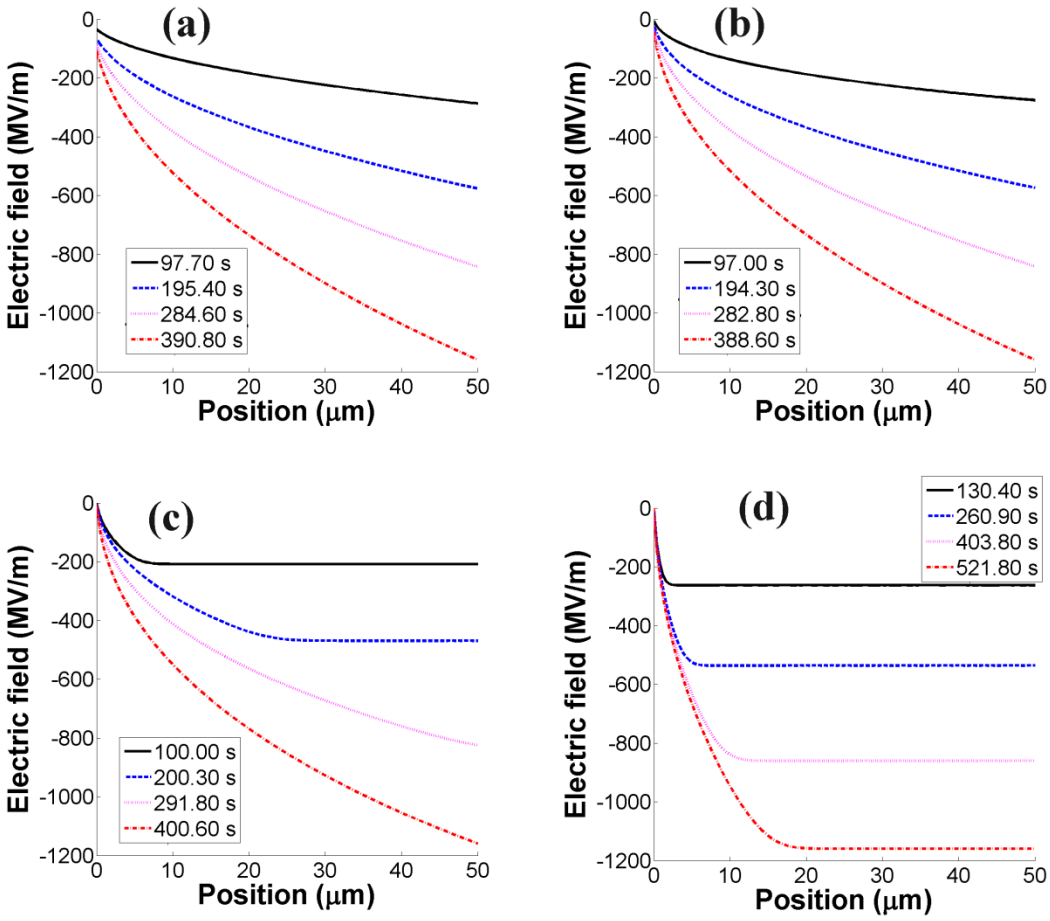

Figure 5-8 Modeling results of electric fields for 50 μm AF45 glasses with different electron mobility; (a) 5.0×10^{-14} m^2/Vs (b) 5.0×10^{-15} m^2/Vs (c) 5.0×10^{-16} m^2/Vs (d) 5.0×10^{-17} m^2/Vs

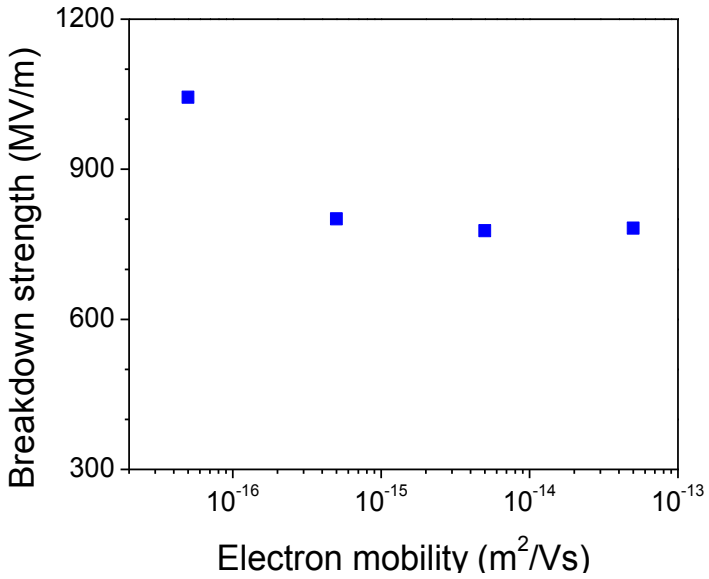

Figure 5-9 Theoretical breakdown strengths for 50 μm AF45 glasses using different electron mobilities.

5.4.1.2.2. Effects of glass thickness on breakdown strengths of AF45 glasses

Glass thickness affects the breakdown strength of dielectric materials. The effect is important in a fundamental point of view as well as a practical point of view. So the effect of glass thickness on breakdown strength for AF45 glasses is modeled using 100 V/s of ramp rate at room temperature as shown in Figure 5-10. Experimental results show that the breakdown strength is constant for thicknesses below about 20 μm and then decreases above the thickness. Meanwhile, the modeling results show that the breakdown strength is constant within the thickness range under given test conditions and cannot predict strong thickness dependence below 20 μm.

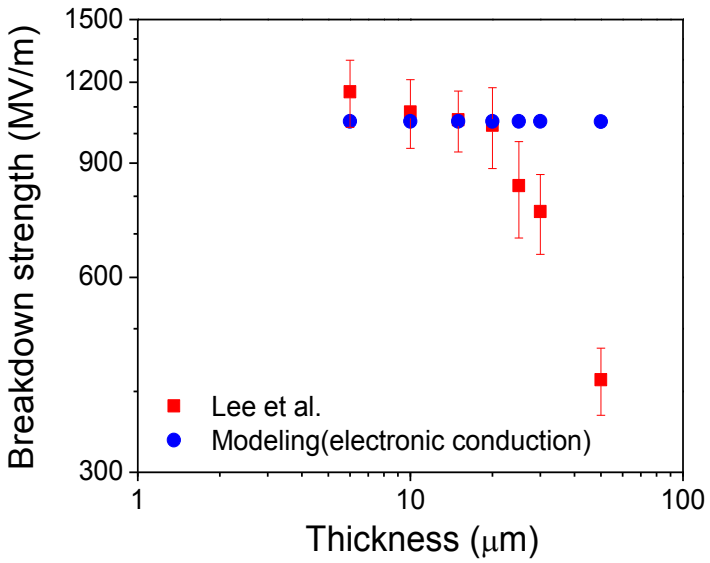

Figure 5-10 Comparison of breakdown strength for AF45 glasses at room temperature from experiments and modeling assuming electronic conduction[2].

5.4.2. Numerical model assuming ionic redistribution and electronic breakdown

5.4.2.1. Theoretical background for the breakdown model assuming ionic redistribution and electronic breakdown

It has been known that the electronic breakdown may be influenced by ionic space charges in ion-conducting materials such as KBr at high temperature[11]. As discussed in Chapter 4 ionic space charges are created under the anode when high electric field is applied to low-alkali BAS. In these glasses even at room temperature the formation of ionic space charges (depletion regions) is experimentally observed using optical second-order nonlinearity measurement if electric field higher than half the breakdown strengths is applied. Then it is possible that the electronic breakdown is initiated from local electric field enhancement within depletion region for low-alkali BAS. Therefore breakdown model assuming ionic redistribution and electronic breakdown will be discussed below.

Thermal breakdown occurs from Joule heating by conduction current. Considering that the thickness is much smaller than the width and breadth of the sample, a one-dimensional problem can be assumed for thermal breakdown. For one-dimensional case thermal breakdown can be described by Eqn. (5-4) as discussed in Chapter 5.4.1.1. At the breakdown criterion, thermal breakdown occurs when a local temperature in the dielectric attains the melting temperature of the glass.

Electronic breakdown can occur from space charge formation induced from ionic conduction. In this breakdown model, it is assumed that mobile cations such as Na^+, H^+/H_3O^+, and Ba^{2+} can produce depletion region and space charge within BAS glass where its electric field enhancement can initiate the breakdown. For breakdown criterion, it occurs when local electric field within the glass reaches intrinsic breakdown strength of glass. The intrinsic breakdown strength of glass is determined based on the literature and set to 1160 MV/m[2].

Then the theoretical breakdown field based on ionic redistribution and electronic breakdown can be determined if the electric field and the temperature in the insulator is numerically calculated for each time and each position. For every time step, the local temperature is compared with the melting point and the local electric field is compared with intrinsic breakdown strength. Dielectric breakdown occurs when either of the two criteria is reached. Both electric field and temperature can be evaluated from ion transport through Poisson's equation and Joule heating.

The ionic charge transport with three charge carriers (Na^+, H^+/H_3O^+, Ba^{2+}) will be used for the breakdown modeling which is also used to predict the depletion with in low-alkali BAS in Chapter 4. There are several assumptions for this model to apply the breakdown of low-alkali BAS.

(1) It is assumed that a BAS sample is located at x=0 and x=d and the problem is one dimensional.

(2) Three kinds of mobile charge carriers are present in the glass; sodium ions, barium ions and H_3O^+/H^+ ions. It is also assumed that initially there are no H_3O^+/H^+ ions in the glass which are injected from the anode with rate of σ_2. The ratio between H_3O^+/H^+ ions mobility to sodium mobility is 10^{-2}. The mobility of Ba^{2+} is set to be $1.0\text{x}10^{-21}$ $m^2V^{-1}s^{-1}$ based on Table 4-6.

(3) Non-blocking electrode condition is present at the anode and cathode. So charge carriers can be neutralized at the electrode.

(4) Sodium, barium and H_3O^+/H^+ ions can move under the applied electric field (E). Then the current density can be given by

$$j_i = \mu_i e p_i E \tag{5-10}$$

where the index i denotes one of the positive ionic species (1 is sodium ion, 2 is proton and 3 is barium ion). Current density from diffusion is ignored in this equation.

The electric field distribution and charge distribution in low-alkali BAS during breakdown can be described by Eqn. (5-10), the local equation of continuity, and Poisson's equation below

$$\frac{\partial p_i}{\partial t} = -\frac{\partial j_i}{\partial x} \tag{5-11}$$

$$\frac{\partial E}{\partial x} = \frac{e}{\varepsilon}\sum_i (p_i - p_{0,i}) \tag{5-12}$$

where p_i is the concentration for positive ions, $p_{0,i}$ the initial concentration for positive ions, j_i the current density for positive ions, e the elementary charge, ε the permittivity, respectively. As an initial condition, it is assumed that mobile sodium and barium ions are uniformly distributed in low-alkali BAS glass. These concentrations are calculated from weak electrolyte theory for glass in chapter 4.7.1. It is further assumed that high electric field can increase the mobile ionic concentration according to the Onsager theory[21, 22]. The Onsager theory shows that the ratio of high field ionic concentration (c) and low field ionic concentration (c_0) can be described by

$$\frac{c}{c_0} = 1 + \frac{b}{2} + \frac{b^2}{24}$$

$$b = \frac{963.6E}{\varepsilon T^2} \tag{5-13}$$

where E is the electric field, ε the relative permittivity of glass, T the temperature. The mobile sodium and barium concentration at high electric field then can be calculated from the weak electrolyte theory and the Onsager theory at different temperatures. These concentrations of mobile sodium ions are summarized in Table 5-4.

Table 5-4 Concentrations of mobile sodium ions as a function of temperature at low electric field and high electric field estimated from the weak electrolyte theory and the Onsager theory respectively.

Temperature	Sodium ion concentration at low field from weak electrolyte theory	Sodium ion concentration at high field from Onsager theory
K	Ions/m^3	Ions/m^3
298	$1.32x10^{20}$	$9.77x10^{21}$
373	$1.25x10^{21}$	$4.38x10^{22}$
423	$3.58x10^{21}$	$8.23x10^{22}$
473	$8.23x10^{21}$	$1.40x10^{23}$
573	$2.81x10^{22}$	$2.78x10^{23}$
673	$6.67x10^{22}$	$4.40x10^{23}$

To solve the coupled problem of Eqn. (5-4), (5-10), (5-11), and (5-12) for our breakdown model, several numerical techniques are utilized. The electric field and potential in the glass are evaluated using finite difference method (FDM) through direct discretization of Eqn. (5-12) as shown in Figure 5-11. The modeled glass sample is divided into m slices and the electric field difference at each cell associated with the net charge density can be calculated with the boundary condition. The continuity equation, Eqn. (5-11), can be evaluated using upwind scheme. The time step in the calculation is selected based on the condition of Courant-Friedrichs-Lewy (CFL) which is necessary for the stability of the numerical technique. The power balance equation, Eqn. (5-4), can be calculated using the FDM with the backward Euler method in time and the forward Euler method in spatial coordinate. The backward Euler method in time is applied due to its superior numerical stability regardless of the time step although the computation is much rigorous.

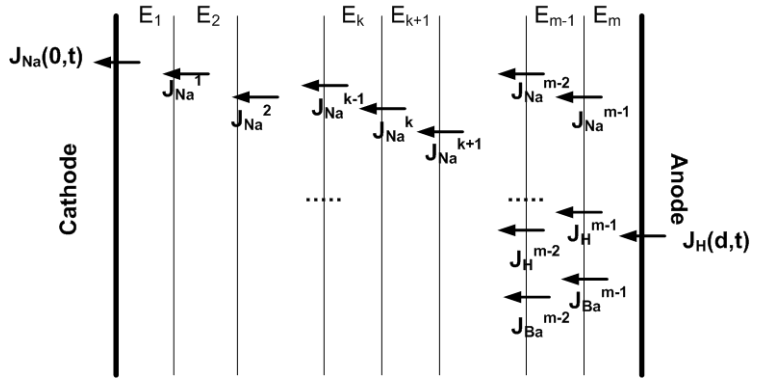

Figure 5-11 Discretization of glass dielectric for breakdown modeling assuming ionic redistribution and electronic breakdown.

5.4.2.2. Simulation results for breakdown strengths of low-alkali BAS glasses

5.4.2.2.1. Effects of glass thickness on breakdown strengths of AF45 glasses

In Chapter 5.4.1.1 the thickness dependence of breakdown strengths in AF45 glass was modeled assuming electronic conduction. It could predict only thickness independent region. On the other hand, experimentally determined breakdown strengths showed two different regimes; weakly thickness dependent region below 20 μm and strongly thickness dependent region above 20 μm. So it is interesting to apply the numerical model assuming ionic redistribution and electronic breakdown to thickness dependence of AF45 glass at room temperature.

Numerical model assuming ionic redistribution and electronic breakdown developed in Chapter 5.4.2.1 was used along with modeling parameters summarized in Table 5-5. The thickness of AF45 glass ranged from 5 to 50 μm. Figure 5-12 shows mobile sodium ion concentration profiles for AF45 glass with different thicknesses during breakdown tests at room temperature. In the figure position '0' designates the cathode side. Below 20 μm of thickness mobile sodium ions were fully depleted at the time of breakdown events. However, above 20 μm mobile sodium ions were partially depleted from the anode side and there were still mobile sodium ions near the cathode side. These mobile sodium ions profiles affect net charge density profiles as shown in Figure 5-13. Although net charge densities consist of sodium ions, H^+/H_3O^+, and barium ions it is mostly determined by mobile sodium concentrations due to relatively low mobility of other ions (In fact H^+/H_3O^+ and barium ions affect the net charge density only at regions close to the anode as shown in Figure 5-13). Then since mobile sodium ions were fully depleted for AF45 glasses with thicknesses below 20 μm the net negative charge densities were uniformly distributed at the time of breakdown events. Meanwhile for AF45 glasses with thickness above 20 μm the net negatives charges were confined within depletion region close to the anode side. These net charge densities determine electric field distributions from Eqn. (5-12).

Table 5-5 Modeling parameters for breakdown strengths of AF45 glass assuming ionic redistribution and electronic breakdown at room temperature.

	AF45
Sodium mobility ($m^2V^{-1}s^{-1}$)	$4.0x10^{-16}$
H_3O^+/H^+ mobility ($m^2V^{-1}s^{-1}$)	$4.0x10^{-18}$
Barium mobility ($m^2V^{-1}s^{-1}$)	$1.0x10^{-21}$
Initial sodium concentration (atoms/m^3)	$9.77x10^{21}$
Initial H_3O^+/H^+ concentration (atoms/m^3)	0
Initial barium concentration (atoms/m^3)	$3.74x10^{13}$
σ_2 ($m^{-2}V^{-1}s^{-1}$)	$5.0x10^{11}$
Voltage ramp rate (V/s)	100
Volumetric heat capacity (J/m^3K)	$1.84x10^6$
Thermal conductivity (W/mK)	1.11
Melting temperature (K)	1156
Intrinsic breakdown strength (V/m)	$1160x10^6$

Figure 5-14 shows electric field distributions for AF45 glass with different thicknesses during breakdown tests at room temperature. For AF45 glass with thickness below 20 μm the magnitude of electric field linearly increases towards the anode. However, for AF45 glass with thicknesses above 20 μm electric fields were enhanced within the depletion regions which could decrease the breakdown strengths. It is noteworthy that there is local electric maximum at bulk side near the anode which results mostly from proton injection as shown in Figure 5-14.

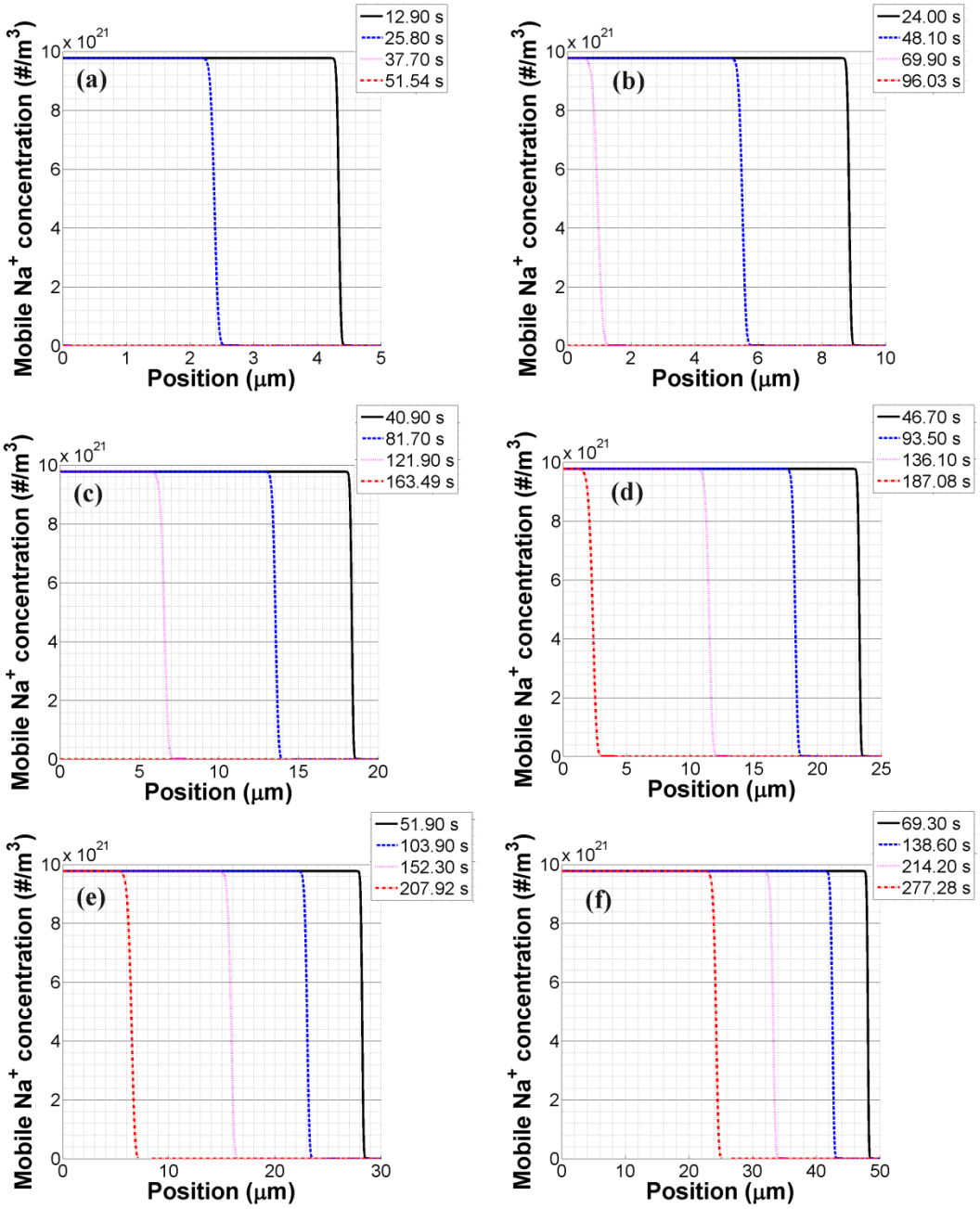

Figure 5-12 Mobile sodium concentration profiles for AF45 glass during breakdown tests at room temperature; (a) 5 μm, (b) 10 μm, (c) 20 μm, (d) 25 μm, (e) 30 μm, (f) 50 μm.

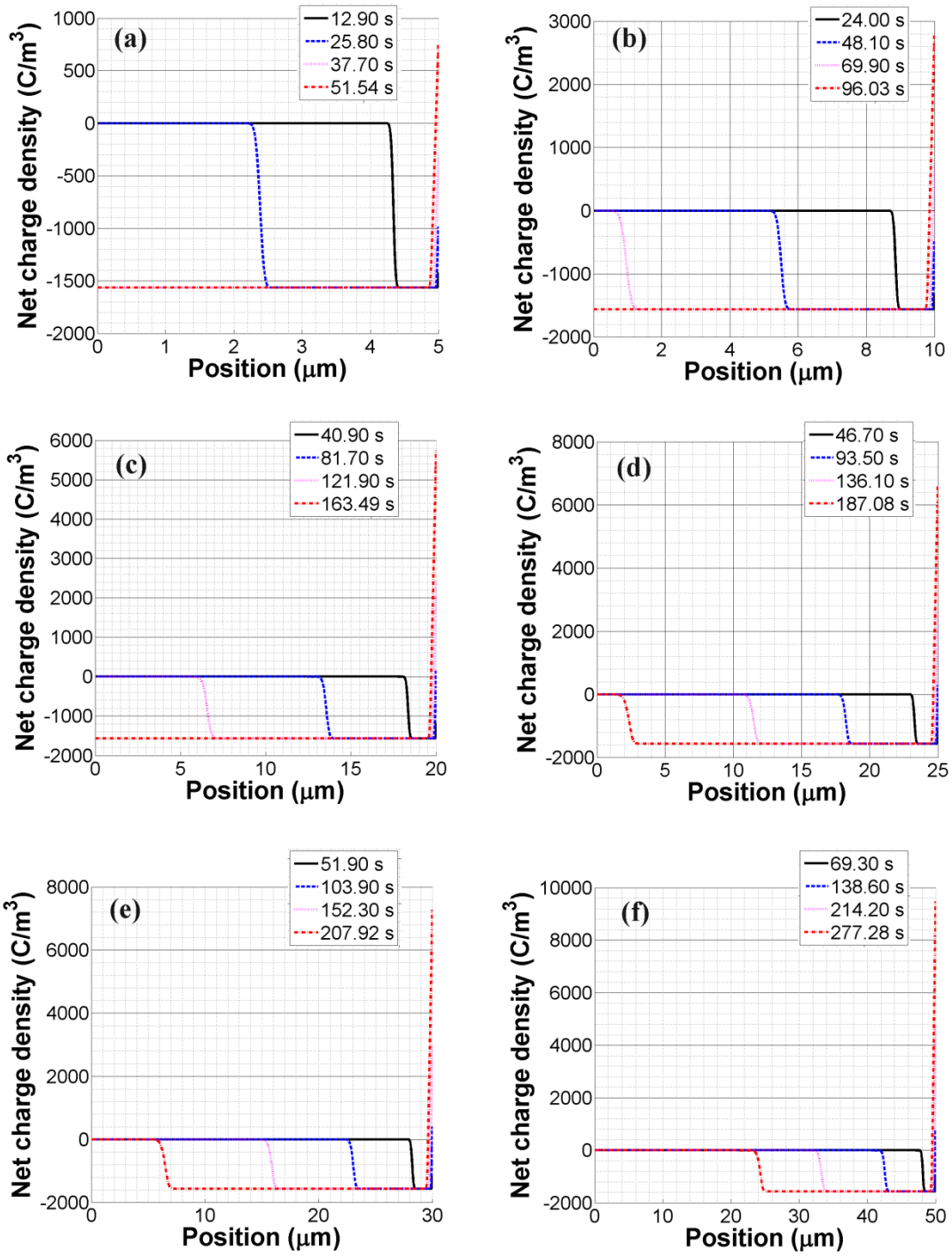

Figure 5-13 Net charge density profiles for AF45 glass during breakdown tests at room temperature; (a) 5 μm, (b) 10 μm, (c) 20 μm, (d) 25 μm, (e) 30 μm, (f) 50 μm.

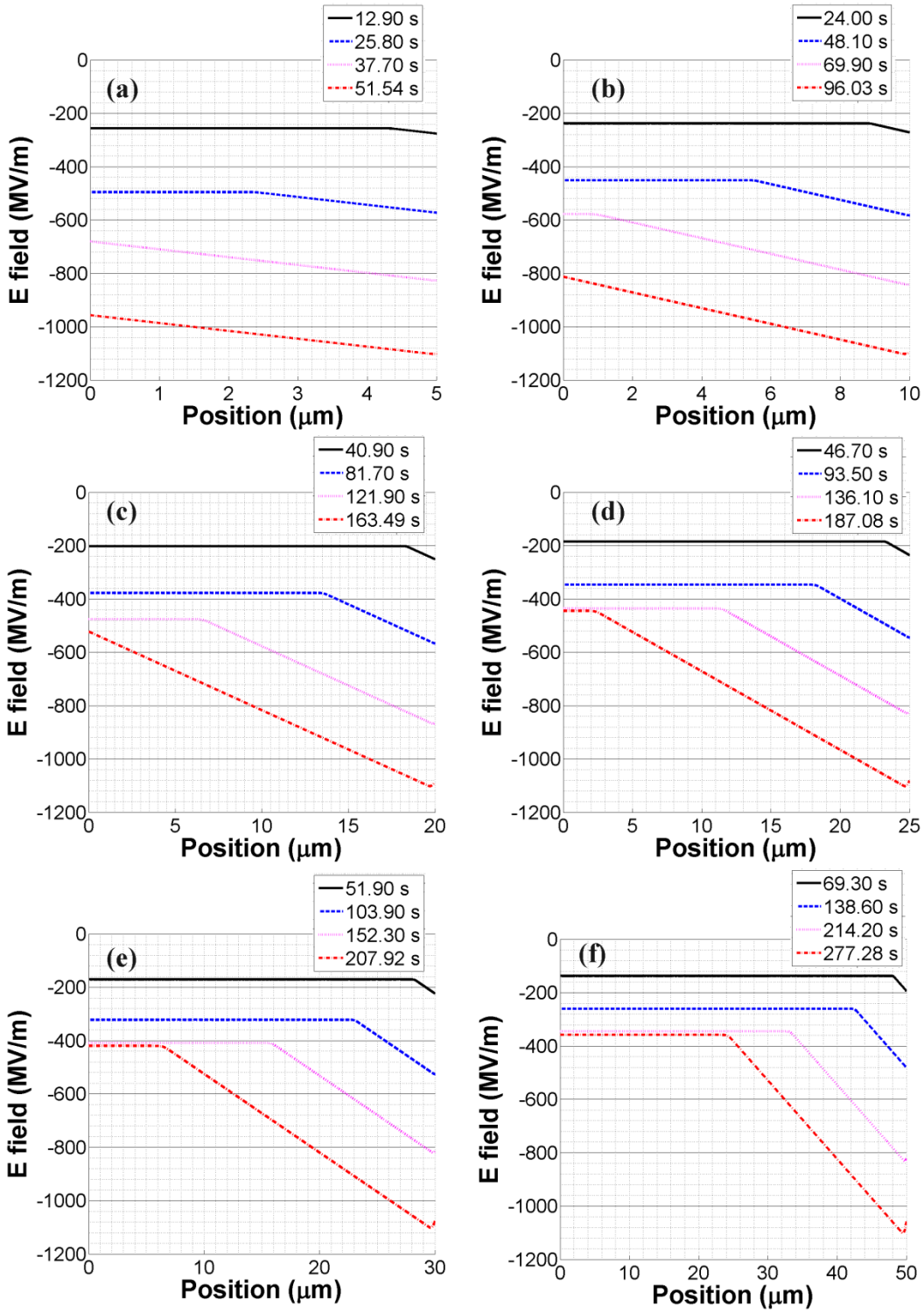

Figure 5-14 Electric field profiles for AF45 glass during breakdown tests at room temperature; (a) 5 μm, (b) 10 μm, (c) 20 μm, (d) 25 μm, (e) 30 μm, (f) 50 μm.

So Figure 5-15 summarized the effect of thickness on breakdown strength for AF45 glasses using 100 V/s of ramp rate at room temperature. The breakdown strengths show two distinct regions similar to experimental results; weakly thickness dependent below 20 μm and strongly thickness dependent region above 20 μm. These two different regions can be explained by the formation of depletion regions. The glasses with thicknesses below 20 μm were fully depleted of mobile sodium ions at the time of breakdown. However the glasses with thicknesses above 20 μm were partially depleted at regions close to the anode and these results in the local electric field enhancement within depletion regions. Then the breakdown strengths for AF45 glass are strongly thickness dependent in the case of thicknesses above 20 μm.

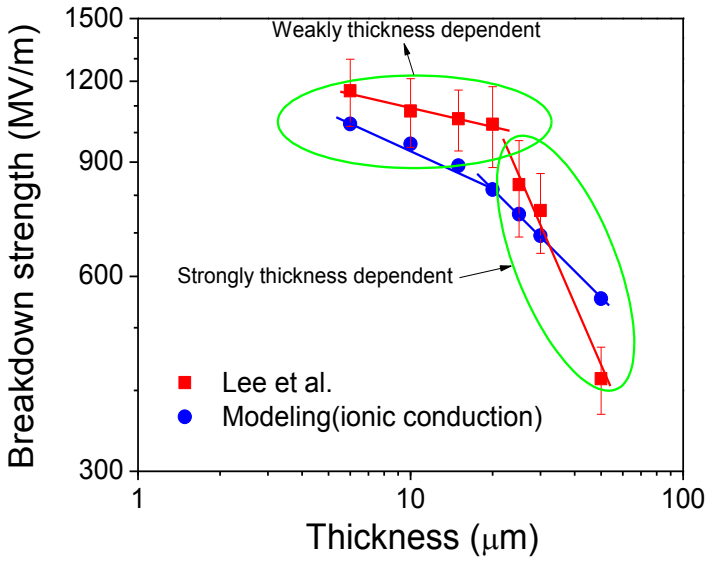

Figure 5-15 Comparison of breakdown strength for AF45 glasses at room temperature from experiments and modeling assuming ionic redistribution and electronic breakdown[2].

5.4.2.2.2. Effects of temperature on breakdown strengths of AF45 glasses

Temperature dependence of breakdown strengths for AF45 glass is also studied using the numerical model assuming ionic redistribution and electronic breakdown. Modeling parameters in Table 5-5 except concentration of mobile ions and voltage ramp rate are used. Voltage ramp rate is 500 V/s for this modeling. The concentrations of mobile sodium and barium ions at different temperatures are estimated using weak electrolyte theory and Onsager theory as discussed in Chapter 5.4.2.1 as shown in Table 5-6. Figure 5-16 shows comparison of breakdown strengths for 15 μm AF45 glass between experiments and modeling. For 15 μm thickness modeling results can predict a decreasing tendency of breakdown strengths with temperature taking into account of experimental errors. For 50 μm thickness modeling results can also predict the decreasing tendency between 100 and 150 ^{o}C although there is a large discrepancy of breakdown strengths at room temperature as shown in Figure 5-17. This relatively higher breakdown strength for 50 μm AF45 glass at room temperature may come from electronic contribution to breakdown. Dash showed electron injection from high field thermally stimulated depolarization current study for 50 μm AF45 glass[23]. Due to high electric field within a depletion layer electron can be injected which can increase negative space charge in the layer. This increased negative space charge can result in decrease in breakdown strengths for 50 μm AF45 glass.

Table 5-6 Concentrations of initial mobile sodium and barium ions estimated from weak electrolyte theory and Onsager theory.

Temperature	Initial sodium ion concentration	Initial barium ion concentration
K	Ions/m^3	Ions/m^3
298	$9.77x10^{21}$	$3.74x10^{13}$
373	$4.38x10^{22}$	$1.99x10^{16}$
423	$8.23x10^{22}$	$3.54x10^{17}$

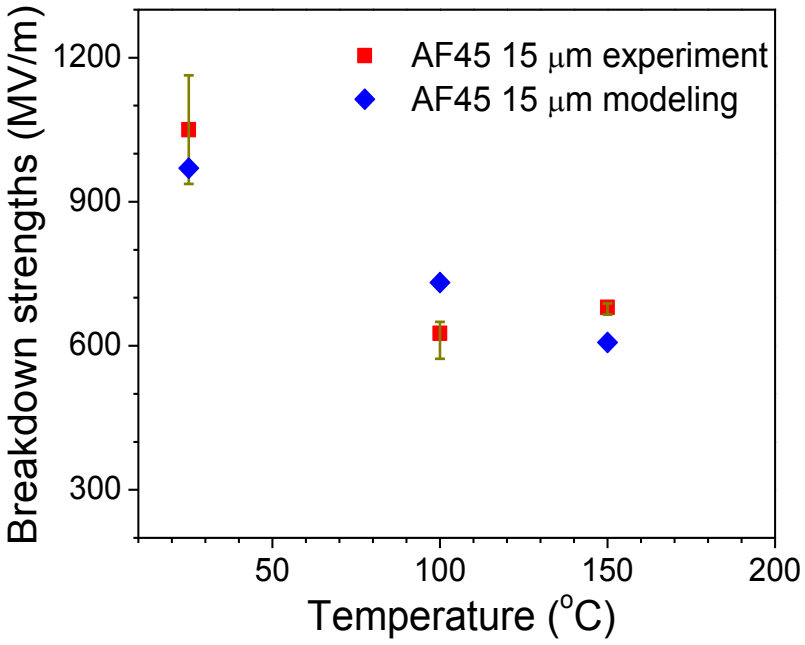

Figure 5-16 Comparison of breakdown strengths for AF45 glass with thickness of 15 μm between experiment and modeling.

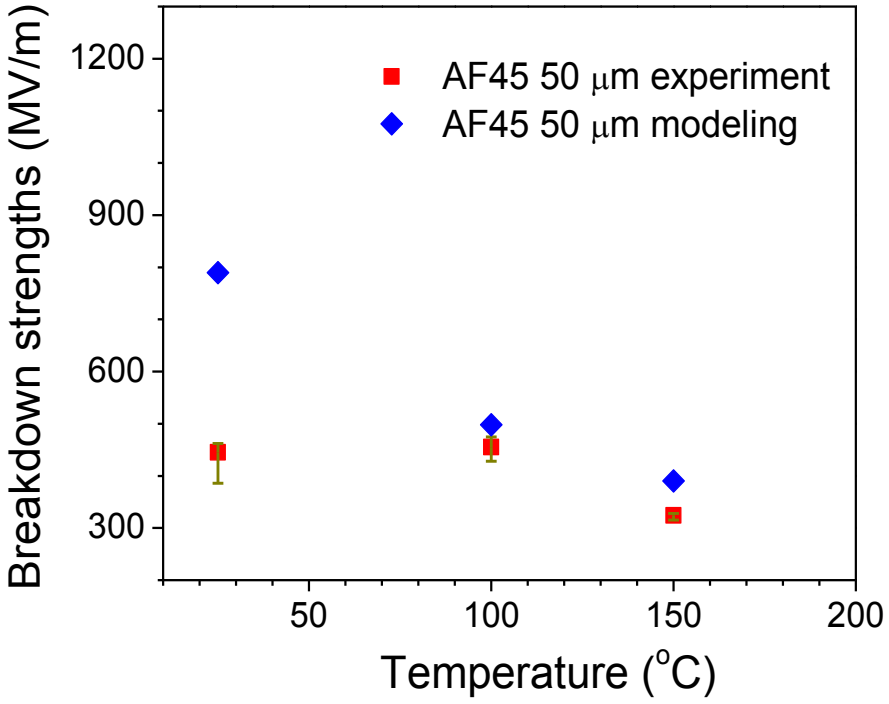

Figure 5-17 Comparison of breakdown strengths for AF45 glass with thickness of 50 μm between experiment and modeling.

5.5. Conclusions

Numerical models are applied to breakdown strengths of low-alkali BAS glass. The model assuming electronic conduction predicted thickness independent breakdown strengths below 20 μm for AF45 glass. However, this model could not predict thickness dependent breakdown strengths above 20 μm. Numerical model assuming ionic redistribution and electronic breakdown predicted two distinct regions in AF45 glass for thickness dependence of breakdown strengths. Interestingly temperature dependence of breakdown strengths for AF45 glass predicted by the latter model agreed well with experimental results. This model showed that the change in breakdown strengths with temperature mostly depended on the initial mobile sodium concentration.

5.6. References

1. Smith, N.J., et al., *Alkali-free glass as a high energy density dielectric material.* Materials Letters, 2009. **63**(15): p. 1245-1248.
2. Lee, H., et al., *Dielectric Breakdown of Thinned $BaO–Al_2O_3–B_2O_3–SiO_2$ Glass.* Journal of the American Ceramic Society, 2010. **93**(8): p. 2346-2351.
3. Murata, T., et al., *Electrode-Limited Dielectric Breakdown of Alkali Free Glass.* Journal of the American Ceramic Society, 2012.
4. Vermeer, J., *The impulse breakdown strength of pyrex glass.* Physica, 1954. **20**(1): p. 313-326.
5. Von Hippel, A. and R. Maurer, *Electric breakdown of glasses and crystals as a function of temperature.* Physical Review, 1941. **59**(10): p. 820.
6. Smith, N.J., *Novel Approaches to the Surface Modification of Glass by Thermo-electric Poling*. 2011, Pennsylvania State University.
7. Optics, U. *Schott AF45*. [cited 2013 8/22]; Available from: http://www.uqgoptics.com/materials_commercial_schott_AF45.aspx.

8. Murata, T., et al. *Ultra thin glass roll for flexible AMOLED display*. in *International Display Workshops*. 2011. Nagoya.
9. Fukuma, M., M. Nagao, and M. Kosaki. *Numerical analysis of dielectric breakdown in polypropylene film based on thermal and electronic composite breakdown model*. in *Properties and Applications of Dielectric Materials, 1991., Proceedings of the 3rd International Conference on*. 1991: IEEE.
10. Zebouchi, N., T. Hoang, and B. Ai, *Thermoelectronic breakdown with pressure and space charge effects in polyethylene.* Journal of Applied Physics, 1997. **81**(5): p. 2363-2369.
11. O'Dwyer, J.J., *The theory of electrical conduction and breakdown in solid dielectrics*. 1973: Clarendon Press Oxford.
12. Chen, G. and J. Zhao, *Observation of negative differential mobility and charge packet in polyethylene.* Journal of Physics D: Applied Physics, 2011. **44**(21): p. 212001.
13. Chen, G., et al., *Origin of thickness dependent dc electrical breakdown in dielectrics.* Applied Physics Letters, 2012. **100**(22): p. 222904-222904-4.
14. Zhao, J., G. Chen, and P. Lewin, *Investigation into the formation of charge packets in polyethylene: Experiment and simulation.* Journal of Applied Physics, 2012. **112**(3): p. 034116-034116-6.
15. Le Roy, S., G. Teyssedre, and C. Laurent, *Charge transport and dissipative processes in insulating polymers: experiments and model.* Dielectrics and Electrical Insulation, IEEE Transactions on, 2005. **12**(4): p. 644-654.
16. Le Roy, S., et al., *Description of charge transport in polyethylene using a fluid model with a constant mobility: fitting model and experiments.* Journal of Physics D: Applied Physics, 2006. **39**(7): p. 1427.
17. Nelson, R., *Electronic Conduction in Glass.* Journal of Applied Physics, 1963. **34**(3): p. 629-631.
18. Dissado, L.A. and J.C. Fothergill, *Electrical degradation and breakdown in polymers*. Vol. 9. 1992: Peter Peregrinus Ltd.
19. Frank, R. and J. Simmons, *Space-Charge Effects on Emission-Limited Current Flow in Insulators.* Journal of Applied Physics, 1967. **38**(2): p. 832-840.
20. Schug, J.C., A. Lilly Jr, and D. Lowitz, *Schottky currents in dielectric films.* Physical Review B, 1970. **1**(12): p. 4811.
21. Onsager, L., *Deviations from Ohm's law in weak electrolytes.* The Journal of Chemical Physics, 1934. **2**: p. 599.
22. Ingram, M., C.T. Moynihan, and A. Lesikar, *Ionic conductivity and the weak electrolyte theory of glass.* Journal of Non-Crystalline Solids, 1980. **38**: p. 371-376.
23. Dash, P., *Dynamics of Space Charge Polarization and Electrical Conduction in Low Alkali Boroaluminosilicate glasses*, in *Engineering Science and Mechanics*. 2013, The Pennsylvania State University: University Park.

Chapter 6: Combined Electronic and Thermal Breakdown Models for Polyethylene

6.1. Introduction

Dielectric breakdown and degradation of polymer insulators under high electric field have been important in practical applications such as power cables and power capacitors. The breakdown processes have been explained by several breakdown mechanisms including electronic, thermal, electromechanical breakdown, and partial discharges[1-5]. These mechanisms assume no space charge distribution and therefore electric field is uniform throughout the entire material.

Effects of space charge on high electric field conduction have been understood through space-charge-limited current where space charge distorts the local electric field in the insulator and affect current density[6-8]. Dependence of dielectric breakdown on space charge has also been reported by dc pre-stress experiments[9, 10]. Moreover, advances in nondestructive measurement techniques such as laser-induced pressure pulse (LIPP), pulsed electro-acoustic (PEA), and thermal pulse methods has made the direct measurement of space charge under high electric field possible[11, 12]. Space charge from charge injection and transport in low-density polyethylene(LDPE) was observed through the PEA method and analyzed with a trapping/detrapping behaviors of charge carriers[13]. Space charge development under thermal poling at 150 ^{o}C in a soda-lime glass was also reported from the LIPP method[14]. Therefore, the breakdown mechanisms should be modified to accommodate space charge effects.

A theoretical breakdown model with space charge effects was first proposed by Fukuma et al. for polypropylene[15]. This model assumed electron injection at the cathode through

Schottky mechanism and charge transport by hopping conduction mechanism through the bulk of the polymer film. Space charge effects on electric field distribution and charge transport were applied by Poisson's equation. This model predicted not only electronic breakdown but also thermal breakdown. Thermal breakdown was expected when elevated local temperature from Joule heating exceeded melting temperature of polypropylene before electric field reached intrinsic breakdown strength. A similar model was applied to LDPE where pressure effects on breakdown strength were also investigated[16]. Although these models have provided successful agreement with experiments, Richardson constant among model parameters showed unrealistically low values of 0.1 $Am^{-2}K^{-2}$. Recently bipolar charge transport model was proposed for LDPE and their modeling of charge profile and electric field distribution showed good agreement with experiments[17-19]. Bipolar charge transport model assuming constant mobility was also applied to electronic breakdown of LDPE and used to explain thickness dependence of breakdown strength at room temperature[20].

The aim of this chapter is to develop combined thermal and electronic breakdown models based on bipolar charge transport and charge injection. For the mobility of charge carriers two kinds of mobility will be addressed including constant mobility, and hopping mobility. This model provides not only a prediction of the breakdown strength but also field, time and temperature effects on the space charge dynamics and the resultant electric field evolution during breakdown process.

6.2. Breakdown model based on charge transport

6.2.1. Model description

Electronic breakdown is initiated by the local electric field enhancement from space charge formation and thermal breakdown occurs from Joule heating by a transient conduction current. Thermal breakdown is explained by the following power balance equation

$$C_v \frac{\partial T}{\partial t} - \mathrm{div}(\kappa \nabla T) = JE \tag{6-1}$$

where T is the local temperature, t the time, C_v the volumetric heat capacity, κ the thermal conductivity, J the transient current density, and E the local electric field. At the breakdown criterion, thermal breakdown occurs when a local temperature in the dielectric attains the melting temperature of LDPE. For impulse thermal breakdown, thermal conduction is ignored, and this assumption has often been used to model breakdown process in the polymer due to the simple mathematical relationship[15, 16]. However, impulse thermal breakdown is only valid if the time to breakdown is smaller than thermal relaxation time[21]. For a LDPE with thickness of 25 μm the time to breakdown is about 30 seconds at 25 ^{o}C assuming 300 V/s of ramp rate. Meanwhile, the thermal relaxation time (τ_d) governed by

$$\tau_d = \frac{d^2 C_v}{4\kappa} \tag{6-2}$$

where d is the sample thickness shows about 1 milliseconds. The time to breakdown is much longer than the thermal relaxation time. Then thermal conduction cannot be ignored and assumption of impulse thermal breakdown is invalid in our case. Instead of impulse thermal breakdown Eqn. (6-1) is used to model thermal breakdown.

Considering that the thickness is much smaller than the width and breadth of the sample, a one-dimensional problem can be assumed for thermal breakdown. The governing equation for thermal breakdown reduces to

$$C_v \frac{\partial T}{\partial t} - \kappa \frac{\partial^2 T}{\partial x^2} = J(x,t)E(x,t) \quad (6\text{-}3)$$

where x is the distance from the cathode in the direction of thickness. It is assumed that the thermal conductivity is independent of temperature.

Charge injection and space charge formation in dielectric materials are closely related with the electronic breakdown. Space charge dynamics plays an important part in breakdown process because it governs the local electric field. It has been experimentally demonstrated that under high dc electric field the charge injection and space charge formation occurs in polyethylene[13, 22-24]. In our breakdown model, it is assumed that injected charges from electrodes produce space charge within bulk and its electric field enhancement determines the breakdown. For breakdown criterion, it occurs when local electric field within the bulk reaches intrinsic breakdown strength of polyethylene. The intrinsic breakdown strength of polyethylene is determined based on the literature and set to 680 MV/m[25].

The theoretical breakdown field based on electronic and thermal models can be determined if the electric field and the temperature in the insulator is numerically calculated for each time and each position. For every time step, the local temperature is compared with the melting point and the local electric field is compared with intrinsic breakdown strength. Dielectric breakdown occurs when either of the two criteria is reached. Both electric field and temperature can be evaluated from charge injection and charge transport through Poisson's equation and Joule heating.

6.2.2. Bipolar charge transport model based on constant mobility

In this model, the charge generation and transport are described by injection, transport, trapping and recombination of bipolar charges (electrons and holes) based on the scheme of Figure 6-1. This model is widely used to predict space charge evolution in polyethylene[18, 19].

Charge carriers are injected at the interface of electrode/dielectric according to the Schottky process. Two kinds of carriers can be either trapped or mobile. Under an externally applied electric field, a mobile electron in the conduction band (hole in the valence band) drift with an effective mobility which account for the plausible trapping and detrapping in shallow traps. Deep trapping is described through a single level of traps for each type of carrier which is assumed to remain without detrapping. The recombination process between the several electron-hole pairs are taken into account. After recombination, the carrier in the trap is released and thus trapping is

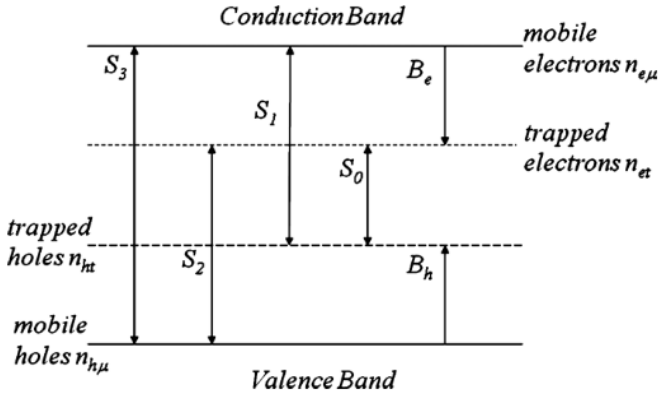

Figure 6-1 Illustration of trapping and recombination of bipolar charges.

feasible again. Initially no mobile charges are assumed within the dielectric. Dipolar polarization has been ignored considering the non-polar nature of polyethylene.

Assuming one-dimensional problem along the thickness, the current densities at the cathode (x=0) and the anode (x=d) from the Schottky mechanism is governed by

$$J_e(0,t) = AT^2 \exp\left(\frac{-w_{ei}}{k_B T}\right) \exp\left(\frac{e}{k_B T}\sqrt{\frac{eE(0,t)}{4\pi\varepsilon}}\right),$$

$$J_h(d,t) = AT^2 \exp\left(\frac{-w_{hi}}{k_B T}\right) \exp\left(\frac{e}{k_B T}\sqrt{\frac{eE(d,t)}{4\pi\varepsilon}}\right), \quad (6\text{-}4)$$

where $J_e(0,t)$ and $J_h(0,t)$ are the fluxes of electrons and holes at cathode and anode respectively, A the Richardson constant, T the temperature, k_B the Boltzmann constant, E(0,t) and E(d,t) the electric fields at the cathode and the anode, ε the permittivity of the dielectric, e the elementary charge, w_{ei} and w_{hi} the potential barriers for electrons and holes. Assuming no extraction barriers at electrodes, extraction current densities for electrons at the anode and holes at the cathode are described by

$$J_e(d,t) = \mu_e n_{em}(d,t)E(d,t),$$
$$J_h(0,t) = \mu_h n_{hm}(0,t)E(0,t), \quad (6\text{-}5)$$

where n_{em} and n_{hm} are charge densities for mobile electrons and holes, and μ_e and μ_h are the effective mobility for the electron and the hole.

The behavior of charge carriers within dielectrics as a function of time and distance are governed by three fundamental equations:

for Poisson's equation

$$\frac{\partial E(x,t)}{\partial x} = \frac{\rho(x,t)}{\epsilon}, \quad (6\text{-}6)$$

for transport equation

$$J(x,t) = \mu n(x,t)E(x,t), \quad (6\text{-}7)$$

for continuity equation

$$\frac{\partial n(x,t)}{\partial t} + \frac{\partial J(x,t)}{\partial x} = s, \quad (6\text{-}8)$$

where E is the electric field, ρ the net charge density, n the charge density for each carrier, and s the source term. The source term defines variations in local charge density due to trapping and recombination processes. For each charge type, mobile or trapped, the source term is described by

$$s_1 = -S_1 n_{ht} n_{em} - S_3 n_{hm} n_{em} - B_e n_{em}\left(1 - \frac{n_{et}}{N_{0et}}\right)$$
$$s_2 = -S_2 n_{et} n_{hm} - S_3 n_{hm} n_{em} - B_h n_{hm}\left(1 - \frac{n_{ht}}{N_{0ht}}\right)$$

$$s_3 = -S_2 n_{hm} n_{et} - S_0 n_{ht} n_{et} + B_e n_{em}\left(1 - \frac{n_{et}}{N_{0et}}\right)$$

$$s_4 = -S_1 n_{ht} n_{em} - S_0 n_{ht} n_{et} + B_h n_{hm}(1 - \frac{n_{ht}}{N_{0ht}}) \quad (6\text{-}9)$$

where s_1, s_2, s_3, and s_4 are the source term for mobile electrons, mobile holes, trapped electrons, and trapped holes; n_{em}, n_{et}, n_{hm}, and n_{ht} are the charge densities for mobile electrons, trapped electrons, mobile holes, and trapped holes; S_0, S_1, S_2, and S_3 are the recombination coefficients between four different electron-hole pairs; B_e and B_h are the trapping coefficients for electrons and holes; N_{0et} and N_{0ht} are the trap densities for electrons and holes.

6.2.3. Numerical techniques and application

To solve the coupled problem of Eqns. (6-3), (6-6), (6-7), and (6-8) for our breakdown model, several numerical techniques are utilized. The electric field and potential in the dielectric are evaluated using finite difference method (FDM) through direct discretization of Eqn. (6-6) as shown in Figure 6-3. The modeled LDPE sample is divided into m slices and the electric field difference at each cell associated with the net charge density can be calculated with the boundary condition. The continuity equation, Eqn. (6-8), can be evaluated using a splitting technique such that in a first step the continuity equation without the source term is calculated using upwind scheme and then in a second step the charge density is updated with the source term. The time step in the calculation is selected based on the condition of Courant-Friedrichs-Lewy which is necessary for the stability of the numerical technique. The power balance equation, Eqn. (6-3), can be calculated using the FDM with the backward Euler method in time and the forward Euler method in spatial coordinate. The backward Euler method in time is applied due to its superior numerical stability regardless of the time step although the computation is much rigorous.

Bipolar transport model with the constant mobility used to predict space charge dynamics, external current density, and electroluminescence in LDPE material has been supported by experimental measurements under various dc electric field conditions[18, 26, 27]. A set of model parameters, summarized in Table 6-1, is selected based on those works about bipolar transport model in LDPE material. Constant mobility for electrons and holes is assumed and the mobility of electrons is higher than that of holes. These parameters will be employed to describe electronic breakdown and thermal breakdown process for LDPE samples with thickness between 5 and 200 μm under dc stress from 100 to 500 V/s voltage ramp rate.

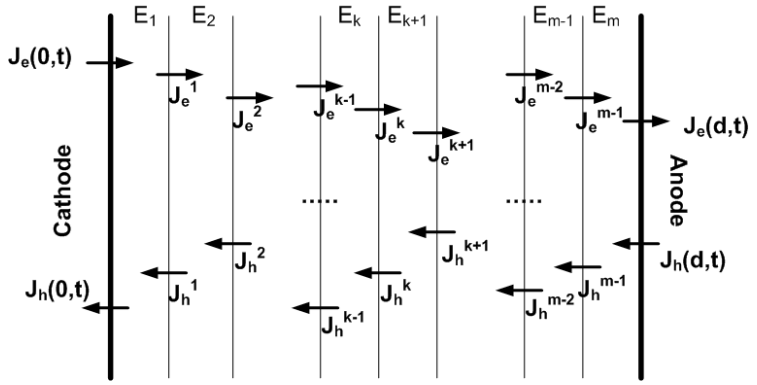

Figure 6-2 Discretization of modeled LDPE sample under breakdown tests.

Table 6-1 Parameters in the simulation of breakdown strength using constant mobility.

Parameters	Value	Unit
Barrier height for injection		
w_{ei}	1.15	eV
w_{hi}	1.14	eV
Mobility		
μ_e	9.0×10^{-15}	$m^2V^{-1}s^{-1}$
μ_h	1.5×10^{-16}	$m^2V^{-1}s^{-1}$
Trap density		
N_{0et}	100	Cm^{-3}
N_{0ht}	10	Cm^{-3}
Trapping coefficients		
B_e	7×10^{-3}	s^{-1}
B_h	7×10^{-5}	s^{-1}
Recombination coefficients		
S_0	4×10^{-3}	$m^3C^{-1}s^{-1}$
S_1	4×10^{-3}	$m^3C^{-1}s^{-1}$
S_2	4×10^{-3}	$m^3C^{-1}s^{-1}$
S_3	0	$m^3C^{-1}s^{-1}$

6.3. Simulation results

6.3.1. Space charge dynamics and electric field evolution from the constant mobility

Space charge dynamics and electric field evolution until the breakdown event can be estimated using our proposed model assuming the constant mobility. Figure 6-3(a) and 6-3(b) show local electric field distribution and net charge distribution at four different times during the voltage ramp (ramp rate of 300 V/s) for 25 μm thick LDPE sample. The fourth line at longest time shows electric field distribution and the net charge density when maximum local electric field within the sample reaches the intrinsic breakdown strength of 680 MV/m.

Figure 6-3(b) shows that negative charge has developed near the cathode and net positive charge has developed near the anode during the linear voltage rise. The magnitude of both charges increases with time, although negative charge has much smaller magnitude than that of

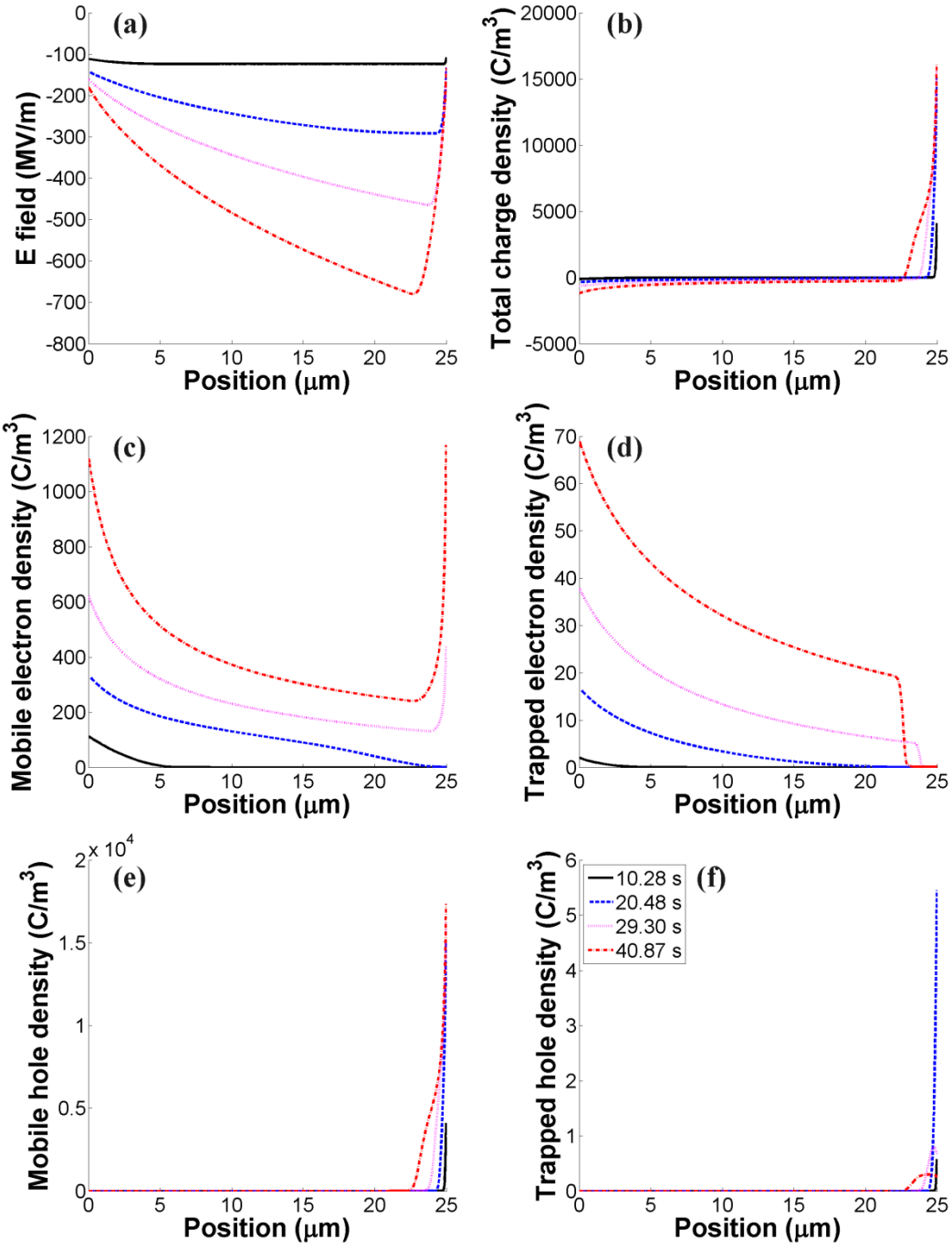

Figure 6-3 Modeling outputs from the constant mobility for 25 μm LDPE sample under 300 V/s until breakdown; (a) electric field (b) net charge density (c) mobile electron density (d) trapped electron density (e) mobile hole density (f) trapped hole density.

positive charge and is distributed over wider thickness region due to the higher electron mobility. The higher electron mobility also results in the arrival of electrons at the anode even at 20 s though holes don't transport to the cathode even at the breakdown as shown in Figure 6-3(c) and 6-3(e). Figure 6-3(d) and 6-3(f) show that trapped electrons are present over the entire region except next to the anode and trapped holes are present only near the anode. The latter is the result of the combination of the low mobility and the low trapping coefficient for holes.

Space charge also contributes the local electric field in addition to the applied electric field as shown in Figure 6-3(a). At about 10 s, near initial stage of the voltage rise, the applied field is not so high that the charge injection from electrodes is negligible. Therefore, the electric field contribution from space charge is very low and the resulting local electric field is almost uniformly given by the applied electric field. At about 20 s, the charge injection contributes the formation of space charge within the dielectric and also affects the local electric field. The maximum local electric field occurs near the anode. Higher electric field with increasing time results in more space charge and the local electric field distortion is more remarkable and the position of maximum local electric field moves towards the cathode. This result suggests that the electronic breakdown takes places within the dielectric and not at the interface between dielectrics and electrodes.

Space charge dynamics and electric field distribution for LDPE samples with thickness from 5 to 200 μm under 300 V/s voltage rise rate are also modeled. Electric field evolution with the different sample thickness is remarkably similar except for thickness length scale and time-to-breakdown as shown in Figure 6-4. Space charge dynamics also have a similar trend of change and the magnitude of net positive charge density near the anode decreases with the thickness as shown in Figure 6-5. The latter is due to a decrease in amounts of electrons which moved near the anode as the thickness increased.

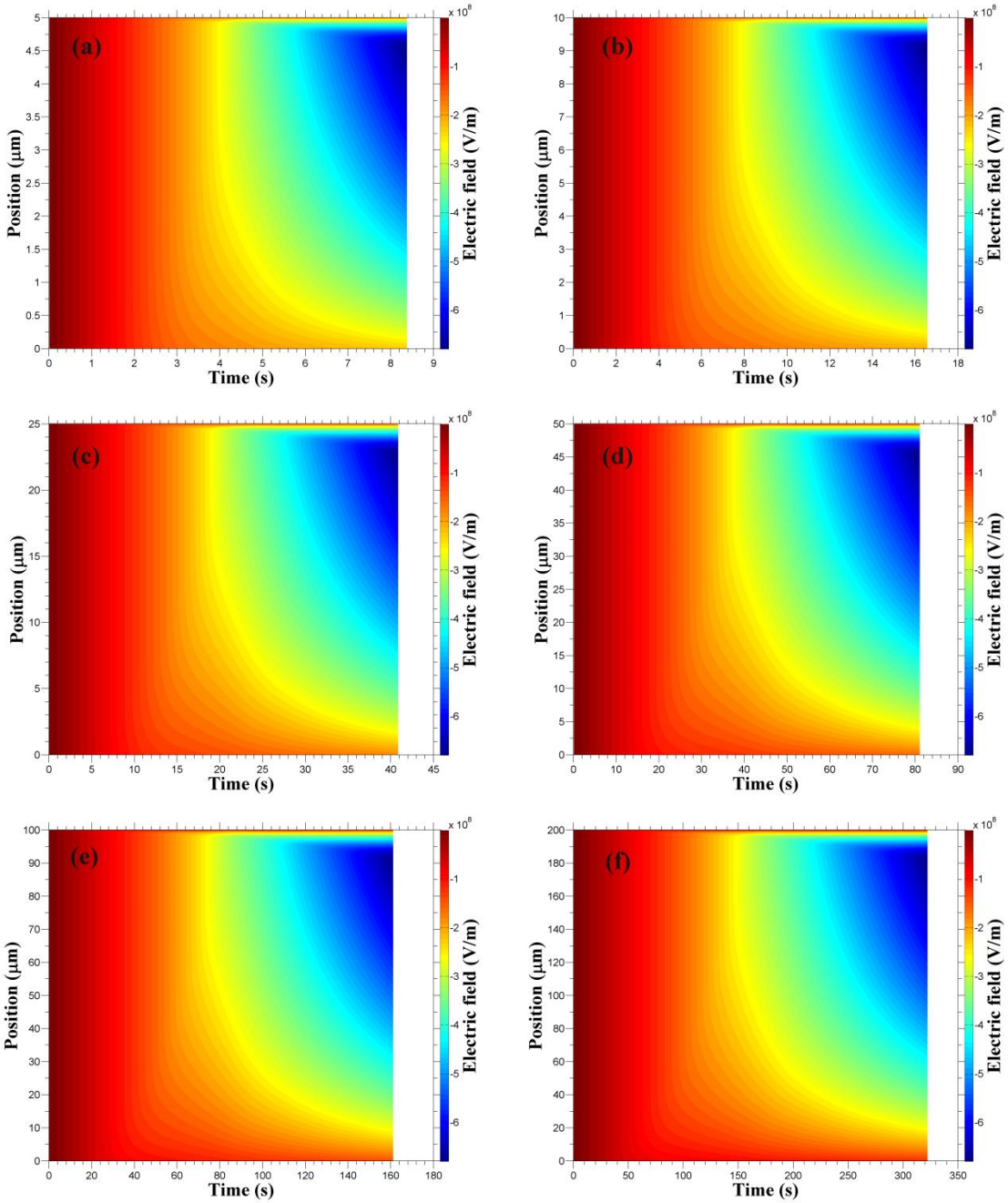

Figure 6-4 Electric field evolution of LDPE samples under 300 V/s voltage ramp; (a) 5 μm (b) 10 μm (c) 25 μm (d) 50 μm (e) 100 μm (f) 200 μm.

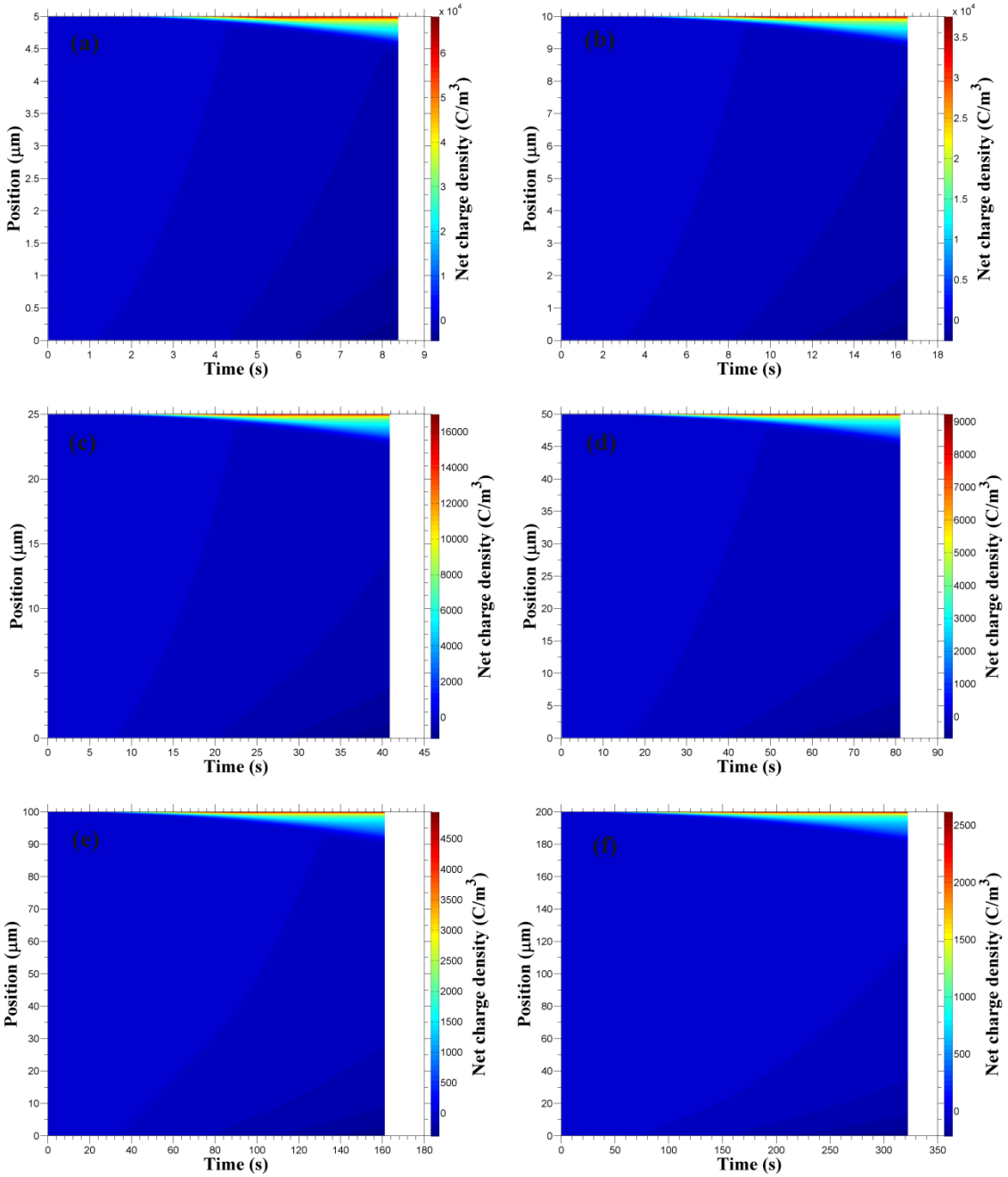

Figure 6-5 Net charge density profile of LDPE samples under 300 V/s voltage ramp; (a) 5 µm (b) 10 µm (c) 25 µm (d) 50 µm (e) 100 µm (f) 200 µm.

6.3.2. Modeling of breakdown strength for LDPE using the constant mobility

Breakdown strength of LDPE samples with thickness from 5 μm to 200 μm under 300 V/s voltage ramp was modeled using the constant mobility. For samples with this thickness range the local electric field near the anode reached the intrinsic breakdown strength as described previously and dielectric breakdown takes place. Breakdown strength of LDPE samples decreases as thickness increases and the rate of decreasing in breakdown strength is reduced with the thickness as shown in Figure 6-6. This trend coincides with the modeling result of LDPE by Chen et al[20]. The difference of about 20 % in the magnitude of the breakdown strength comes from different assumption of hole mobility[20]. Compared to constant hole mobility Chen et al. used field dependent hole mobility which decreases with electric field. Then in their case there is more space charge buildup near anode which decreases breakdown strengths.

The thickness dependence of the breakdown strength is often plotted in the logarithmic scale. Figure 6-7 shows that breakdown strengths in our model for LDPE are weakly thickness dependent. This agrees with Chen's results which also show weakly thickness dependent breakdown strengths. In low-alkali BAS glasses Lee and Murata also showed weakly thickness dependent breakdown strengths[28, 29].

The voltage rise rate dependence of breakdown field is also important and experimental results show that breakdown strength for polyethylene increases as the rate increases. This can be the validating tool for our breakdown model. Figure 6-8 shows the effect of a voltage rise rate

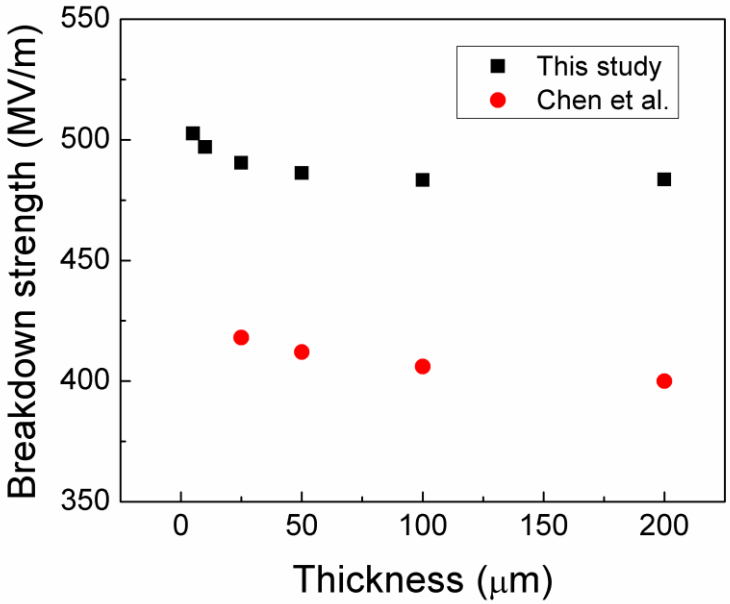

Figure 6-6 Breakdown strength of LDPE with thickness from 5 μm to 200 μm compared with Chen et al.'s modeling data[20].

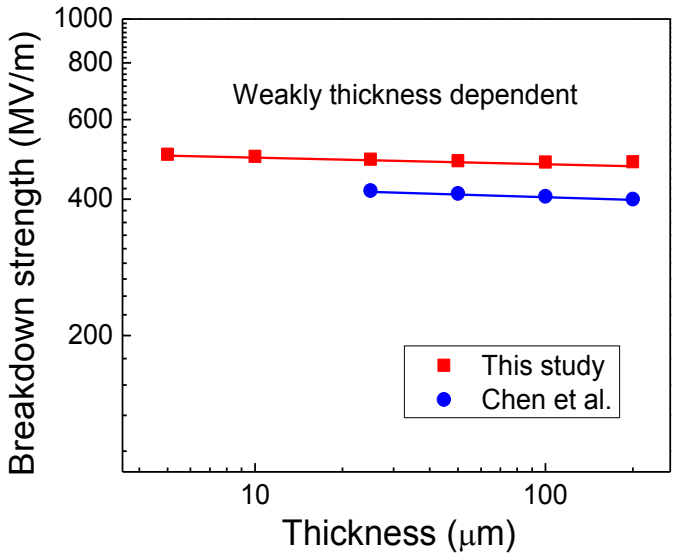

Figure 6-7 Breakdown strength of LDPE with thickness from 5 μm to 200 μm on the log-log plot.

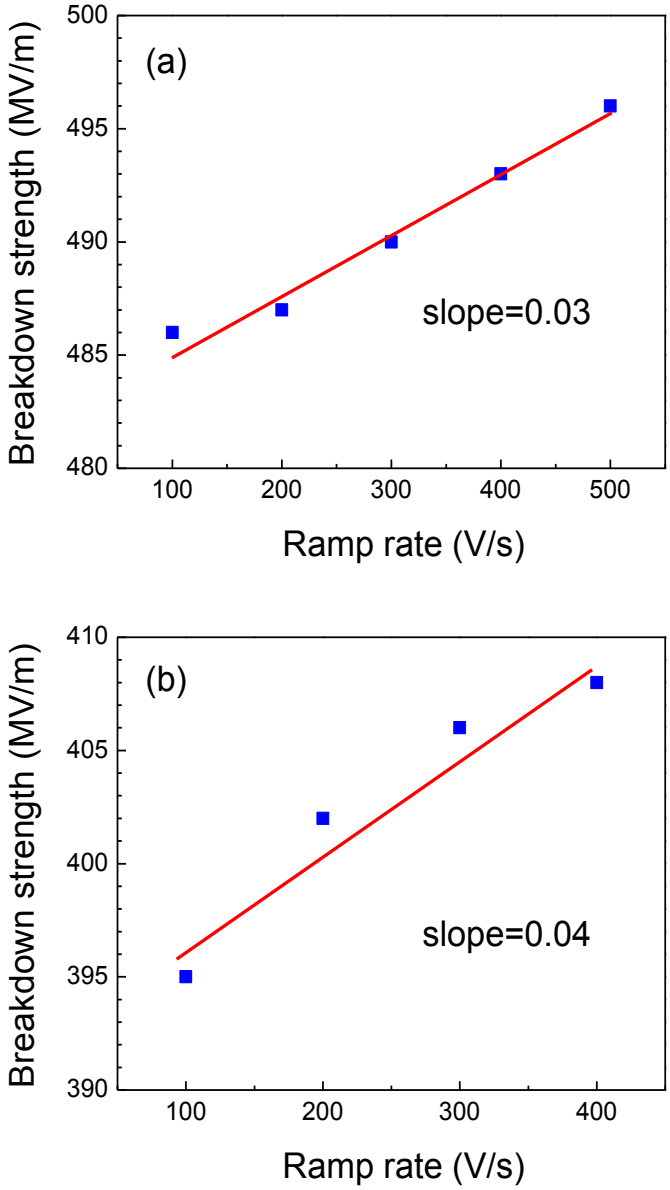

Figure 6-8 (a) Influence of voltage rise rate on the breakdown strength of 25 μm LDPE by this model; (b)Influence of voltage rise rate on the breakdown strength of 100 μm LDPE by Chen[20].

from 100 V/s to 500 V/s on the electrical breakdown field for 25 μm thick LDPE. The breakdown field increases with the voltage rise rate which agrees with modeling results from Chen[20]. As shown in Figure 6-8 the increasing rate (0.03) of breakdown strength with voltage rise rate is close to that (0.04) of Chen.

The temperature rise from Joule heating until the breakdown is also tested. For all the different samples the temperature increased by less than 1 ^{o}C. Therefore at 25 ^{o}C the effect of temperature on the breakdown strength was negligible.

6.4. Conclusions

A model for electrical breakdown under DC conditions has been proposed for low-density polyethylene. The model is based on bipolar charge injection and the space charge formation under higher electric fields which is experimentally verified. From the modeling it is shown that the space charge dynamics lead to weakly thickness dependent breakdown strength at room temperature which is also predicted by other researcher[20]. Furthermore, the relationship between the breakdown strength and voltage rise rate can be reproduced in the model.

Currently, there is limited DC breakdown strength data for polyethylene while AC breakdown data is much more abundant. Further experimental works for breakdown strength in polyethylene such as thickness dependence and ramp rate dependence can help testing this numerical model. On the other hand, temperature dependence of electron mobility and hole mobility should be studied for further applying this numerical model to temperature dependence of breakdown strength. Temperature dependence of volumetric heat capacity and thermal conductivity will be also useful to improve the accuracy of temperature dependent breakdown strength using this model.

6.5. References

1. Hikita, M., M. Ieda, and G. Sawa, *Numerical analysis of steady-state thermal breakdown.* Journal of Applied Physics, 1983. **54**(4): p. 2025-2029.
2. Hikita, M., et al., *Dielectric breakdown and electrical conduction of poly (vinylidene-fluoride) in high temperature region.* Journal of Physics D: Applied Physics, 1980. **13**: p. 661.
3. Hikita, M., G. Sawa, and M. Ieda, *Electrical breakdown and solid structure of poly (vinylidene-fluoride).* Journal of Physics D: Applied Physics, 1983. **16**: p. L157.
4. Ieda, M., M. Nagao, and M. Hikita, *High-field conduction and breakdown in insulating polymers. Present situation and future prospects.* Dielectrics and Electrical Insulation, IEEE Transactions on, 1994. **1**(5): p. 934-945.

5. Wintle, H., *Electrothermal breakdown: Analytic solutions for currents and fields.* Journal of Applied Physics, 1981. **52**(6): p. 4181-4185.
6. Rose, A., *Space-charge-limited currents in solids.* Physical Review, 1955. **97**(6): p. 1538.
7. Lampert, M.A., *Simplified theory of space-charge-limited currents in an insulator with traps.* Physical Review, 1956. **103**(6): p. 1648.
8. Lampert, M.A., *Volume-controlled current injection in insulators.* Reports on Progress in Physics, 1964. **27**: p. 329.
9. Keller, K.J., *Formation and Annulment of Space Charges Glass and Their Influence on Electric Breakdown.* Physical Review, 1952. **86**(5): p. 804-805.
10. Bradwell, A., R. Cooper, and B. Varlow. *Conduction in polythene with strong electric fields and the effect of prestressing on the electric strength*. in *Proceedings of the Institution of Electrical Engineers*. 1971: IET.
11. Ahmed, N. and N. Srinivas, *Review of space charge measurements in dielectrics.* Dielectrics and Electrical Insulation, IEEE Transactions on, 1997. **4**(5): p. 644-656.
12. Fleming, R., *Space charge profile measurement techniques: recent advances and future directions.* Dielectrics and Electrical Insulation, IEEE Transactions on, 2005. **12**(5): p. 967-978.
13. Montanari, G., et al., *Space-charge trapping and conduction in LDPE, HDPE and XLPE.* Journal of Physics D: Applied Physics, 2001. **34**(18): p. 2902.
14. Lepienski, C., et al., *Electric field distribution and near-surface modifications in soda-lime glass submitted to a dc potential.* Journal of Non-Crystalline Solids, 1993. **159**(3): p. 204-212.
15. Fukuma, M., M. Nagao, and M. Kosaki. *Numerical analysis of dielectric breakdown in polypropylene film based on thermal and electronic composite breakdown model*. in *Properties and Applications of Dielectric Materials, 1991., Proceedings of the 3rd International Conference on*. 1991: IEEE.
16. Zebouchi, N., T. Hoang, and B. Ai, *Thermoelectronic breakdown with pressure and space charge effects in polyethylene.* Journal of Applied Physics, 1997. **81**(5): p. 2363-2369.
17. Alison, J. and R. Hill, *A model for bipolar charge transport, trapping and recombination in degassed crosslinked polyethene.* Journal of Physics D: Applied Physics, 1994. **27**(6): p. 1291.
18. Le Roy, S., G. Teyssedre, and C. Laurent, *Charge transport and dissipative processes in insulating polymers: experiments and model.* Dielectrics and Electrical Insulation, IEEE Transactions on, 2005. **12**(4): p. 644-654.
19. Belgaroui, E., et al., *A new numerical model applied to bipolar charge transport, trapping and recombination under low and high dc voltages.* Journal of Physics D: Applied Physics, 2007. **40**(21): p. 6760.
20. Chen, G., et al., *Origin of thickness dependent dc electrical breakdown in dielectrics.* Applied Physics Letters, 2012. **100**(22): p. 222904-222904-4.
21. O'Dwyer, J.J., *The theory of electrical conduction and breakdown in solid dielectrics*. 1973: Clarendon Press Oxford.
22. Okamatsu, T., H. Sano, and H. Takagi, *Effects of grain boundary and segregated-phases on reliability of Ba(Ti,Zr)O_3-based Ni electrode MLCs.* Japanese Journal of Applied Physics Part 1-Regular Papers Brief Communications & Review Papers, 2005. **44**(9B): p. 7186-7189.
23. Matsui, K., et al., *Space charge behavior in low density polyethylene at pre-breakdown.* Dielectrics and Electrical Insulation, IEEE Transactions on, 2005. **12**(3): p. 406-415.

24. Fukuma, M., K. Fukunaga, and C. Laurent, *Two-dimensional structure of charge packets in polyethylene under high dc fields.* Applied Physics Letters, 2006. **88**(25): p. 253110-253110-2.
25. Hikita, M., et al., *Electrical Breakdown of Ethylene Copolymers.* Electrical Insulation, IEEE Transactions on, 1987(2): p. 175-179.
26. Le Roy, S., et al., *Description of charge transport in polyethylene using a fluid model with a constant mobility: fitting model and experiments.* Journal of Physics D: Applied Physics, 2006. **39**(7): p. 1427.
27. Zhao, J., G. Chen, and P. Lewin, *Investigation into the formation of charge packets in polyethylene: Experiment and simulation.* Journal of Applied Physics, 2012. **112**(3): p. 034116-034116-6.
28. Lee, H., et al., *Dielectric Breakdown of Thinned $BaO–Al_2O_3–B_2O_3–SiO_2$ Glass.* Journal of the American Ceramic Society, 2010. **93**(8): p. 2346-2351.
29. Murata, T., et al., *Electrode-Limited Dielectric Breakdown of Alkali Free Glass.* Journal of the American Ceramic Society, 2012.

Chapter 7: Conclusions and Future Work

7.1. Conclusions

The motivation of this research was to gain an insight into the space charge dynamics during electrical breakdown and thermal poling of low-alkali BAS glass and low-density polyethylene using numerical techniques. There are many theories about electrical breakdown in dielectric solids including thermal, electronic, electromechanical, and partial discharge breakdown[1]. However, it is generally difficult to understand breakdown mechanism through only experimental works since the breakdown mechanism depends on the combination of temperature, voltage ramp rate, sample thickness, composition and defects[2]. With the aid of numerical techniques, taking into account of thermal breakdown and electronic breakdown via electrical conduction, this research can provide some insights about breakdown process and space charge dynamics in low-alkali BAS and low-density polyethylene. On the basis of the systematic research in this work following conclusions can be made.

1. Understanding electrical conduction is important to predict breakdowns strengths of dielectric materials. Conduction mechanisms for AF45 glass(one of low-alkali BAS) below 473 K were studied using Schottky, Poole-Frenkel, Space-charge-limited current, and ionic hopping conduction mechanism. Schottky and Poole-Frenkel mechanisms were successful to predict current density in the glass at high temperature (>423 K) since calculated permittivities were close to the static permittivity. Space-charge-limited conduction mechanism was also possible for high temperature (423 K) and high electric field regions. Ionic hopping conduction mechanism also provided reasonable hopping distances between 0.62 and 1.2 nm. Therefore it is concluded

that the conduction in low-alkali BAS glass is governed by a combination of two or more conduction mechanisms.

2. Cation depletion phenomena during thermal poling of low-alkali BAS is an important precursor to dielectric breakdown. Analytical method using von Hippel's theory which is widely used for fused silica predicted much smaller depletion widths for AF45 and OA10G glasses compared to experimental widths. An analytical method assuming proton ion exchange was also applied, and more realistic depletion widths for both glasses were predicted. However, these analytical methods can predict depletion widths only in steady state conditions and do not include migration of other possible charge carriers such as NBO and Ba^{2+}(Ca^{2+}). Therefore several numerical models assuming multiple mobile charges were developed and applied to thermal poling process of low-alkali BAS. These numerical models include charge compensation from other mobile ions and predict depletions widths close to experimental ones. Among them the model assuming motion of Na^{+}, H_3O^{+}/H^{+}, and Ba^{2+} can predict the maximum electric field inside bulk not at the anode for AF45 glass which confirms the experimental electric field profile determined by optical second order nonlinearity measurement[3].

3. Numerical models were developed assuming electronic conduction or ionic redistribution and electronic breakdown respectively. These models were applied to predict the thickness and temperature dependence of breakdown strengths. The model assuming electronic conduction predicted weakly thickness dependent breakdown strengths below 20 μm although it cannot predict strongly thickness dependent breakdown strengths above 20 μm. Another combined breakdown model assuming ionic redistribution and electronic breakdown predicted two distinct regions in AF45 glass for thickness dependence of breakdown strengths. Interestingly temperature dependence of breakdown strengths for AF45 glass predicted by the combined breakdown model agreed well with experimental results. This model showed that the change in

breakdown strengths with temperature mostly depended on the initial mobile sodium concentration.

4. Thermal and electronic breakdown combined model was also applied to low-density polyethylene (polymer insulator). In this material, electronic conduction was assumed with charge carriers of both electrons and holes which has been experimentally demonstrated[4]. In this model electrons and holes are injected at the cathode and the anode respectively with Schottky mechanism. Upon high electric fields these carriers move and produce space charges which enhance local electric field near the anode. This breakdown model predicts weakly thickness dependent breakdown strengths at room temperature which is also predicted by other researchers[4]. Furthermore, the relationship between the breakdown strength and voltage ramp rate can be reproduced in this model.

7.2. Future Work

1. Electrical conduction mechanism is important for understanding both breakdown mechanism and thermal poling in low-alkali BAS. Various kinds of conduction mechanism including both electronic and ionic mechanism were applied to analyze their current density data at various temperature and electric field in Chapter 3. However, there are other possibilities that proton and/or NBO contribute the electrical conduction in the glass system. Therefore it will be helpful to apply the concept that after depletion of sodium ions the conduction is determined by motion of NBO or proton as Carlson et al. did for alkali-containing glass[5, 6].

2. Several numerical models for thermal poling in low-alkali BAS are developed assuming multiple charge carriers in Chapter 4. It is necessary to confirm these numerical models experimentally. For this purpose it is important to determine what charge carriers are during thermal poling. It is possible to use several characterization techniques such as NMR and ion-

scattering for measuring Na^+, NBO, $Ba^{2+}(Ca^{2+})$, H^+/H_3O^+ profiles after thermal poling. It will be also helpful to measure the depletion widths as a function of temperature, applied voltage, and poling time. These depletion widths data can further verify the numerical models for thermal poling.

3. Numerical models were applied to analyze the breakdown strengths of low-alkali BAS and low-density polyethylene. It will be interesting for the model assuming ionic redistribution and electronic breakdown to apply barium titanate single crystals or polycrystals since this is one of most important dielectric materials. The model for barium titanate single crystals is similar to the case of low-alkali BAS since oxygen vacancies might be the dominant charge carrier. Then if the mobility and concentration of oxygen vacancies are known for the given testing condition (electric field, temperature, etc) then the combined model can predict the breakdown strengths for barium titanate single crystals.

4.It is demonstrated that low-alkali BAS coated with polymer has higher breakdown strengths than that of low-alkali BAS without polymer coating. Further study is necessary to understand the mechanism of breakdown strength enhancement. Then impedance spectroscopy or thermally stimulated depolarization current can be useful to characterize and understand the underlying phenomena between glass and polymer film. The numerical modeling technique can also provide some insights about the effect of interfacial polarization between glass and polymer on breakdown strengths.

5.The mobility of mobile ions such as Na^+, H_3O^+/H^+, and $Ba^{2+}(Ca^{2+})$ and their concentration are crucial to calculate the depletion widths and breakdown strengths in low-alkali BAS. For this purpose the current density measurement is not enough since it cannot provide the mobility and mobile ion concentration separately. Therefore it is necessary to determine the mobile ion concentration using different techniques such as electrode polarization or capacitance-voltage technique[7] as a function of temperature. The experimentally determined values could

then be incorporated into the numerical model, which will provide more accurate predictions of the breakdown strength.

7.3. References

1. O'Dwyer, J.J., *The theory of electrical conduction and breakdown in solid dielectrics*. 1973: Clarendon Press Oxford.
2. Dissado, L.A. and J.C. Fothergill, *Electrical degradation and breakdown in polymers*. Vol. 9. 1992: Peter Peregrinus Ltd.
3. Dash, P., *Dynamics of Space Charge Polarization and Electrical Conduction in Low Alkali Boroaluminosilicate glasses*, in *Engineering Science and Mechanics*. 2013, The Pennsylvania State University: University Park.
4. Chen, G., et al., *Origin of thickness dependent dc electrical breakdown in dielectrics.* Applied Physics Letters, 2012. **100**(22): p. 222904-222904-4.
5. Carlson, D., *Ion depletion of glass at a blocking anode: I, theory and experimental results for alkali silicate glasses.* Journal of the American Ceramic Society, 1974. **57**(7): p. 291-294.
6. Carlson, D., *Anodic proton injection in glasses.* Journal of the American Ceramic Society, 1974. **57**(11): p. 461-466.
7. Tomozawa, M. and D.-W. Shin, *Charge carrier concentration and mobility of ions in a silica glass.* Journal of Non-Crystalline Solids, 1998. **241**(2): p. 140-148.

Appendix A

Derivation of ODE for capacitor Ragone plot

Derivation of ODE for capacitor Ragone plot

$$\left(1-\frac{RP}{U^2}\right)\frac{dU^2}{dt}=-\frac{2P}{C} \quad (A.1)$$

Start with two equations Eqn. (A.2) and Eqn. (A.3) for U

$$U=\frac{P}{I}=-\frac{P}{dQ/dt} \quad (A.2)$$

$$U=\frac{Q}{C}-RI=\frac{Q}{C}+R\frac{dQ}{dt} \quad (A.3)$$

Differentiate Eqn. (A.2) and Eqn. (A.3) with respect to time, then

$$\frac{dU}{dt}=\frac{P}{(\frac{dQ}{dt})^2}\frac{d^2Q}{dt^2} \quad (A.4)$$

$$\frac{dU}{dt}=\frac{1}{C}\frac{dQ}{dt}+R\frac{d^2Q}{dt^2}\rightarrow\frac{d^2Q}{dt^2}=\frac{1}{R}(\frac{dU}{dt}-\frac{1}{C}\frac{dQ}{dt}) \quad (A.5)$$

Insert Eqn. (A.5) into Eqn. (A.4), then

$$\frac{dU}{dt}=\frac{P}{R\left(\frac{dQ}{dt}\right)^2}(\frac{dU}{dt}-\frac{1}{C}\frac{dQ}{dt}) \quad (A.6)$$

Multiply U for each side of Eqn. (A.6) and rearrange,

$$(\frac{dQ}{dt})^2U\frac{dU}{dt}=\frac{P}{R}(U\frac{dU}{dt}-\frac{U}{C}\frac{dQ}{dt}) \quad (A.7)$$

Use relationship between dU^2/dt and dU/dt

$$\frac{dU^2}{dt}=2U\frac{dU}{dt} \quad (A.8)$$

Insert Eqn. (A.8) into Eqn. (A.7), then

$$(\frac{dQ}{dt})^2\frac{1}{2}\frac{dU^2}{dt}=\frac{P}{R}(\frac{1}{2}\frac{dU^2}{dt}-\frac{U}{C}\frac{dQ}{dt}) \quad (A.9)$$

$$\frac{dQ}{dt}=-\frac{P}{U} \quad (A.10)$$

Insert Eqn. (A.10) into Eqn. (A.9) and we finally get the Eqn. (A.1).

$$\frac{P^2}{U^2}\frac{dU^2}{dt} = \frac{P}{R}\left(\frac{dU^2}{dt} + \frac{2P}{C}\right) \rightarrow \left(1 - \frac{RP}{U^2}\right)\frac{dU^2}{dt} = -\frac{2P}{C} \quad \text{(A.1)}$$

Appendix B

Derivation of impulse thermal breakdown Eqn. (2-4)

In the impulse thermal breakdown condition it is assumed that the heat loss to the surrounding environment plays a negligible role due to a short time scale until the breakdown. Then the power balance equation between heat generation rate and heat loss rate can be expressed by

$$C_v \frac{dT}{dt} = \sigma E^2 \tag{B.1}$$

where C_v is the specific heat per unit volume, T the temperature, t the time, σ the electrical conductivity, and E the electric field. Assuming a linear ramp rate of electric field, E can be given by E=at where a is a constant. If σ can be expressed by the Arrhenius equation of

$$\sigma = \sigma_0 \exp\left(-\frac{E_a}{k_B T}\right) \tag{B.2}$$

where σ_0 is the pre-exponential factor, E_a the activation energy, and k_B the Boltzmann constant. If Eqn. (B.2) is inserted into Eqn. (B.1), it yields

$$C_v \frac{dT}{dt} = \sigma_0 (at)^2 \exp\left(-\frac{E_a}{k_B T}\right) \tag{B.3}.$$

Separation of variables for Eqn. (B.3) yields

$$\exp\left(\frac{E_a}{k_B T}\right) dT = \frac{\sigma_0 (at)^2}{C_v} dt \tag{B.3}.$$

Integration for T from T_0 to T and for t from 0 to t give

$$\int_{T_0}^{T} \exp\left(\frac{E_a}{k_B T}\right) dT = \int_0^t \frac{\sigma_0 (at)^2}{C_v} dt$$

$$\frac{k_B T_0^2}{E_a}\left[\exp\left(\frac{E_a}{k_B T_0}\right) - \exp\left(\frac{E_a}{k_B T}\right)\right] \approx \frac{\sigma_0 a^2}{3C_v} t^3 \tag{B.4}.$$

It is assumed that C_v is independent of temperature and $E_a >> k_B T$.

Appendix C

Matlab code for modeling cation depletion widths assuming Na^+, H_3O^+/H^+, Ba^{2+} migration in low-alkali BAS

```
%2013-08-28
%Calculate charge transport and E field distribution for boroaluminosilicate
%Then calcualte depletion width
%Transport eqn for charge transport and uniform charge distribution for
Na+,H3O+/H+ and Ba
%Ignore diffusion term at charge transport
%Constant mobility for sodium and Ba
%Assume nonblocking electrodes for anode and nonblocking electrode for cathode
%apply multiple charge carriers proposed by Petrov(2012)
%apply estimation of mobile Na (Souquet 2010)
%H3O+/H+ injection (Kudlinski 2005)

clear all;close all;

tic;
%Define material parameters
kb=1.381e-23; %Boltzmann constant(JK-1)
qe=1.602e-19;  %elementary charge(Coulomb)

muNa=1.0e-16; %Sodium mobility(m2/V-s) from Ikeda(2013)
muH=muNa*1e-2; %proton mobility(m2/V-s)
muBa=1.0e-20;%Ba mobility(m2/V-s)
sigma2=5e11; %proton injection rate(m-2V-1s-1)
cNa0=9.41e22; %initial average sample cation or anion concentration (m-3)
cH0=0;  %initial Ba2+ concentration (m-3)
cBa0=2.00e20;   %initial Ba2+ concentration (m-3)

epr_r=6.0;                % Relative permittivity of AF45 glass
epr_0=8.854e-12;          % permittivity of air(F/m)
epr=epr_r*epr_0;          % Absolute permittivity(F/m)
T0=723.15;                %initial and boundary temperature
d=400e-6;                 %sample thickness(m)
Vapp=4000;                                              %applied   voltage
cv=1.84e6;                %volumetric heat capacity(J/m3-K) Zebouchi(1997)
kcon=1.11;                %thermal conductivity(W/m-K)
Tf=1156;                  %melting temperature(K)
Fmax=1160e6;              %electronic breakdown strength
m=4096;                   %number of steps for distance
h=d/m; %distance step(m)
pNa0=ones(m,1)*cNa0;        %initial Na concentration (#/m3)
pH0=ones(m,1)*cH0;        %initial Ba concentration (#/m3)
pBa0=ones(m,1)*cBa0;        %initial Ba concentration (#/m3)

dt = 5e-2;                              % time step
tmax=1800;  %poling time
tcef=1;          % time interval for file save
kmax=round(tmax/dt);                     % maximum k
xn=0;               % Number of graph plotting

%  Initialize profiles
x1=(0:h:d)*1e6; %set distance profile(um) for E field and current density
x2=(0.5*h:h:d-0.5*h)*1e6;   %set distance profile(um) for charge density
```

```
pH=ones(m,1)*cH0;   %bulk proton concentration(#/m3)
pNa=ones(m,1)*cNa0; %bulk Na+ concentration(#/m3)
pBa=ones(m,1)*cBa0; %bulk barium ion concentration(#/m3)
pH1=zeros(m,1);   %mobile proton concentration(#/m3)
pNa1=zeros(m,1);   %mobile sodium concentration(#/m3)
pBa1=zeros(m,1);   %mobile barium concentration(#/m3)

rhs=zeros(m,1);
F=zeros(m+1,1);  %electric field profile(V/m)
V=zeros(m+2,1);     %voltage profile (V)
Vtemp=zeros(m,1);     %voltage profile (V)
JH=zeros(m+1,1);       %proton current density(A/m2)
JNa=zeros(m+1,1);       %sodium ionic current density(A/m2)
JBa=zeros(m+1,1);       %barium ionic current density(A/m2)
Tlocal0=ones(m,1)*T0;      %local temperature(K)
Tlocal1=ones(m,1)*T0;      %local temperature(K)

t=0;

fid1=fopen('t_Na_H_Ba_4kV_723K_30min_400um_af45_nb.txt','w');
fid2=fopen('Efield_Na_H_Ba_4kV_723K_30min_400um_af45_nb.txt','w');
fid3=fopen('ntotal_Na_H_Ba_4kV_723K_30min_400um_af45_nb.txt','w');
fid4=fopen('pH_Na_H_Ba_4kV_723K_30min_400um_af45_nb.txt','w');
fid5=fopen('pNa_Na_H_Ba_4kV_723K_30min_400um_af45_nb.txt','w');
fid6=fopen('pBa_Na_H_Ba_4kV_723K_30min_400um_af45_nb.txt','w');
fid7=fopen('Tlocal_Na_H_Ba_4kV_723K_30min_400um_af45_nb.txt','w');
fid8=fopen('Type_Ebd_Na_H_Ba_4kV_723K_30min_400um_af45_nb.txt','w');
fid9=fopen('JH_Na_H_Ba_4kV_723K_30min_400um_af45_nb.txt','w');
fid10=fopen('JNa_Na_H_Ba_4kV_723K_30min_400um_af45_nb.txt','w');
fid11=fopen('JBa_Na_H_Ba_4kV_723K_30min_400um_af45_nb.txt','w');

 %1d Poisson matrix
 L1D = spdiags(ones(m,1)*[-1 2 -1],-1:1,m,m);

 %1d matrix for power balance eqn
 coeff=kcon/cv;
 pbA = spdiags(ones(m,1)*[-coeff/h^2 1/dt+2*coeff/h^2 -coeff/h^2],-1:1,m,m);

for k=1:kmax   %Time Loop for poling time
   t=k*dt;  % current time
   %calculate E field distribution using Poisson's eqn and previous charge
density
   rhs=qe*(pNa+pH+2*pBa-pNa0-pH0-2*pBa0)*(h^2/epr);
   rhs(1)=qe*(pNa(1)+pH(1)+2*pBa(1)-pNa0(1)-pH0(1)-2*pBa0(1))*(h^2/epr);
   rhs(m)=qe*(pNa(m)+pH(m)+2*pBa(m)-pNa0(m)-pH0(m)-2*pBa0(m))*(h^2/epr)+Vapp;
   Vtemp=L1D\rhs;
   V=[0;Vtemp;Vapp];
   F=-diff(V)/h;    %Electric field

   %calculate current density for electron using transport eqn and previous
charge density
   %H current density, JH<0
   JH(1)=muH.*pH(1).*F(1)*qe;  %proton current density at cathode
   JH(m+1)=0;  %proton current density at anode
   JH(2:m)=muH.*pH(2:m).*F(2:m)*qe;   %proton current density
   %Na+ current density, JNa<0
    JNa(1)=muNa.*pNa(1).*F(1)*qe;  %Na+ current density at cathode
   JNa(m+1)=0;%JNa(m+1)=0; %Na+ current density at anode
   JNa(2:m)=muNa.*pNa(2:m).*F(2:m)*qe;%Na+ current density
   %Ba current density, JBa<0
   JBa(1)=muBa.*pBa(1).*F(1)*2*qe; %Ba2+ current density at cathode
```

```
JBa(m+1)=0;%JBa(m+1)=0;  %Ba2+ current density at anode
JBa(2:m)=muBa.*pBa(2:m).*F(2:m)*2*qe;     %Ba2+ current density
%calcualte net charge density using continuity eqn
%H charge density
pH1=pH-(dt/h)*diff(JH)/qe;        % H concentration
pH1(m)=pH(m)-dt*sigma2*F(m+1);        %proton injection at anode
%Na+ charge density
pNa1=pNa-(dt/h)*diff(JNa)/qe;        % Na concentration
%Ba2+ charge density
pBa1=pBa-(dt/h)*diff(JBa)/(2*qe);        % Ba2+ concentration

%replace previous charge density with current charge density
pH=pH1; pNa=pNa1; pBa=pBa1;
%calcualte total mobile ion concentration (#/m3)
ntotal=qe*(pNa+pH+2*pBa-pNa0-pH0-2*pBa0);

%Calcualte local temperature using Tn and heat source
Fav=(abs(F(1:m))+abs(F(2:m+1)))/2;
JHAv=(abs(JH(1:m))+abs(JH(2:m+1)))/2;
JNaAv=(abs(JNa(1:m))+abs(JNa(2:m+1)))/2;
JBaAv=(abs(JBa(1:m))+abs(JBa(2:m+1)))/2;
hs=JHAv.*Fav+JNaAv.*Fav+JBaAv.*Fav;       %calcualte heat source
pbB=1/dt*Tlocal0+hs/cv;
pbB(1)=1/dt*Tlocal0(1)+hs(1)/cv+(coeff/h^2)*T0;
 pbB(m)=1/dt*Tlocal0(m)+hs(m)/cv+(coeff/h^2)*T0;
Tlocal1=pbA\pbB;          %calcualte local temp using backward Euler method
Temp=[T0;Tlocal1;T0];
Tlocal0=Tlocal1; %replace old local temperature with new local temperature

if mod(t*tcef,1)==0 %mod(t*10,1)==0
     fprintf(fid1,'%f\n',t);
     fprintf(fid2,'%f\t',F);
     fprintf(fid2,'\n');
     fprintf(fid3,'%f\t',ntotal);
     fprintf(fid3,'\n');
     fprintf(fid4,'%f\t',pH);
     fprintf(fid4,'\n');
     fprintf(fid5,'%f\t',pNa);
     fprintf(fid5,'\n');
     fprintf(fid6,'%f\t',pBa);
     fprintf(fid6,'\n');
     fprintf(fid7,'%f\t',Temp);
     fprintf(fid7,'\n');
     fprintf(fid9,'%f\t',abs(JH));
     fprintf(fid9,'\n');
     fprintf(fid10,'%f\t',abs(JNa));
     fprintf(fid10,'\n');
     fprintf(fid11,'%f\t',abs(JBa));
     fprintf(fid11,'\n');
     xn=xn+1;
elseif (max(abs(F)) >= Fmax)
     fprintf(fid1,'%f\n',t);
     fprintf(fid2,'%f\t',F);
     fprintf(fid2,'\n');
     fprintf(fid3,'%f\t',ntotal);
     fprintf(fid3,'\n');
     fprintf(fid4,'%f\t',pH);
     fprintf(fid4,'\n');
     fprintf(fid5,'%f\t',pNa);
     fprintf(fid5,'\n');
     fprintf(fid6,'%f\t',pBa);
```

```
        fprintf(fid6,'\n');
        fprintf(fid7,'%f\t',Temp);
        fprintf(fid7,'\n');
        fprintf(fid9,'%f\t',abs(JH));
        fprintf(fid9,'\n');
        fprintf(fid10,'%f\t',abs(JNa));
        fprintf(fid10,'\n');
        fprintf(fid11,'%f\t',abs(JBa));
        fprintf(fid11,'\n');
        xn=xn+1;
    elseif (max(Tlocal0) >= Tf)
        fprintf(fid1,'%f\n',t);
        fprintf(fid2,'%f\t',F);
        fprintf(fid2,'\n');
        fprintf(fid3,'%f\t',ntotal);
        fprintf(fid3,'\n');
        fprintf(fid4,'%f\t',pH);
        fprintf(fid4,'\n');
        fprintf(fid5,'%f\t',pNa);
        fprintf(fid5,'\n');
        fprintf(fid6,'%f\t',pBa);
        fprintf(fid6,'\n');
        fprintf(fid7,'%f\t',Temp);
        fprintf(fid7,'\n');
        fprintf(fid9,'%f\t',abs(JH));
        fprintf(fid9,'\n');
        fprintf(fid10,'%f\t',abs(JNa));
        fprintf(fid10,'\n');
        fprintf(fid11,'%f\t',abs(JBa));
        fprintf(fid11,'\n');
        xn=xn+1;
    end
    if max(abs(F))>=Fmax
        Fbd=Vapp/d;            %set breakdown strength
        fprintf(fid8,'Electronic breakdown mechanism and Ebd is %f\n',Fbd);
        break
    elseif max(Temp)>=Tf
        Fbd=Vapp/d;            %set breakdown strength
        fprintf(fid8,'Thermal breakdown mechanism and Ebd is %f\n',Fbd);
        break
    end
end
fclose('all');

fid1=fopen('t_Na_H_Ba_4kV_723K_30min_400um_af45_nb.txt');
fid2=fopen('Efield_Na_H_Ba_4kV_723K_30min_400um_af45_nb.txt');
fid3=fopen('ntotal_Na_H_Ba_4kV_723K_30min_400um_af45_nb.txt');
fid4=fopen('pH_Na_H_Ba_4kV_723K_30min_400um_af45_nb.txt');
fid5=fopen('pNa_Na_H_Ba_4kV_723K_30min_400um_af45_nb.txt');
fid6=fopen('pBa_Na_H_Ba_4kV_723K_30min_400um_af45_nb.txt');
fid7=fopen('Tlocal_Na_H_Ba_4kV_723K_30min_400um_af45_nb.txt');
fid9=fopen('JH_Na_H_Ba_4kV_723K_30min_400um_af45_nb.txt');
fid10=fopen('JNa_Na_H_Ba_4kV_723K_30min_400um_af45_nb.txt');
fid11=fopen('JBa_Na_H_Ba_4kV_723K_30min_400um_af45_nb.txt');

tplot=fscanf(fid1,'%f');            % time variable for plot
Efield=fscanf(fid2,'%f',[m+1 xn]);
ntotal=fscanf(fid3,'%f',[m xn]);
pH=fscanf(fid4,'%f',[m xn]);
pNa=fscanf(fid5,'%f',[m xn]);
pBa=fscanf(fid6,'%f',[m xn]);
```

```
Temp=fscanf(fid7,'%f',[m+2 xn]);
AJH=fscanf(fid9,'%f',[m+1 xn]);
AJNa=fscanf(fid10,'%f',[m+1 xn]);
AJBa=fscanf(fid11,'%f',[m+1 xn]);

fclose('all');

h1=figure('Visible','off');
%hold on;
axbkgd=axes('Position',[0 0 1 1],'Visible', 'off');
axis([0 1 0 1]);
%formatting figure
set(gcf, 'renderer', 'painters');
set(gcf, 'color', 'white'); % sets the color to white

set(gcf, 'PaperUnits', 'inches');
xSize = 17;         %xSize = 8.5; %inches wide for total page
ySize = 22;         %ySize = 11; %inches high for total page
axisLeft = .1;
axisRight = .58;
axisTop = .73;
axisMiddle = 0.41;
axisBottom = .09;
axisXSize = .35;
axisYSize = .25;
axisInsetSize = .1;
InsetLeft = .30;
InsetBottom = .12;
set(gcf, 'PaperPositionMode', 'manual');
set(gcf, 'PaperSize', [xSize ySize]);
set(gcf, 'PaperPosition', [0 0 xSize ySize]);
Lfntsize=32;
Afntsize=24;

ColorSet=[0 0 0; 0 0 1; 1 0 1; 1 0 0];
LSorder={'-','--',':','-.'};

%titv=fix(xn/10);

%%%%FIGURE UPPER LEFT
ax1=axes('position',[axisLeft,axisTop,axisXSize,axisYSize]);
set(ax1,'FontSize',Afntsize,'XGrid','on');
grid(gca,'minor');
hold on
for kul=1:4

plot(x1',Efield(:,fix(xn*kul/4))./1e6,'Color',ColorSet(kul,:),'LineStyle',LSord
er{kul},'LineWidth',3);
end
xlabel('Position (\mum)','fontsize',Lfntsize,'fontweight','b');
ylabel('E field (MV/m)','fontsize',Lfntsize,'fontweight','b')
xlim([d*1e6-5 d*1e6]);
ylim([-1200 0]);
%text(10,0, '(a)','FontSize',Lfntsize, 'FontWeight','bold');
box off
hold off

%%%%FIGURE UPPER RIGHT
ax2=axes('position',[axisRight,axisTop,axisXSize,axisYSize]);
set(ax2,'FontSize',Afntsize,'XGrid','on');
grid(gca,'minor');
```

```
hold on
for kur=1:4

plot(x2',ntotal(:,fix(xn*kur/4)),'Color',ColorSet(kur,:),'LineStyle',LSorder{ku
r},'LineWidth',3);
end
xlabel('Position (\mum)','fontsize',Lfntsize,'fontweight','b');
ylabel('Net charge density (C/m^{3})','fontsize',Lfntsize,'fontweight','b')
xlim([d*1e6-5 d*1e6]);
ylim auto;  %ylim([-800 800]);
%text(10,800, '(b)','FontSize',Lfntsize, 'FontWeight','bold');
box off
hold off

%%%%FIGURE MIDDLE LEFT
ax3=axes('position',[axisLeft,axisMiddle,axisXSize,axisYSize]);
set(ax3,'FontSize',Afntsize,'XGrid','on');
grid(gca,'minor');
hold on
for kml=1:4

plot(x2',pH(:,fix(xn*kml/4)),'Color',ColorSet(kml,:),'LineStyle',LSorder{kml},'
LineWidth',3);
end
xlabel('Position (\mum)','fontsize',Lfntsize,'fontweight','b');
ylabel('Mobile                          H^{+}                          concentration
(#/m^{3})','fontsize',Lfntsize,'fontweight','b')
xlim([d*1e6-5 d*1e6]);
ylim auto;  %ylim([-10 800]);
%text(10,800, '(c)','FontSize',Lfntsize, 'FontWeight','bold');
box off
hold off

%%%%FIGURE MIDDLE RIGHT
ax4=axes('position',[axisRight,axisMiddle,axisXSize,axisYSize]);
set(ax4,'FontSize',Afntsize,'XGrid','on');
grid(gca,'minor');
hold on
for kmr=1:4

hmr(kmr)=plot(x2',pNa(:,fix(xn*kmr/4)),'Color',ColorSet(kmr,:),'LineStyle',LSor
der{kmr},'LineWidth',3);
    smr{kmr}=sprintf('%4.2f s',tplot(fix(xn*kmr/4)));
end
xlabel('Position (\mum)','fontsize',Lfntsize,'fontweight','b');
ylabel('Mobile                          Na^{+}                          concentration
(#/m^{3})','fontsize',Lfntsize,'fontweight','b')
xlim([d*1e6-5 d*1e6]);
ylim auto;  %ylim([-0.5 40]);
ind=[1 2 3 4];          %select the plots to include in the legend
l1=legend(hmr(ind),smr{ind},'Location','SouthWest');       %Creat legend for the
selected plots
%text(10,40, '(d)','FontSize',Lfntsize, 'FontWeight','bold');
box off
hold off

%%%%FIGURE LOWER LEFT
ax5=axes('position',[axisLeft,axisBottom,axisXSize,axisYSize]);
set(ax5,'FontSize',Afntsize,'XGrid','on');
grid(gca,'minor');
hold on
```

```
for kll=1:4

plot(x2',pBa(:,fix(xn*kll/4)),'Color',ColorSet(kll,:),'LineStyle',LSorder{kll},
'LineWidth',3);
end
xlabel('Position (\mum)','fontsize',Lfntsize,'fontweight','b');
ylabel('Mobile                    Ba^{2+}                    concentration
(#/m^{3})','fontsize',Lfntsize,'fontweight','b')
xlim([d*1e6-5 d*1e6]);
ylim auto;  %ylim([-10 800]);
%text(10,800, '(e)','FontSize',Lfntsize, 'FontWeight','bold');
box off
hold off

print(h1,'-dtiff','2Dplot_Na_H_Ba_4kV_723K_30min_400um_af45_nb.tif');

toc;
```

Appendix D

Matlab code for modeling breakdown strengths assuming ionic conduction in low-alkali BAS

```
%2013-08-28
%Calculate charge transport and E field distribution for boroaluminosilicate
%Transport eqn for charge transport and uniform charge distribution for
Na+,H3O+/H+,and Ba2+
%Ignore diffusion term at charge transport
%Constant mobility for sodium, proton and Ba ions
%Assume nonblocking electrodes for anode and nonblocking electrode for cathode
%apply estimation of mobile Na (Souquet 2010)
%H3O+/H+ injection (Kudlinski 2005)
%Add Onsager theory for sodium dissociation(Onsager 1934, Tomozawa 1980)

clear all;close all;

tic;
%Define material parameters
kb=1.381e-23; %Boltzmann constant(JK-1)
qe=1.602e-19;  %elementary charge(Coulomb)

muNa=4.0e-16;  %Sodium mobility(m2/V-s)
muH=muNa*1e-2; %proton mobility(m2/V-s)
muBa=1.0e-21;   %Ba mobility(m2/V-s)
sigma2=5e11;            %proton injection rate(m-2V-1s-1)
cNa0=9.77e21;  %initial sodium concentration (#/m3)
cH0=0;         %initial proton concentration(#/m3)
cBa0=3.74e13;  %initial Ba2+ concentration (#/m3)
epr_r=6.0;                 % Relative permittivity of glass
epr_0=8.854e-12;           % permittivity of air(F/m)
epr=epr_r*epr_0;           % Absolute permittivity(F/m)
T0=298;                   %initial and boundary temperature
d=50e-6;                   %sample thickness(m)
Vramp=100;        %voltage ramp rate(V/s)
cv=1.84e6;        %volumetric heat capacity(J/m3-K)
kcon=1.11;      %thermal conductivity(W/m-K)
Tf=1156;             %melting temperature(K)
Fmax=1160e6;        %electronic breakdown strength
%Fmax=550e6;         %electronic breakdown strength
m=4096;             %number of steps for distance
h=d/m;              %distance step(m)
pNa0=ones(m,1)*cNa0;        %initial Na concentration (#/m3)
pH0=ones(m,1)*cH0;        %initial Ba concentration (#/m3)
pBa0=ones(m,1)*cBa0;        %initial Ba concentration (#/m3)

dt = 1e-3;                              % time step
tmax=1800;  %poling time
tcef=10;       % time interval for file save
kmax=round(tmax/dt);                    % maximum k
xn=0;               % Number of graph plotting

%  Initialize profiles
x1=(0:h:d)*1e6; %set distance profile(um) for E field and current density
x2=(0.5*h:h:d-0.5*h)*1e6;   %set distance profile(um) for charge density
pH=ones(m,1)*cH0;     %bulk proton concentration (#/m3)
```

```
pNa=ones(m,1)*cNa0; %bulk sodim concentration (#/m3)
pBa=ones(m,1)*cBa0; %bulk barium concentration (#/m3)
pH1=zeros(m,1);   %mobile proton concentration (#/m3)
pNa1=zeros(m,1);   %mobile sodium concentration (#/m3)
pBa1=zeros(m,1);   %mobile barium concentration (#/m3)
rhs=zeros(m,1);
F=zeros(m+1,1);  %electric field profile(V/m)
V=zeros(m+2,1);     %voltage profile (V)
Vtemp=zeros(m,1);     %voltage profile (V)
JH=zeros(m+1,1);       %BO4 current density(A/m2)
JNa=zeros(m+1,1);       %sodium current density(A/m2)
JBa=zeros(m+1,1);       %BO4 current density(A/m2)
Tlocal0=ones(m,1)*T0;      %local temperature(K)
Tlocal1=ones(m,1)*T0;      %local temperature(K)

t=0;

fid1=fopen('t_Na_H_Ba_100Vs_298K_50um_af45_nb.txt','w');
fid2=fopen('Efield_Na_H_Ba_100Vs_298K_50um_af45_nb.txt','w');
fid3=fopen('ntotal_Na_H_Ba_100Vs_298K_50um_af45_nb.txt','w');
fid4=fopen('pH_Na_H_Ba_100Vs_298K_50um_af45_nb.txt','w');
fid5=fopen('pNa_Na_H_Ba_100Vs_298K_50um_af45_nb.txt','w');
fid6=fopen('pBa_Na_H_Ba_100Vs_298K_50um_af45_nb.txt','w');
fid7=fopen('Tlocal_Na_H_Ba_100Vs_298K_50um_af45_nb.txt','w');
fid8=fopen('Type_Ebd_Na_H_Ba_100Vs_298K_50um_af45_nb.txt','w');
fid9=fopen('JH_Na_H_Ba_100Vs_298K_50um_af45_nb.txt','w');
fid10=fopen('JNa_Na_H_Ba_100Vs_298K_50um_af45_nb.txt','w');
fid11=fopen('JBa_Na_H_Ba_100Vs_298K_50um_af45_nb.txt','w');

 %1d Poisson matrix
 L1D = spdiags(ones(m,1)*[-1 2 -1],-1:1,m,m);

 %1d matrix for power balance eqn
 coeff=kcon/cv;
 pbA = spdiags(ones(m,1)*[-coeff/h^2 1/dt+2*coeff/h^2 -coeff/h^2],-1:1,m,m);

for k=1:kmax   % Time Loop for breakdown
   t=k*dt;  % current time
   Vapp=Vramp*t;    % calculate applied voltage
   %calculate E field distribution using Poisson's eqn and previous charge
density
   rhs=qe*(pNa+pH+2*pBa-pNa0-pH0-2*pBa0)*(h^2/epr);
   rhs(1)=qe*(pNa(1)+pH(1)+2*pBa(1)-pNa0(1)-pH0(1)-2*pBa0(1))*(h^2/epr);
   rhs(m)=qe*(pNa(m)+pH(m)+2*pBa(m)-pNa0(m)-pH0(m)-2*pBa0(m))*(h^2/epr)+Vapp;
   Vtemp=L1D\rhs;
   V=[0;Vtemp;Vapp];
   F=-diff(V)/h;    %Electric field

   %calculate current density for electron using transport eqn and previous
charge density
   %H current density, JH<0
    JH(1)=muH*pH(1).*F(1)*qe;     %proton current density at cathode
   JH(m+1)=0;                    %proton current density at anode
   JH(2:m)=muH.*pH(2:m).*F(2:m)*qe;  %proton current density
   %Na+ current density, JNa<0
   JNa(1)=muNa*pNa(1).*F(1)*qe; %Na+ current density at cathode
   JNa(m+1)=0;                   %Na+ current density at anode
   JNa(2:m)=muNa.*pNa(2:m).*F(2:m)*qe; %Na+ current density
   %Ba current density, JBa<0
    JBa(1)=muBa.*pBa(1).*F(1)*2*qe;    %Ba2+ current density at cathode
   JBa(m+1)=0;                         %Ba2+ current density at anode
```

```
    JBa(2:m)=muBa.*pBa(2:m).*F(2:m)*2*qe;    %Ba2+ current density

    %calcualte net charge density using continuity eqn
    %H+ concentration
    pH1=pH-(dt/h)*diff(JH)/qe;        % H concentration
    pH1(m)=pH(m)-dt*sigma2*F(m+1);        %proton injection at anode
    %Na+ concentration
    pNa1=pNa-(dt/h)*diff(JNa)/qe;        % Na concentration
    %Ba2+ concentration
    pBa1=pBa-(dt/h)*diff(JBa)/(2*qe);        % Ba2+ concentration

    %Calcualte local temperature using Tn and heat source
    Fav=(abs(F(1:m))+abs(F(2:m+1)))/2;
    JHAv=(abs(JH(1:m))+abs(JH(2:m+1)))/2;
    JNaAv=(abs(JNa(1:m))+abs(JNa(2:m+1)))/2;
    JBaAv=(abs(JBa(1:m))+abs(JBa(2:m+1)))/2;
    hs=JHAv.*Fav+JNaAv.*Fav+JBaAv.*Fav;       %calcualte heat source
    pbB=1/dt*Tlocal0+hs/cv;
    pbB(1)=1/dt*Tlocal0(1)+hs(1)/cv+(coeff/h^2)*T0;
pbB(m)=1/dt*Tlocal0(m)+hs(m)/cv+(coeff/h^2)*T0;
    Tlocal1=pbA\pbB;          %calcualte local temp using backward Euler method
    Temp=[T0;Tlocal1;T0];
    Tlocal0=Tlocal1;  %replace old local temperature with new local temperature
    %replace previous charge density with current charge density
    pH=pH1; pNa=pNa1; pBa=pBa1;
    %calcualte total mobile ion concentration (#/m3)
    ntotal=qe*(pNa+pH+2*pBa-pNa0-pH0-2*pBa0);

    if mod(t*tcef,1)==0 %mod(t*10,1)==0
         fprintf(fid1,'%f\n',t);
         fprintf(fid2,'%f\t',F);
         fprintf(fid2,'\n');
         fprintf(fid3,'%f\t',ntotal);
         fprintf(fid3,'\n');
         fprintf(fid4,'%f\t',pH);
         fprintf(fid4,'\n');
         fprintf(fid5,'%f\t',pNa);
         fprintf(fid5,'\n');
         fprintf(fid6,'%f\t',pBa);
         fprintf(fid6,'\n');
         fprintf(fid7,'%f\t',Temp);
         fprintf(fid7,'\n');
         fprintf(fid9,'%f\t',abs(JH));
         fprintf(fid9,'\n');
         fprintf(fid10,'%f\t',abs(JNa));
         fprintf(fid10,'\n');
         fprintf(fid11,'%f\t',abs(JBa));
         fprintf(fid11,'\n');
         xn=xn+1;
    elseif (max(abs(F)) >= Fmax)
         fprintf(fid1,'%f\n',t);
         fprintf(fid2,'%f\t',F);
         fprintf(fid2,'\n');
         fprintf(fid3,'%f\t',ntotal);
         fprintf(fid3,'\n');
         fprintf(fid4,'%f\t',pH);
         fprintf(fid4,'\n');
         fprintf(fid5,'%f\t',pNa);
         fprintf(fid5,'\n');
         fprintf(fid6,'%f\t',pBa);
         fprintf(fid6,'\n');
```

```
        fprintf(fid7,'%f\t',Temp);
        fprintf(fid7,'\n');
        fprintf(fid9,'%f\t',abs(JH));
        fprintf(fid9,'\n');
        fprintf(fid10,'%f\t',abs(JNa));
        fprintf(fid10,'\n');
        fprintf(fid11,'%f\t',abs(JBa));
        fprintf(fid11,'\n');
        xn=xn+1;
    elseif (max(Tlocal0) >= Tf)
        fprintf(fid1,'%f\n',t);
        fprintf(fid2,'%f\t',F);
        fprintf(fid2,'\n');
        fprintf(fid3,'%f\t',ntotal);
        fprintf(fid3,'\n');
        fprintf(fid4,'%f\t',pH);
        fprintf(fid4,'\n');
        fprintf(fid5,'%f\t',pNa);
        fprintf(fid5,'\n');
        fprintf(fid6,'%f\t',pBa);
        fprintf(fid6,'\n');
        fprintf(fid7,'%f\t',Temp);
        fprintf(fid7,'\n');
        fprintf(fid9,'%f\t',abs(JH));
        fprintf(fid9,'\n');
        fprintf(fid10,'%f\t',abs(JNa));
        fprintf(fid10,'\n');
        fprintf(fid11,'%f\t',abs(JBa));
        fprintf(fid11,'\n');
        xn=xn+1;
    end
    if max(abs(F))>=Fmax
        Fbd=Vapp/d;            %set breakdown strength
        fprintf(fid8,'Electronic breakdown mechanism and Ebd is %f\n',Fbd);
        break
    elseif max(Temp)>=Tf
        Fbd=Vapp/d;            %set breakdown strength
        fprintf(fid8,'Thermal breakdown mechanism and Ebd is %f\n',Fbd);
        break
    end
end
fclose('all');

fid1=fopen('t_Na_H_Ba_100Vs_298K_50um_af45_nb.txt');
fid2=fopen('Efield_Na_H_Ba_100Vs_298K_50um_af45_nb.txt');
fid3=fopen('ntotal_Na_H_Ba_100Vs_298K_50um_af45_nb.txt');
fid4=fopen('pH_Na_H_Ba_100Vs_298K_50um_af45_nb.txt');
fid5=fopen('pNa_Na_H_Ba_100Vs_298K_50um_af45_nb.txt');
fid6=fopen('pBa_Na_H_Ba_100Vs_298K_50um_af45_nb.txt');
fid7=fopen('Tlocal_Na_H_Ba_100Vs_298K_50um_af45_nb.txt');
fid9=fopen('JH_Na_H_Ba_100Vs_298K_50um_af45_nb.txt');
fid10=fopen('JNa_Na_H_Ba_100Vs_298K_50um_af45_nb.txt');
fid11=fopen('JBa_Na_H_Ba_100Vs_298K_50um_af45_nb.txt');

tplot=fscanf(fid1,'%f');            % time variable for plot
Efield=fscanf(fid2,'%f',[m+1 xn]);
ntotal=fscanf(fid3,'%f',[m xn]);
pH=fscanf(fid4,'%f',[m xn]);
pNa=fscanf(fid5,'%f',[m xn]);
pBa=fscanf(fid6,'%f',[m xn]);
Temp=fscanf(fid7,'%f',[m+2 xn]);
```

```
AJH=fscanf(fid9,'%f',[m+1 xn]);
AJNa=fscanf(fid10,'%f',[m+1 xn]);
AJBa=fscanf(fid11,'%f',[m+1 xn]);

fclose('all');

h1=figure('Visible','off');
%hold on;
axbkgd=axes('Position',[0 0 1 1],'Visible', 'off');
axis([0 1 0 1]);
%formatting figure
set(gcf, 'renderer', 'painters');
set(gcf, 'color', 'white'); % sets the color to white

set(gcf, 'PaperUnits', 'inches');
xSize = 17;         %xSize = 8.5; %inches wide for total page
ySize = 22;         %ySize = 11; %inches high for total page
axisLeft = .1;
axisRight = .58;
axisTop = .73;
axisMiddle = 0.41;
axisBottom = .09;
axisXSize = .35;
axisYSize = .25;
axisInsetSize = .1;
InsetLeft = .30;
InsetBottom = .12;
set(gcf, 'PaperPositionMode', 'manual');
set(gcf, 'PaperSize', [xSize ySize]);
set(gcf, 'PaperPosition', [0 0 xSize ySize]);
Lfntsize=32;
Afntsize=24;

ColorSet=[0 0 0; 0 0 1; 1 0 1; 1 0 0];
LSorder={'-','--',':','-.'};

%titv=fix(xn/10);

%%%%FIGURE UPPER LEFT
ax1=axes('position',[axisLeft,axisTop,axisXSize,axisYSize]);
set(ax1,'FontSize',Afntsize,'XGrid','on');
grid(gca,'minor');
hold on
for kul=1:4

plot(x1',Efield(:,fix(xn*kul/4))./1e6,'Color',ColorSet(kul,:),'LineStyle',LSord
er{kul},'LineWidth',3);
end
xlabel('Position (\mum)','fontsize',Lfntsize,'fontweight','b');
ylabel('E field (MV/m)','fontsize',Lfntsize,'fontweight','b')
xlim([0 d*1e6]);
ylim([-1200 0]);
%text(10,0, '(a)','FontSize',Lfntsize, 'FontWeight','bold');
box off
hold off

%%%%FIGURE UPPER RIGHT
ax2=axes('position',[axisRight,axisTop,axisXSize,axisYSize]);
set(ax2,'FontSize',Afntsize,'XGrid','on');
grid(gca,'minor');
hold on
```

```
for kur=1:4

plot(x2',ntotal(:,fix(xn*kur/4)),'Color',ColorSet(kur,:),'LineStyle',LSorder{ku
r},'LineWidth',3);
end
xlabel('Position (\mum)','fontsize',Lfntsize,'fontweight','b');
ylabel('Net charge density (C/m^{3})','fontsize',Lfntsize,'fontweight','b')
xlim([0 d*1e6]);
ylim auto;  %ylim([-800 800]);
%text(10,800, '(b)','FontSize',Lfntsize, 'FontWeight','bold');
box off
hold off

%%%%FIGURE MIDDLE LEFT
ax3=axes('position',[axisLeft,axisMiddle,axisXSize,axisYSize]);
set(ax3,'FontSize',Afntsize,'XGrid','on');
grid(gca,'minor');
hold on
for kml=1:4

plot(x2',pH(:,fix(xn*kml/4)),'Color',ColorSet(kml,:),'LineStyle',LSorder{kml},'
LineWidth',3);
end
xlabel('Position (\mum)','fontsize',Lfntsize,'fontweight','b');
ylabel('Mobile H^{+} concentration
(#/m^{3})','fontsize',Lfntsize,'fontweight','b')
xlim([0 d*1e6]);
ylim auto;  %ylim([-10 800]);
%text(10,800, '(c)','FontSize',Lfntsize, 'FontWeight','bold');
box off
hold off

%%%%FIGURE MIDDLE RIGHT
ax4=axes('position',[axisRight,axisMiddle,axisXSize,axisYSize]);
set(ax4,'FontSize',Afntsize,'XGrid','on');
grid(gca,'minor');
hold on
for kmr=1:4

plot(x2',pNa(:,fix(xn*kmr/4)),'Color',ColorSet(kmr,:),'LineStyle',LSorder{kmr},
'LineWidth',3);

end
xlabel('Position (\mum)','fontsize',Lfntsize,'fontweight','b');
ylabel('Mobile Na^{+} concentration
(#/m^{3})','fontsize',Lfntsize,'fontweight','b')
xlim([0 d*1e6]);
ylim auto;  %ylim([-0.5 40]);
% ind=[1 2 3 4];          %select the plots to include in the legend
% l1=legend(hmr(ind),smr{ind},'Location','SouthWest');      %Creat legend for
the selected plots
%text(10,40, '(d)','FontSize',Lfntsize, 'FontWeight','bold');
box off
hold off

%%%%FIGURE LOWER LEFT
ax5=axes('position',[axisLeft,axisBottom,axisXSize,axisYSize]);
set(ax5,'FontSize',Afntsize,'XGrid','on');
grid(gca,'minor');
hold on
for kll=1:4
```

```
hmr(kll)=plot(x2',pBa(:,fix(xn*kll/4)),'Color',ColorSet(kll,:),'LineStyle',LSor
der{kll},'LineWidth',3);
    smr{kll}=sprintf('%4.2f s',tplot(fix(xn*kll/4)));
end
xlabel('Position (\mum)','fontsize',Lfntsize,'fontweight','b');
ylabel('Mobile Ba^{2+} concentration
(#/m^{3})','fontsize',Lfntsize,'fontweight','b')
xlim([0 d*1e6]);
ylim auto;  %ylim([-10 800]);
ind=[1 2 3 4];          %select the plots to include in the legend
l1=legend(hmr(ind),smr{ind},'Location','SouthWest');      %Creat legend for the
selected plots
%text(10,800, '(e)','FontSize',Lfntsize, 'FontWeight','bold');
box off
hold off

print(h1,'-dtiff','2Dplot_Na_H_Ba_100Vs_298K_50um_af45_nb.tif');

toc;
```

VITA

Doo Hyun Choi

Doo Hyun Choi was born in Boryung, Korea on December 29, 1977. He graduated from Seoul National University, Seoul, Korea with his B.S. degree in Materials Science and Engineering in 2000. He continued his graduate study at the same university and got his M.S. degree in Materials Science and Engineering in 2002. He then worked at Agency for Defense Development in Korea for about 7 years as a senior researcher. During the period he studied dielectric phenomena in microwave frequency for silica based materials and earned Bronze technology award and Recognition of outstanding contribution to the development in defense technology in 2008. In 2009 he decided to pursue Ph.D. degree in the Department of Materials Science and Engineering at the Pennsylvania State University. He received the George W. Brindley/Jyung-oock Choe Graduate Fellowship from the Department of Materials Science and Engineering at the Pennsylvania State University in 2010 and 2011.